Demonstration of near Diffraction-Limited Imaging using a THz CMOS-Integrated Camera

Robbin van Dijk

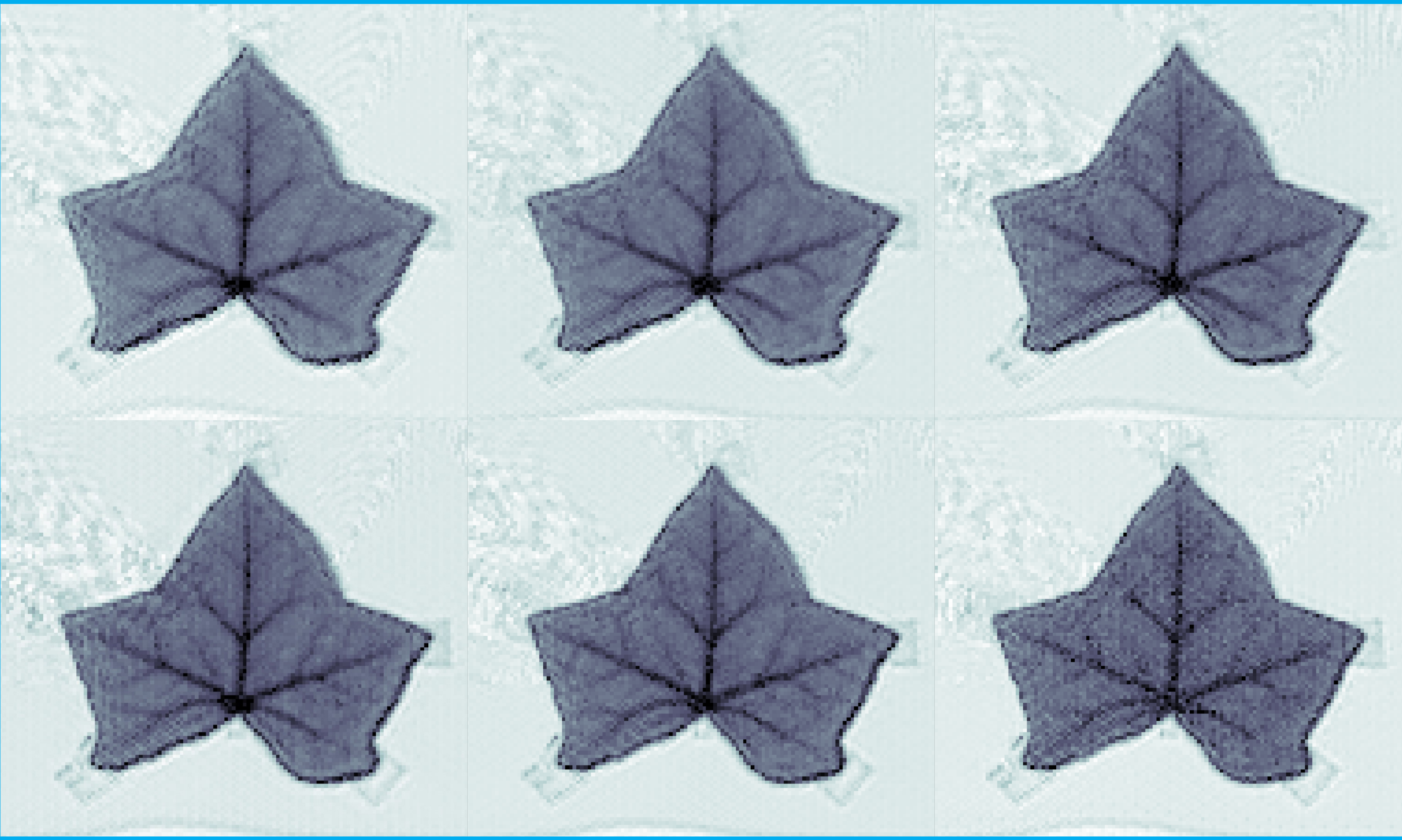

Demonstration of near Diffraction-Limited Imaging using a THz CMOS-Integrated Camera

MSc. Thesis

by

Robbin van Dijk

To obtain the degree of Master of Science,
at Delft University of Technology,
to be defended publicly on the 17th of November, 2023.

Project duration: October 2022 – November 2023
Thesis Committee: N. Llombart, M. Alonso-delPino, M. Spirito

Abstract

This work aims to make a (near) diffraction-limited image at sub-millimeter wavelengths using a previously developed terahertz camera in CMOS techonlogy at 200 GHz - 600 GHz with a high angular resolution, thanks to the high pixel density in its focal plane array (FPA). To this end, a quasi-optical (QO) imaging setup with active illumination is designed and optimized such that it provides uniform illumination of the imaging plane. The major design challenge is to design a QO setup that does not degrade the scanning capabilities of the FPA and simultaneously maximizes uniform coupling between the THz source and each of the detectors of the FPA. The implementation of the QO imaging system is described in detail, including the read-out electronics and alignment of the various focusing elements. The alignment steps of the QO setup are described with an overall accuracy of 0.7 mm. To validate the QO imaging system, the designed radiation patterns in the imaging plane and coupling are extracted from the measured voltage response of the detector. To quantify the similarity between the measured patterns and simulated patterns, the near fields directivities are calculated, which show a maximum deviation of 0.45dB within the characterized band compared to simulations. The characterized coupling of the camera to the source showed a 0.7 dB agreement with simulations over the considered band. Finally, a slotted metal plate and a leaf were imaged using the THz camera. The resulting images have excellent quality in terms of resolution and demonstrate the (near) diffraction-limited resolution of the THz camera.

Acknowledgements

While this year presented numerous challenges, I managed to overcome them with the support of various individuals. Consequently, this section is dedicated to expressing my gratitude to those who have helped me navigate these difficulties.

First of all, I would like to express my sincere appreciation to dr. M. Alonso-delPino and M. Hoogelander for being my daily supervisors. Their knowledge, guidance and support allowed me to learn a lot this year and enabled me to take the thesis to a higher level.

Furthermore, I would like to thank everyone in the THz Sensing group for always being open to discussion and trying to help each other out, even if someone has nothing to do with the project. The number of times I was able to get new insights in the theory in this manner is impressive and makes the environment so valuable. A special thanks to the office mates for all the good times.

Finally, I would like to thank my parents for their encouragement when I needed it during my thesis, and my brother for being the kind, supportive person he is.

Contents

Appendices

Chapter 1

Introduction

1.1 Background and project context

Over the past decades, technology in the largest portion of the electromagnetic spectrum has matured, with applications spanning from healthcare to the defence industry. In the THz band, from 0.3 THz to 3 THz, commercial applications remain limited due to the technology gap: the design of compact and power-efficient sources and detectors in this band remains challenging. The lack of equipment is not due to a limited amount of user cases. The THz band has great potential in fields like astronomy, as this band contains many molecular absorption lines [1]. Another user case is in the automotive industry due to its high resolution w.r.t. radio waves and the ability to propagate through adverse environment like fog [2]. The THz band also has potential for next generation telecommunication due the large available bandwidth [3]. Finally, the THz band could be useful in security screening thanks to the high resolution, non-ionizing characteristics and ability to penetrate clothing and packaging materials with little attenuation [4]. This work is focused around the imaging applications in the THz band.

Heterodyne detection versus direct detection

When an image is captured, the radiation can in general be detected using either heterodyne detection or direct detection. Heterodyne detection has several advantages, like a higher SNR and retention of phase, which can be used to extract more information from the received signal. However, the mixers and amplifiers needed for heterodyne detection make compact integration difficult and increase the power consumption [5]. In direct detection, only the amplitude of the signal is detected. This results in simple detection schemes and low power consumption, as no local oscillator or mixers are needed for amplitude measurements. This simple detection scheme makes direct detectors an excellent candidate for large-integrated FPA cameras. An important performance metric of a detector is the noise-equivalent-power (NEP), which is defined as the signal power that gives a signal-to-noise ratio of one in a one Hz output bandwidth [6]. In the past, integrated THz detectors had an NEP that was too high for imaging purposes. However, thanks to the advancements in f_T/f_{max} of silicon-based technology like CMOS and BiCMOS [5], THz direct detectors with an appealing noise equivalent power (NEP) can now be designed for imaging applications. As a result, it becomes viable to work towards a fully integrated passive imaging system in silicon-based technology that is low-cost, low-power and can be mass produced.

Challenges in passive THz imaging using direct detection

Two challenges remain to be solved before such a passive imaging system can be achieved. First, a detector with low NEP and large bandwidth is needed. For real-time imaging, a detector with NEP in the order of a few $pW/\sqrt{Hz}$ and several hundred GHz bandwidth is required [7]. Second, a tight sampling of the focal plane is required for a high resolution. Any imaging system has an upper limit to the resolution that can be achieved caused by the dimensions of the optics that are used. This upper limit to the resolution is called the diffraction limit, and it is obtained when the focal plane is sampled with an inter-element distance of $d_f = \lambda_d F/(2D)$ [8], where λ_d is the wavelength in the medium in which the focal plane is located, F is the focal length and D is the diameter of the used optics.

State-of-the-art THz imager resolution

Imaging setups with (near) diffraction-limited resolution have been demonstrated at THz frequencies using one of two methods. The first method involves cryogenically cooling the detectors to decrease the NEP [9], the complexity/cost of which makes the system unsuitable for commercial applications. The second method involves using a sparsely sampled array and mechanically scanning the field of view [10], which results in a refresh rate penalty. This work focuses on room-temperature direct detection cameras using silicon technologies. The use of silicon technologies allows to achieve a mass-producible, low-cost, low-power camera. Table 1.1 [11] shows an overview of state-of-the-art room-temperature silicon-based cameras.

Table 1.1: Comparison of state-of-the-art silicon THz imagers.

Reference	Technology	Array grid	Antenna	Size	BW (Abs.)	Periodicity d_f	η_{ap}
This work	22 nm SOI CMOS	Chessboard	Dipole	2 × 2 × 3	200 - 600 GHz	$0.7F_{\#}\lambda_d$	-4.1 dB
[12]	22 nm SOI CMOS	-	Double slot	1 × 1	200 - 600 GHz	$2.5F_{\#}\lambda_d^{(a)}$	-3.0 dB
[13], [14]	130 μm SiGe	-	Wire ring	1 × 1	350 - 1000 GHz$^{(b)}$	$1.2F_{\#}\lambda_d^{(a)}$	-4.0 dB
[15]	65nm SOI CMOS	Rectangular	Wire ring	32 × 32	750 - 1000 GHz	$1.4F_{\#}\lambda_d$	-3.2 dB
[16]	65nm SOI CMOS	Rectangular	Patch	4 × 4	270 - 290 GHz	$0.5\ \lambda_0\ ^{(c)}$	-5.5 dB
[17]	130 μm SiGe	Rectangular	Wire ring	4 × 4	230 - 290 GHz	$0.5\ \lambda_0\ ^{(c)}$	-3.4 dB$^{(d)}$

(a) single detector elements are presented which are not integrated in an FPA, thus a comparison is made with an FPA composed of these single elements. (b) 450 GHz is taken as a reference frequency, since this is where the imager reaches peak sensitivity. (c) These works do not include a focusing element in the imaging system. (d) Estimated from the difference between the reported detector and system NEP using [15], the authors mention a near conjugate impedance matching.

In [12], a wideband single pixel detector is presented with excellent aperture efficiency. The detector meets the requirement of several hundred GHz bandwidth for passive imaging, but achieves a large periodicity of $2.5F_{\#}\lambda_d$. In [13] and [14] a wideband wire ring is presented with high radiation efficiency and relatively small dimensions, which means that it can reach a periodicity of $1.2F_{\#}\lambda_d$ when used in an array. In [15] a 1k-pixel THz array is demonstrated. This array has excellent aperture efficiency, a relatively large bandwidth and a large number of detectors, verifying the scalability of the design and reaches a periodicity of $1.4F_{\#}\lambda_d$. [16] and [17] present imager arrays with a more narrow bandwidth. The arrays are difficult to compare in terms of resolution as they do not include a focusing element.

At the THz Sensing Group in TU Delft a 12 pixel CMOS camera was recently developed [11]. This THz camera contains an FPA with integrated, antenna-coupled direct detectors in 22 nm CMOS technology and operates between 200 GHz to 600 GHz. By applying polarization re-usage, the FPA achieves a diagonal element separation of $d_f = \lambda F/(\sqrt{2}D)$, λ_d being the wavelength in silicon at 387 GHz. This element separation is close to the diffraction-limited sampling of $d_f = 0.5\lambda F/D$, as will be shown in Chapter 2.

When comparing the state-of-the-art THz imagers in Table 1.1, it becomes clear that the FPA of this work achieves substantially better periodicity than any of the other THz imagers, in combination with a high aperture efficiency and broadband operation. Therefore, this work is dedicated to the demonstration of (near) diffraction-limited images using this previously designed silicon-integrated THz camera [11] that is suitable for passive imaging with future low NEP detectors.

State-of-the-art THz quasi-optical systems for THz imaging

Currently, all THz imagers in literature use illumination to overcome the poor NEP of the detectors. There have been multiple examples where images have been realized using active illumination. One such example is presented in [16], where the object is placed between the source and detector, but in this design no quasi-optical (QO) system is used and the distance between detector and source is just 20mm, putting constraints on user cases. Another common approach is to perform a raster scan with a QO setup where detector and source both focus in the imaging plane [17] [18], increasing resolution and coupling, but such an approach is only suitable for single-pixel imaging. In [17] the imaging plane is illuminated by a collimated beam to allows multiple detectors to couple to the THz source simultaneously, but no optimization is performed on the coupling and scanning capabilities of the setup. Thus far, to the best of the author's knowledge, no structured design strategy has been demonstrated to implement a multi-pixel imaging system does not degrade the scanning capabilities of the FPA and simultaneously maximizes uniform coupling between the THz source and each of the detectors of the FPA.

1.2 Thesis objectives

This work aims to realize (near) diffraction-limited images using the silicon-integrated THz camera developed in the THz Sensing Group [11]. Since the NEP of the CMOS direct detectors is too high at room temperatures to achieve passive performance, active illumination using a coherent THz source is required. In this contribution a QO setup has been developed that does not degrade the scanning capabilities of the FPA and simultaneously maximizes uniform coupling between the THz source and each of the detectors of the FPA. This objective has been divided in the following segments:

1. The analysis and optimization of the proposed QO imaging setup.
2. The practical implementation of the QO imaging system with the CMOS passive imager array.
3. Characterization of patterns and coupling of the implemented QO imaging setup.
4. The capturing of near diffraction-limited images in the THz regime.

1.3 Outline of the thesis

This work is divided into 4 central chapters. In Chapter 2, the design of a QO setup [19] to realize images with the CMOS FPA is presented the and the trade-offs of such a design are analysed. The radiation patterns of the detector are presented, and the radiation patterns of the detector and source in the imaging plane are designed to provide uniform coupling among all detectors. The chapter ends with an analysis of all losses in the QO setup. Chapter 3 describes the procedure to realize the QO imaging setup described in Chapter 2. Specifically, the chapter presents an overview of the of the overall implementation, the detector architecture, the readout, the implementation of the 12 pixel FPA and the alignment process of the QO setup. Chapter 4 validates the QO setup by measuring the radiation patterns in the imaging plane and the coupling of the overall setup. The measured coupling and radiation patterns are compared with their simulated values obtained in Chapter 2. In Chapter 5 the imaging method is described and the obtained images of two subjects are presented and analysed. Finally, Chapter 6 provides conclusion and discusses the future work.

Chapter 2

Design of Quasi-Optical setup

The design of a Quasi-Optical setup to realize images with the CMOS FPA, described in [19], is presented in this chapter. The CMOS FPA has been integrated in a hyperhemispherical lens to create a virtual FPA, which, in combination with a biconvex lens, focuses the radiation in the imaging plane with a resolution in the mm range and with very tight sampling. In this QO setup, the active illumination was used to overcome relatively high NEP of the FPA and increase the DR of the setup. The trade-off between coupling and the resolution of the system as well as the losses have been analyzed. The final design of the QO setup is presented.

2.1 Geometry

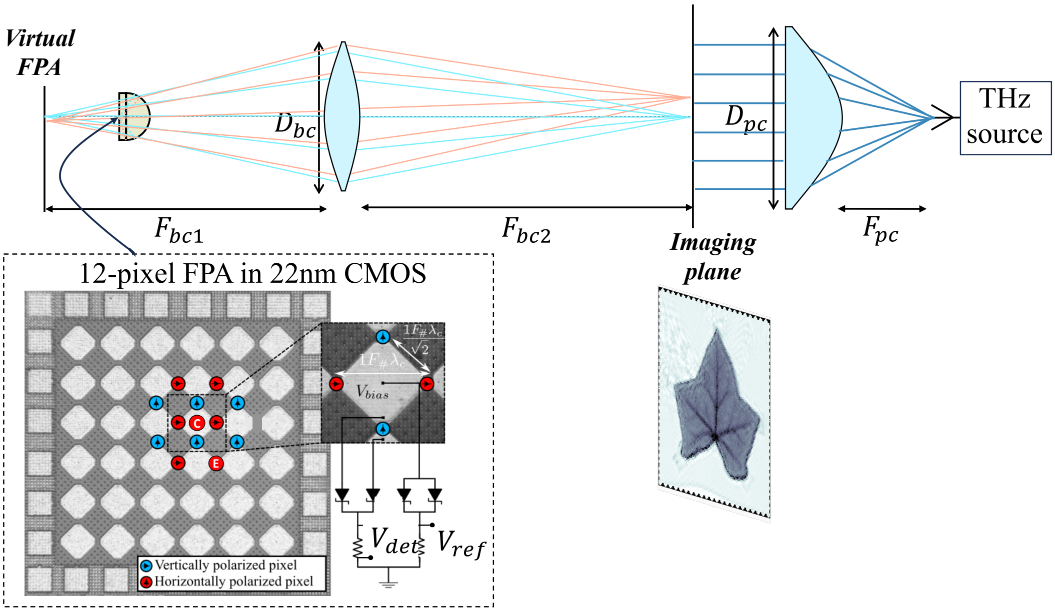

Figure 2.1: Schematic overview of the QO setup.

An overview of the complete QO system is shown in Figure 2.1. On one side, the focal plane array (FPA) is integrated with a hyperhemispherical lens that creates a virtual focal plane array (VFPA) behind the array. The FPA shows a virtual center and edge pixel, which will be used to determine the best and worst case performance of the QO setup. The array will be tilted 45 degree w.r.t. the THz source, so that both polarization can be illuminated simultaneously. The hyperhemispherical lens is designed to couple to a hyperbolic biconvex lens with an f-number $f_{bc1} = F_{bc1}/D_{bc}$, where D_{bc} is the diameter of the biconvex lens and F_{bc1} the focal length on the receiver side. The design of the virtual focal plane array is explained in Section 2.1.1.

The second side of the biconvex lens focuses the radiation of each pixel on the imaging plane with an f-number $f_{bc2} = F_{bc2}/D_{bc}$. Section 2.1.2 elaborates on the design of this source side of the biconvex lens.

The imaging plane is illuminated by a coherent source with a 20dB standard gain horn through a planoconvex hyperbolic lens. The trade-offs that are involved in the design of this hyperbolic lens are discussed in Section 2.1.3.
The overall performance of the QO setup, including the FPA and antenna losses, will be presented in Section 2.2.

2.1.1 Virtual Focal Plane Array

Substrate lenses are the preferred solution for integration with silicon chips since lens and chip's substrate are of the same dielectric constant and thus broadband operation can be realized. An elliptical lens is commonly used for maximum directivity. However, in an elliptical lens a displacement in the FPA translates to a scanning angle with all scanning angles having the phase center at the tip of the lens. The QO setup used in this work uses a refocusing element, which means that identical phase centers get refocused to the same location. This means that with an elliptical lens, no scanning can be performed in this QO setup, as is illustrated in Figure 2.2.

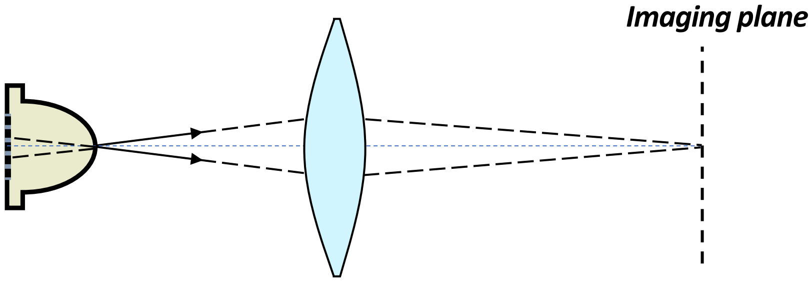

Figure 2.2: Elliptical lens in the focus of a biconvex, hyperbolic lens. This configuration cannot perform scanning in the imaging plane.

The hyperhemispherical substrate lens used in [20],[21] is and excellent solution to increase scanning capabilities while keeping the system compact. It is a broadband solution since it is an aplanatic design, i.e. the rays are still focused on a spot.

Figure 2.3 shows a schematic overview of the architecture. The hyperhemispherical lens is a particular case of extended hyperhemispherical lens, with the hemisphere radius R_l and extension length $L_l = R_l/\sqrt{\epsilon_r}$, ϵ_r being the relative permittivity of the lens. When this lens is excited by a feed in the center of its base, the field radiated by the lens appears as if generated by a virtual source placed in a point below the lens. This virtual focus point is located at a distance $F_v = R_l(\sqrt{\epsilon_r}+1)$ from the tip of the lens. The virtual focus should be aligned with the focus of the biconvex lens on the receiver side.
When a feed element of the FPA is displaced by a distance d_f from the on-axis position, the corresponding virtual feed also displaces from the virtual focus point by a distance d_v, as shown in Figure 2.3. For small displacements, the scanning angle of the displaced feed, θ_{out}, can be approximated using Snell's law as in

$$\theta_{out} \approx \epsilon_r \frac{d_f}{R_l(1+\sqrt{\epsilon_r})} \tag{2.1}$$

The angle θ_{in} (see Figure 2.3) is identical to θ_{out} and can be calculated through geometrical considerations by assuming a small displacement as in Equation 2.2.

$$\theta_{in} \approx \frac{d_v}{R_l(1+\sqrt{\epsilon_r})} \tag{2.2}$$

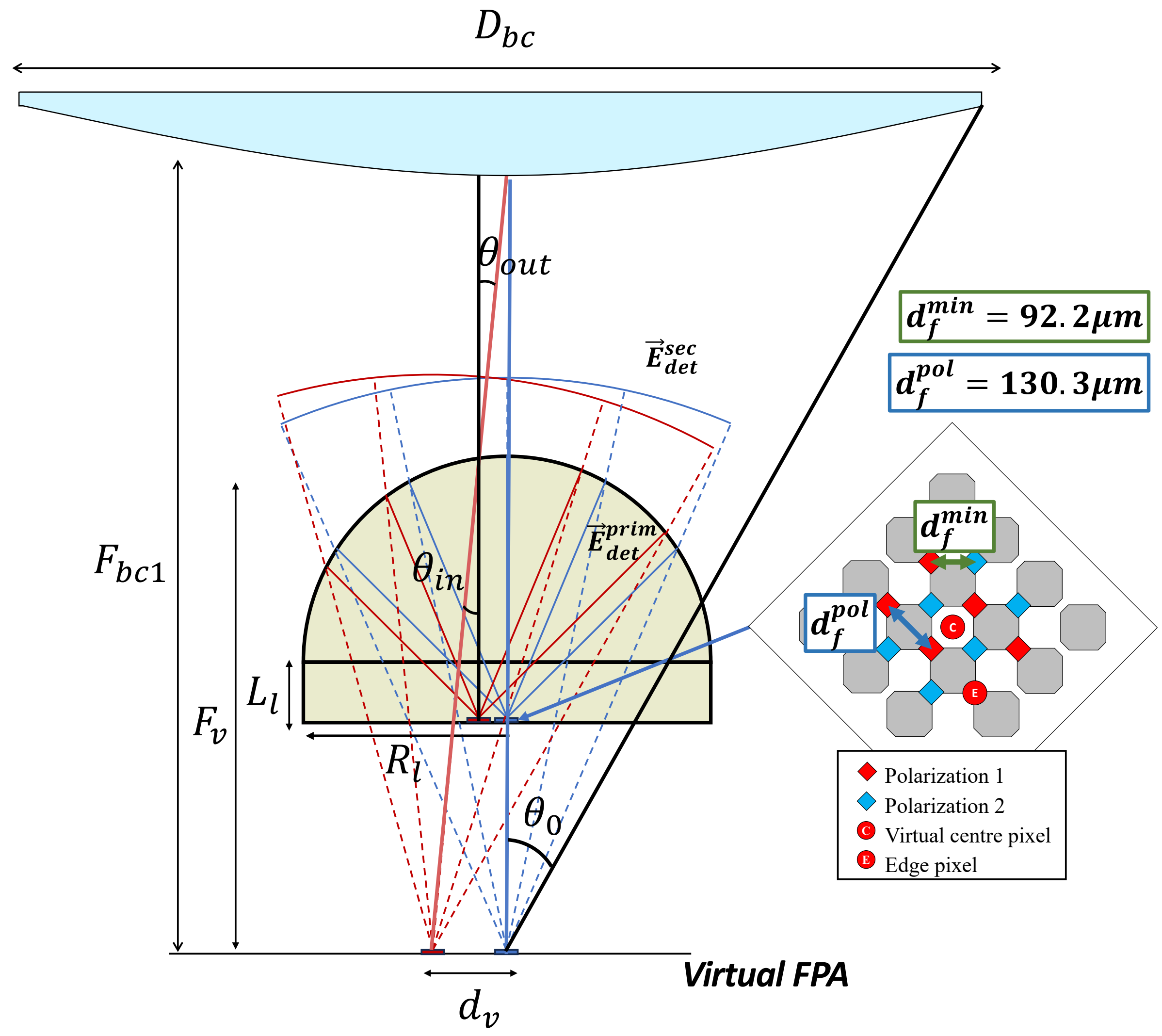

Figure 2.3: A schematic representation of the FPA in the hyperhemispherical lens and illustration of the virtual FPA created by such a hyperhemispherical lens. The minimum.

Therefore, the resulting displacement in the VFPA can be obtained by equating 2.2 and 2.1, yielding Equation 2.3.

$$d_v \approx d_f \epsilon_r \tag{2.3}$$

The overall performance of the system (i.e. scan loss) depends on the geometrical parameters of the hyperhemispherical and hyperbolic lens. For large values of R_l, the patterns become more symmetric as the scanning angle decreases, resulting in smaller scan loss[21]. However, larger lens radii makes the integration with the detector more challenging. As a compromise, a diameter of $20\lambda_0$ at 400 GHz was chosen, which corresponds to 15 mm.

The radiation patterns of the hyper-hemispherical lens with the FPA have been simulated using a combination of full-wave simulation and PO techniques. The embedded radiation patterns inside the silicon medium were obtained through a full-wave simulation, and then propagated to the outside of the lens using an in-house Physical Optics (PO) tool [22]. Figure 2.4 shows the magnitude and phase of these secondary patterns. As can be seen, a relatively symmetric pattern is obtained.

In previous works, the hyperhemispherical lens was designed for an f-number corresponding to

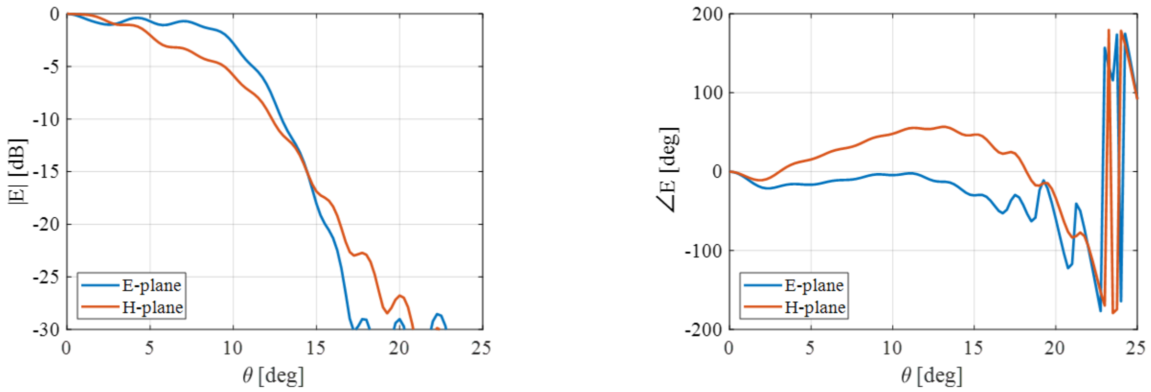

(a) Amplitude.

(b) Phase.

Figure 2.4: Simulated secondary patterns of virtual center pixel C (see Figure 2.3) phase and amplitude at 400 GHz.

the -15 dB field tapering of the primary patterns inside the silicon, e.g., at an angle of 60° [23]. This corresponds to an f-number of the feed $f_f = \frac{1}{2sin^{-1}(60)} = 0.58$. In order for the biconvex lens to be illuminated by the hyperhemispherical lens by the same taper angle, the f-number of the biconvex lens should be approximately $f_{bc1} = f_f\sqrt{\epsilon_r} = 2.0$ [21]. To optimize this f-number, the aperture efficiency $\eta_{ap,BC}$ of the biconvex lens was calculated for both the center and edge pixel using the radiation patterns of the hyperhemispherical lens, for different values of f_{bc1}. The aperture efficiency of the biconvex lens is defined as:

$$\eta_{ap,BC} = \eta_{tap,BC}\eta_{SO,BC} \tag{2.4}$$

Here, $\eta_{SO,BC}$ is the spillover efficiency of the biconvex lens. The spillover efficiency is defined as follows:

$$\eta_{SO,BC} = \frac{\int_0^{2\pi}\int_0^{\theta_0}|\vec{E}^{sec}_{det}|^2 sin\theta d\theta d\phi}{\int_0^{2\pi}\int_0^{\pi/2}|\vec{E}^{sec}_{det}|^2 sin\theta d\theta d\phi} \tag{2.5}$$

In this equation, $\vec{E}^{sec}_{det}$ is the electric field of the hyperhemispherical lens evaluated on a sphere of radius F_{bc1} centered at the the virtual focus of the hyperhemispherical lens. θ_0 is the subtended half-angle (see Figure 2.3).
$\eta_{tap,BC}$ is the taper efficiency of the biconvex lens and is defined as in Equation 2.6.

$$\eta_{tap} = \frac{Dir\lambda_0^2}{4\pi A_{phys}} \tag{2.6}$$

Where Dir is the directivity of the equivalent aperture of the biconvex lens, λ_0 is the wavelength in free space, for which the center frequency of 400GHz has been used for this analysis. A_{phys} is the physical area of the equivalent aperture, which is $\pi(D_{bc}/2)^2$.

Figure 2.5 shows the resulting aperture efficiency of the biconvex lens for the center and edge pixel, and shows that the optimum occurs at $f_{bc1} = 2.12$ for both pixels, corresponding to a taper angle of $\theta_0 = tan^{-1}(\frac{1}{2F_\#}) = 13.3°$, which is slightly higher than the $f_{bc1} = 2.0$ that is prescribed by [21]. Figure 2.4a shows that this angle is only slightly smaller than the -15 dB taper angle, which occurs around 14°. The optimum η_{ap} is obtained for a higher f-number most likely due to the non-uniform phase (see Figure 2.4b), which deviates more for larger angles. A design was chosen where the f-number resulted in the highest η_{ap}, which is $f_{bc1} = 2.12$.

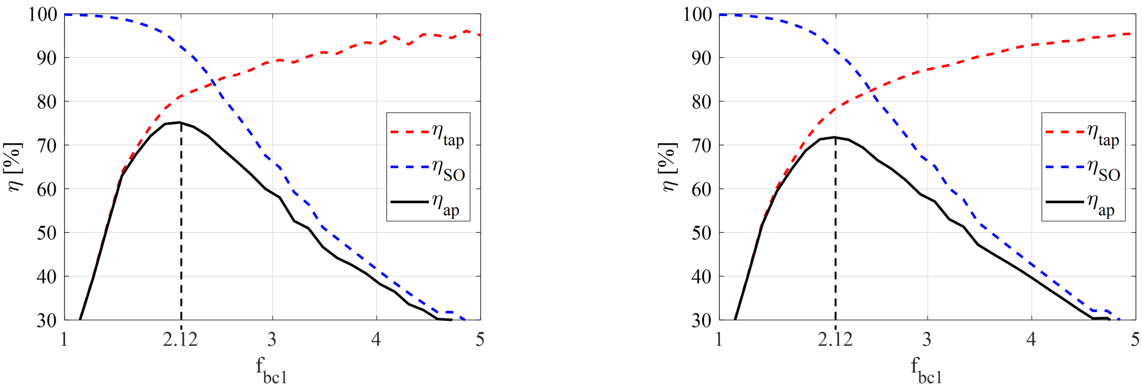

(a) Virtual center pixel. **(b)** Edge pixel.

Figure 2.5: aperture efficiency of the biconvex lens at 400 GHz.

2.1.2 Detector Illumination on the imaging plane

Figure 2.7 shows a schematic overview of the imaging plane illuminated by the imaging side of the biconvex lens. For this setup, it is desired to know the relation between the HPBW, $\Delta\rho^{det}_{HPBW}$, and the geometry. Therefore, the electric field, $\vec{E}^{im}_{det}$, is computed by propagating radiation from the VFPA through the biconvex lens to the imaging plane, using a PO method in GRASP. From this field, $\Delta\rho^{det}_{HPBW}$ is calculated for different values of the second f-number of the biconvex lens f_{bc2} for both the center and edge pixel. The results are shown in Figure 2.6. It can be seen that pixel E has a larger $\Delta\rho^{det}_{HPBW}$, which is due to the lower taper efficiency as shown in Figure 2.5b.

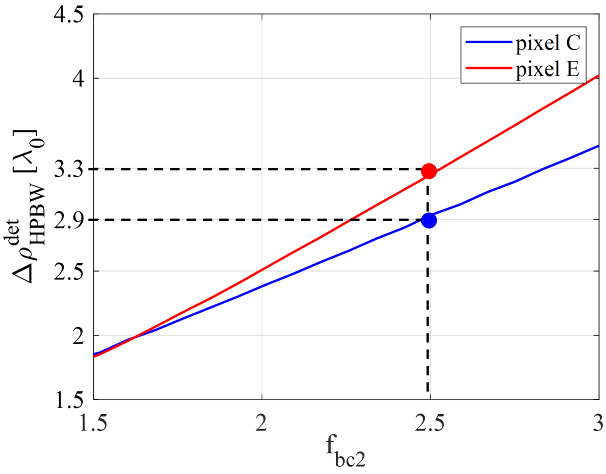

Figure 2.6: HPBW versus f_{bc2}.

For a given f_{bc2}, the inter-element distance of the FPA in the imaging plane d_v is given by Equation 2.7.

$$d_i = \frac{F_{bc2}}{F_{bc1}} d_v \tag{2.7}$$

Where d_i and d_v are the displacements from the on-axis location in the imaging plane and VFPA, respectively. Thus, a small f-number results in a high resolution. While a small f-number results in a high resolution, it also results in a lower depth-of-field. This in turn makes alignment of the

QO setup more difficult. A smaller HPBW also means diffraction effects will become more pronounced. To keep a good resolution, but also keep diffraction effects limited, $\Delta\rho_{HPBW}^{det} \approx 3\lambda_0$ was chosen which corresponds to $f_{bc2} = 2.5$ (see Figure 2.6). This results in a deviation in $\Delta\rho_{HPBW}^{det}$ of 14% for pixel E w.r.t. pixel C, which is acceptable considering it also results in a larger depth-of-field. The final dimensions of this QO setup are shown in table 2.1. The realized half-power beamwidth (HPBW) of the camera is $\Delta\rho_{HPBW}^{det} = 2.1mm$ and $\Delta\rho_{HPBW}^{det} = 2.48mm$ for a pixel located in the FPA center and at the edge, respectively, at 400 GHz. The detector (and source) radiation patterns in the imaging plane are shown in Figure 2.8.

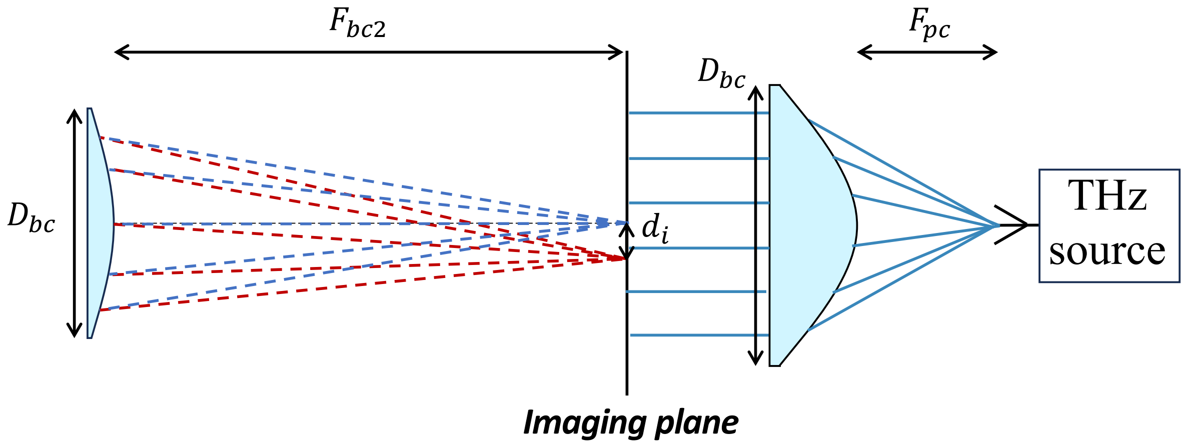

Figure 2.7: HPBW versus f_{bc2}.

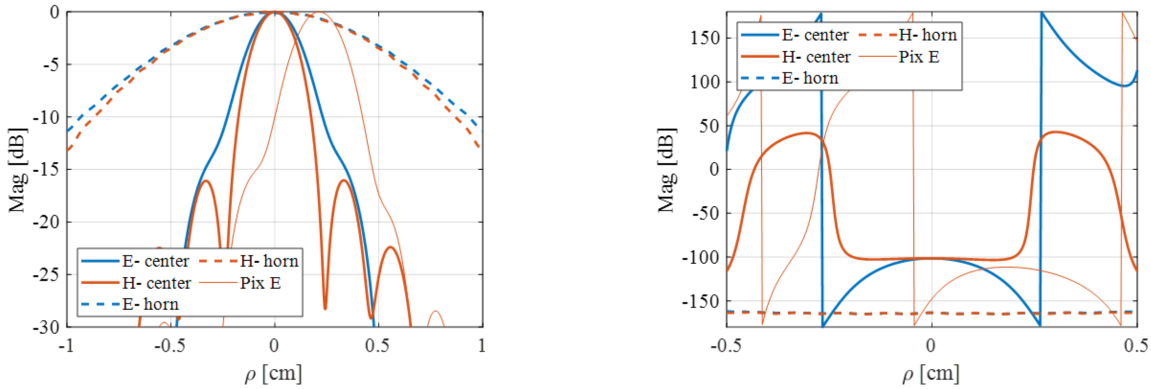

(a) Amplitude. **(b)** Phase.

Figure 2.8: Simulated patterns of pixels C (see Figure 2.3) and E, phase and amplitude in imaging plane.

From Equation 2.3 and 2.7, the relation between the inter-element distance in the FPA and inter-element distance in the imaging plane can be calculated geometrically as:

$$d_i = \frac{F_{bc2}}{F_{bc1}} \epsilon_r d_f \tag{2.8}$$

This way, the minimum separation in the imaging plane between two elements of the FPA can be calculated as $d_i^{min} = 1.27mm$. In [11] when an elliptical lens is used, a sampling is achieved of $d = \frac{F_{\#}\lambda}{\sqrt{2}}$, at 363 GHz, where $F_{\#}$ is the f-number of the elliptical lens. In this setup, an equivalent sampling in the imaging plane is achieved $d_i^{min} = \frac{f_{bc2}\lambda_0}{\sqrt{2}}$ at 417 GHz. The difference can be ascribed

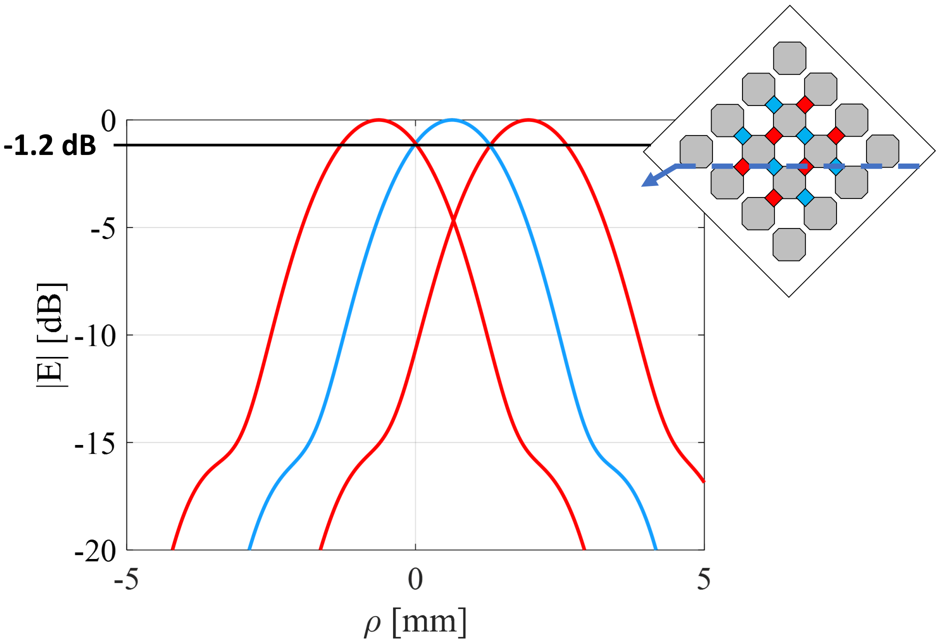

Figure 2.9: Beam overlap for 3 adjacent oppositely polarized pixels in the imaging plane at 400 GHz

to the use of a different QO setup. Figure 2.9 shows the simulated $\vec{E}_{det}^{im}$ patterns for 3 oppositely polarized adjacent (i.e. minimum separation) pixels in the imaging plane at 400 GHz. It can be seen that the beam-overlap is approximately -1.2 dB, which is slightly higher than in [11], where the simulated beam overlap at 400 GHz is -1.3 dB. The difference can be ascribed to a lower directivity of the hyperhemispherical lens.

2.1.3 Coherent Source Illumination

Current state-of-the-art antenna coupled direct detectors in silicon technology are not yet capable of achieving passive imaging for room temperature scenarios. The imagers rely on illumination from an active THz source to increase the dynamic range [15] [16]. This can be problematic when having a FPA since one requires all the pixels illuminated equally to ensure that their imaging performance is uniform. To generalise the analysis, the HPBW ratio is introduced, which is defined as how much wider the beam of the source is in the imaging plane w.r.t. the beam of the detector: $\Delta\rho_{HPBW}^{src}/\Delta\rho_{HPBW}^{det}$.
To arrive at the most compact setup that achieves uniform illumination, multiple topologies were analyzed in which the imaging plane is illuminated in different manners [19], as shown in Figure 2.10. The basic scheme is the FPA on one end, a THz source placed on the other end, and the imaging plane in-between. To simplify the analysis, the beams from the horn and FPA are approximated by Gaussian beams. To model a beam corresponding to an off-axis FPA element, a linear phase shift was included. To investigate how to achieve uniform coupling of the source to the two beams, we define the coupling efficiency. It is given by:

$$\eta_c = \frac{|\int\int_{S_{im}} \vec{E}_{det}^{im} \cdot \vec{E}_{src}^{im} dS|^2}{\int\int_{S_{im}} |\vec{E}_{det}^{im}|^2 dS \int\int_{S_{im}} |\vec{E}_{src}^{im}|^2 dS} \tag{2.9}$$

Where $\vec{E}_{det}^{im}$ and $\vec{E}_{src}^{im}$ represent the electric fields of the camera and the horn antennas in the imaging plane S_{im}, respectively. $\vec{E}_{src}^{im}$ is computed from the propagation of the primary fields of the horn through the planoconvex lens to the imaging plane, through a PO method in GRASP, trough the

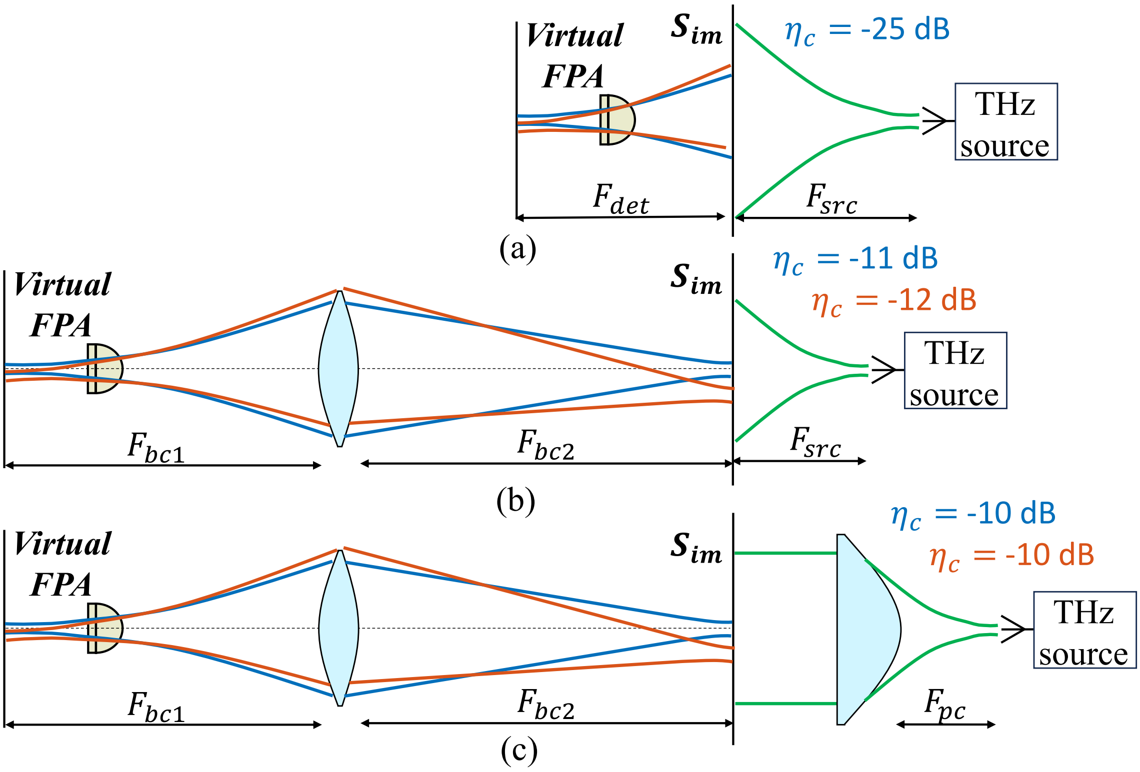

Figure 2.10: Different topologies for illuminating the imaging plane and the coupling efficiency between the source and beams.

same method as was used for the detector side. The coupling efficiency is shown for the three variations for a pixel in the FPA center and edge pixel in the FPA, when assuming a HPBW ratio of six in the imaging plane, between the detector and source fields. As shown in Figure 2.10, focused illumination on the camera side provides the best coupling efficiency. On the illumination side, a source radiating a collimated beam will not only couple well to the virtual center pixel but also improves the coupling to the edge pixel. Thus, in order to both maximize the coupling and have uniform coupling to all FPA pixels, the choice was made to have a collimating lens at the horn side of the setup, and a focusing lens at the detector side. This collimated beam has been implemented in the setup by the use of a planoconvex hyperbolic lens.

An analysis of the aperture efficiency of the planoconvex lens with the horn was performed as a function of f_{PC}, following the same procedure as in Section 2.1.1. The result is shown in Figure 2.11. The figure shows maximum aperture efficiency for $f_{pc} = 1.48$, which will be the used f-number.

With f_{pc} selected, the diameter of the planoconvex lens, D_{pc}, is left to optimize, which is an important design choice as it determines the HPBW of the source in the imaging plane $\Delta\rho^{src}_{HPBW}$. Intuitively, one would want to maximize the coupling between the coherent source and the detector by (conjugately) matching their fields in the imaging plane, therefore also maximizing the DR. However, the resolution of the imaging setup will then be defined by the two-way pattern (TWBP) of the imaging system, including both the source and the detector patterns [24]. The resulting resolution then becomes $\Delta\rho^{QO}_{HPBW} = \Delta\rho^{det}_{HPBW}/\sqrt{2}$, with $\Delta\rho^{QO}_{HPBW}$ being the HPBW of the TWBP. This will be especially important when performing active imaging with the FPA, since it is not desired to have to align the antenna of the coherent source to the beams of every individual pixel within the FPA.

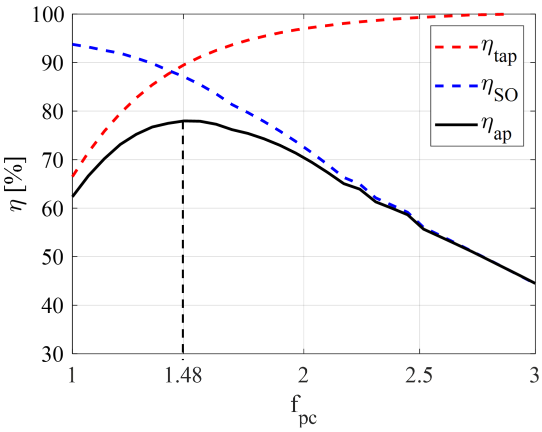

Figure 2.11: Aperture efficiency of the horn with planoconvex lens as a function of f_{pc}.

This effect is illustrated in Figure 2.12, where a scenario with a low HPBW ratio (Figure 2.12a) is compared with the scenario for high HPBW ratio (Figure 2.12b). The figure shows that for a low HPBW ratio, $\Delta\rho^{QO}_{HPBW}$ deviates significantly from $\Delta\rho^{det}_{HPBW}$, especially for the edge pixel. The peak location of the TWBP is also shifted more to the center. Moreover, the maximum amplitude of the TWBP is lower w.r.t. the TWBP of the virtual center pixel, causing a deviation in DR between center and edge pixel. In the high HPBW ratio scenario resolution of the overall camera is given by the detector and not influenced by the source, but more power is lost in due to a lower coupling.

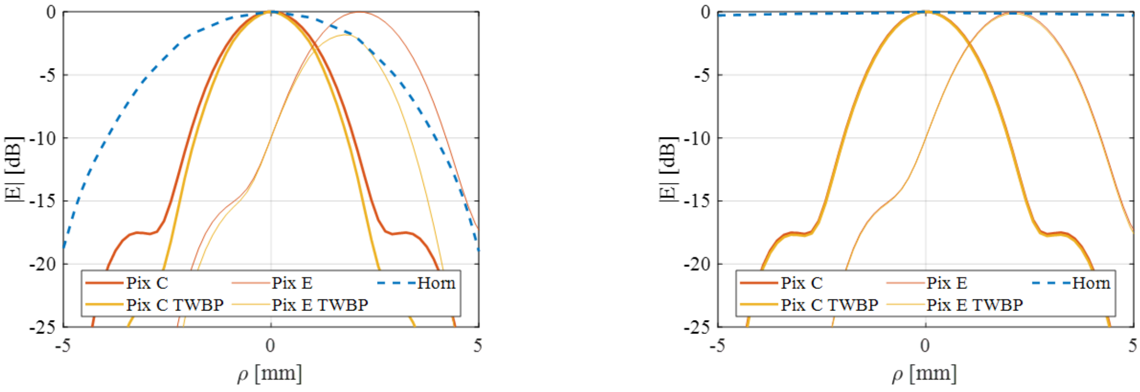

(a) Low $\Delta\rho^{src}_{HPBW}/\Delta\rho^{det}_{HPBW}$. **(b)** High $\Delta\rho^{src}_{HPBW}/\Delta\rho^{det}_{HPBW}$.

Figure 2.12: Effect of the illumination of the imaging plane on the TWBP.

In order to quantify these differences, the directivity of the TWBP is calculated for both the center and edge pixel. These directivities are compared with the directivity of their $\vec{E}^{im}_{det}$ pattern. Since the fields are not in the far field, the focused antenna directivity is used [25]. This focused antenna directivity is defined as:

$$D_{NF} = \frac{4\pi|\vec{S}(\vec{r}_{max})|r^2_{max}}{P_{rad}} \tag{2.10}$$

Where $\vec{S}(\vec{r})$ is the power of the fields in the imaging plane as in Equation 2.11, r_{max} is the distance from the biconvex lens to the imaging plane in the main axis, F_{BC2}, and P_{rad} is the power $\vec{S}(\vec{r})$ integrated over the imaging plane.

$$|\vec{S}(\vec{r})| = \frac{1}{2\zeta_0}|\vec{E}(\vec{r})|^2 \tag{2.11}$$

The focused antenna directivities of $\vec{E}_{det}^{im}$ for pixel C and pixel E are shown in Figure 2.13 with dotted lines. The directivities of the TWBP for pixel C and pixel E were calculated for different HPBW ratios and shown in the same figure.

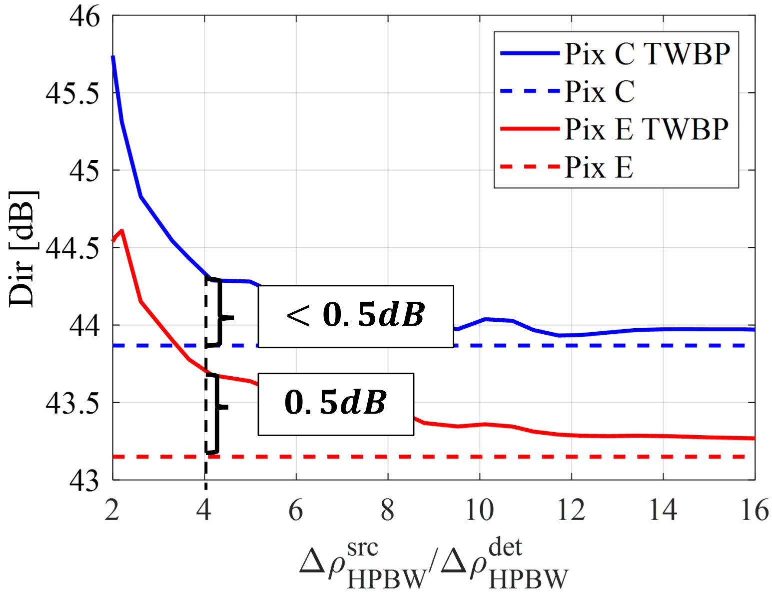

Figure 2.13: TWBP Directivities compared to the directivities of $\vec{E}_{det}^{im}$ for pixel C and pixel E.

As expected, the directivities of the TWBP approaches $\vec{E}_{det}^{im}$ for both pixels as the HPBW ratio increases. From Figure 2.13 it seems desirable to choose a large HPBW ratio. However, as discussed earlier, a large HPBW ratio will result in a low η_c. To analyse this trade-off, η_c was calculated using Equation 2.9 as a function of the same HPBW ratios and is shown in Figure 2.14. In this analysis, η_c was analysed for a detector that was aligned with the THz source, which is why η_c is 3dB higher than in 2.2, where a 45 degree rotation is applied for simultaneous illumination of all detectors.

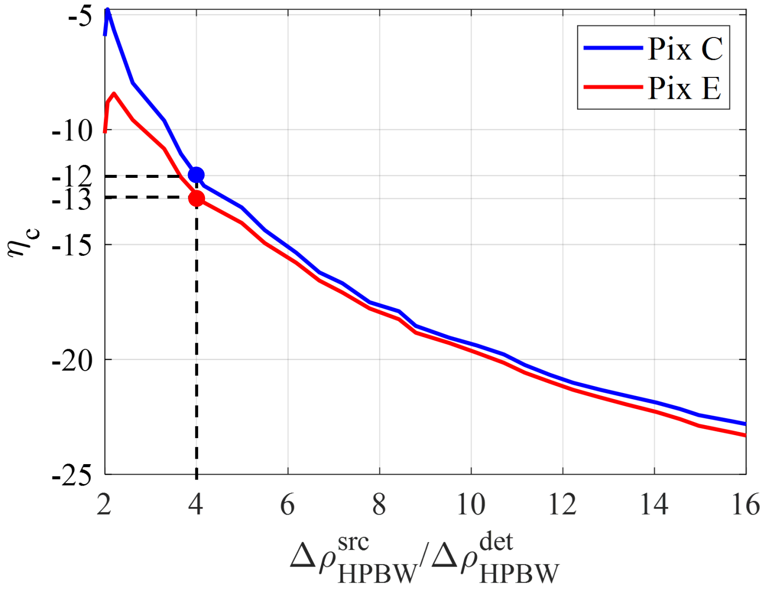

Figure 2.14: Coupling as a function of the ratio of HPBWs of the source and detector.

The ratio of HPBW between the detector and the source $\Delta\rho^{src}_{HPBW}/\Delta\rho^{det}_{HPBW}$ has been chosen such that the deviation in directivity between TWBP and $\vec{E}^{im}_{det}$ is at most 0.5dB for both the center and edge pixel (see Figure 2.13). This occurs for a HPBW ratio of 4. This corresponds to a coupling efficiency of -12dB and -13dB for the center and edge pixel, respectively. This means deviation between DR due to illumination is below 1dB. This threshold not only achieves a good uniform illumination, but also ensures that the resolution of the overall camera is given by the detector and not the source. The final parameters of the QO setup are shown in Table 2.1.

Table 2.1: Dimensions of the Implemented QO System.

Parameter	Dimension	Parameter	Dimension
D_{bc}	4.2 cm	d_v^{min}	1.07 mm
F_{bc1}	8.9 cm	d_i^{min}	1.27 mm
F_v	3.3 cm	F_{bc2}	10.5 cm
L_l	0.22 cm	D_{PC}	6 cm
R_l	0.75 cm	F_{PC}	2.96 cm
d_f^{min}	92.2 μm		

2.2 Power coupling of the QO setup

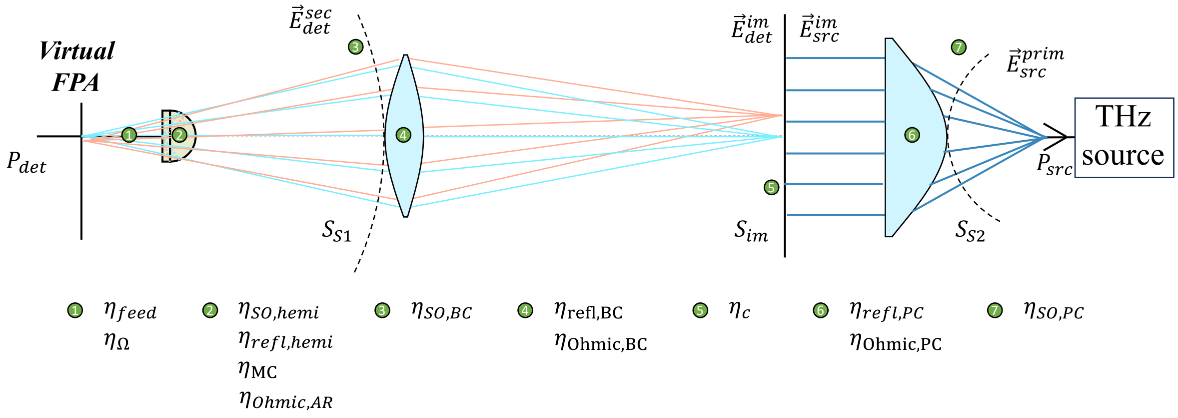

Figure 2.15: Overview of all loss contributions in the QO setup from the power radiated by the source P_{src} to the power arriving to the detector P_{det}.

In this Section, all loss contributions in the designed QO setup will be further elaborated on and the overall performance of the QO setup including the FPA and antenna losses will be presented. Figure 2.15 shows an overview of all these loss contributions. The overall performance is expressed as the overall power coupling of the full QO system, η_P^{QO}, which is defined as in Equation 2.12.

$$\eta_P^{QO} = \frac{P_{det}}{P_{src}} \tag{2.12}$$

In this equation, P_{det} is the power received from the detector, and P_{src} is the power transmitted by the source (see Figure 2.15).

Losses within hyperhemispherical lens and FPA chip

Figure 2.16 gives a more detailed view on the losses occurring within the hyperhemispherical lens and the FPA chip. η_{feed} is the feed efficiency in the FPA which accounts for the front-to-back ratio, losses in tiling of the CMOS architecture, conductor losses and losses in the silicon [11]. η_{Ω} is the impedance matching efficiency between the antenna and detector and η_{MC} represents the losses due to mutual coupling between the FPA elements. η_{feed}, η_{Ω} and η_{MC} were thoroughly characterized in [11] and also apply in the design with a hyperhemispherical lens since η_{feed}, η_{Ω} are independent of the lens geometry and η_{MC} as well when an infinite silicon medium is assumed.

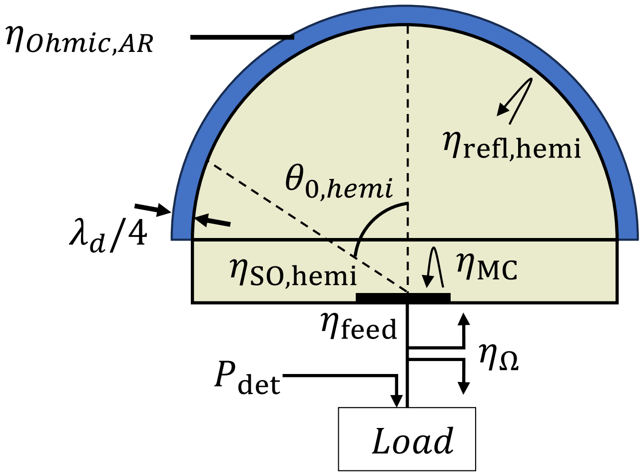

Figure 2.16: Losses from hyperhemispherical lens to detector.

$\eta_{ohmic,AR}$ represents the ohmic losses in the quarter wavelength parylene-C anti reflection coating. In [26], it was found that such an anti-reflection coating results in 1.6dB ohmic losses. $\eta_{SO,hemi}$ is the spillover efficiency of the radiation patterns inside the silicon medium of the hyperhemispherical lens while $\eta_{refl,hemi}$ represents the losses due to all reflections occurring from the silicon-air interface. To find $\eta_{SO,hemi}$ and $\eta_{refl,hemi}$, the power radiated by the hyperhemispherical lens, P_{hemi}, is calculated from the far field patterns of the hyperhemispherical lens using the PO tool presented in [22]. Then, the power radiated by the FPA in the silicon medium, P_{FPA} is calculated from the radiation patterns inside the silicon medium. The combined efficiency term is then calculated as in Equation 2.13.

$$\eta_{refl,hemi}\eta_{SO,hemi} = \frac{P_{hemi}}{P_{FPA}} \tag{2.13}$$

Altogether these terms give the aperture efficiency of the hyperhemispherical lens as in Equation 2.14

$$\eta_{ap} = \eta_{feed}\eta_{SO,hemi}\eta_{refl,hemi}\eta_{ohmic,AR}\eta_{MC} \tag{2.14}$$

The results are shown in Table 2.2.

Spillover losses

The spillover loses for the biconvex lens $\eta_{SO,BC}$ and planoconvex lens $\eta_{SO,PC}$ were calculated for the center frequency in Section 2.1.1 and 2.1.3, respectively, using Equation 2.5. The same analysis is repeated for 350 to 475 GHz. The results are shown in Table 2.2.

Reflection losses

$\eta_{refl,BC}$ is the total reflection loss (air to HDPE and HDPE to air) in the biconvex lens. After defining a lossless lens in GRASP, $\eta_{refl,BC}$ is calculated using:

$$\eta_{refl,BC} = \frac{\int\int_{S_{im}} |\vec{E}^{im}_{det}|^2 dS}{\int_0^{2\pi}\int_0^{\theta_0} |\vec{E}^{sec}_{det}|^2 sin\theta r^2 d\theta d\phi} \tag{2.15}$$

Where $\vec{E}^{sec}_{det}$ is evaluated on sphere S_{S1} (see Figure 2.15) and θ_0 is the subtended half-angle (see Figure 2.3) and r is the radius of sphere S_{S1}, which is F_{bc1}. Equation 2.15 expresses that when the lenses are free from ohmic losses, then the the reflection efficiency is equal to the ratio of power that arrives to the imaging plane versus the power entering the lens. $\eta_{refl,PC}$ is calculated following the same steps. The results are shown in Table 2.2.

Ohmic losses

$\eta_{ohmic,BC}$ is the ohmic efficiency in the biconvex and it is calculated as:

$$\eta_{ohmic,BC} = \frac{\int\int_{S_{im}} |\vec{E}^{im}_{det}|^2 dS|_{tan\delta=4\cdot 10^{-4}}}{\int\int_{S_{im}} |\vec{E}^{im}_{det}|^2 dS|_{tan\delta=0}} \tag{2.16}$$

This formula expresses that the ohmic efficiency of the biconvex lens is equal to the ratio of the power arriving to the imaging plane when the loss tangent $tan\delta$ is 0 versus when the loss tangent $tan\delta$ is $4\cdot 10^4$. The loss tangent of $tan\delta = 4\cdot 10^4$ is the loss tangent that was measured during the characterization of the material that was used to implement the hyperbolic lenses. $\eta_{ohmic,PC}$ is calculated following the same steps. The results are shown in Table 2.2.

Overview QO setup losses

An overview of all losses in the setup is given in Table 2.2. A visual representation of the losses is given in Figure 2.17. In this figure $\eta_{BC/PC}$ are the combined spillover, ohmic and reflection losses of the biconvex and planoconvex lenses. $\eta_{optical}$ is defined as the optical efficiency, as in:

$$\eta_{optical} = \eta_{BC}\eta_{c}\eta_{PC} \tag{2.17}$$

Using this expression, the overall power coupling of the full QO system, η_P^{QO}, can be expressed as $\eta_P^{QO} = \eta_{optical}\eta_{ap}$. This η_P^{QO} is shown in the bottom row of Table 2.2.

Table 2.2: summary of all losses in system.

Freq [GHz]	**350**	**375**	**400**	**425**	**450**	**475**
$\eta_{\Omega}[dB]$	-1.04	-0.92	-0.83	-0.79	-0.80	-0.85
$\eta_{feed}[dB]$	-1.86	-1.86	-1.86	-1.87	-1.90	-1.93
$\eta_{SO,hemi}$ [dB]$\eta_{refl,hemi}[dB]$	-0.40	-0.40	-0.40	-0.40	-0.40	-0.40
$\eta_{MC}[dB]$	-1.60	-1.24	-0.98	-0.80	-0.66	-0.56
$\eta_{ohmic,AR}[dB]$	-1.60	-1.6	-1.6	-1.6	-1.6	-1.6
$\eta_{SO,BC}[dB]$	-0.30	-0.23	-0.17	-0.15	-0.14	-0.14
$\eta_{refl,BC}[dB]$	-0.47	-0.45	-0.44	-0.42	-0.42	-0.41
$\eta_{ohmic,BC}[dB]$	-0.15	-0.16	-0.18	-0.19	-0.20	-0.22
$\eta_{c}[dB]$	-14.55	-14.70	-14.92	-15.01	-14.85	-15.00
$\eta_{refl,PC}[dB]$	-0.52	-0.35	-0.44	-0.21	-0.49	-0.42
$\eta_{ohmic,PC}[dB]$	-0.30	-0.31	-0.34	-0.35	-0.39	-0.41
$\eta_{SO,PC}[dB]$	-0.05	-0.04	-0.03	-0.03	-0.0	-0.04
$\boldsymbol{\eta_P^{QO}}[dB]$	**-22.84**	**-22.26**	**-22.19**	**-21.82**	**-21.89**	**-21.98**

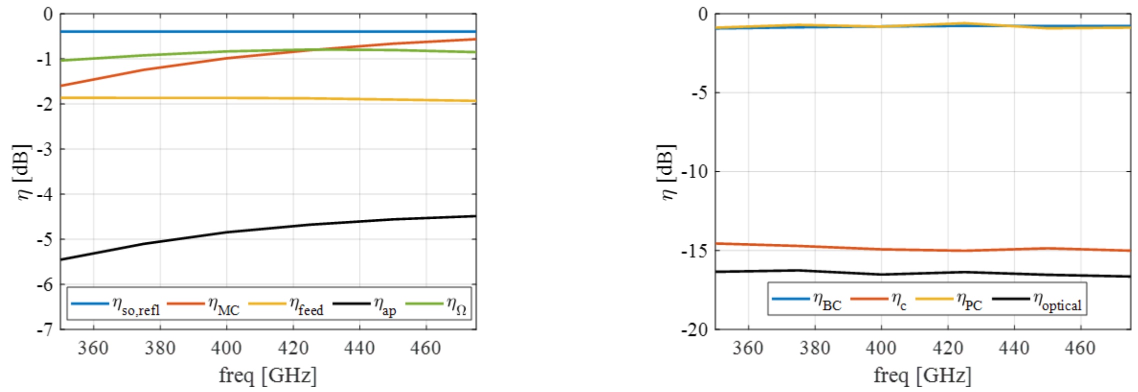

(a) Aperture and matching efficiency.

(b) Efficiencies of biconvex and planoconvex lenses.

Figure 2.17: Visual respresentation of losses in the QO system.

Chapter 3

Practical Implementation of the QO Imaging System

This chapter describes the procedure to implement the QO imaging setup described in Chapter 2. First, a schematic overview of the overall implementation and working principles will be introduced. Second, the detector architecture of the FPA camera in CMOS technology is explained, as well as its operation and performance metrics. Third, the implementation of the 12 pixel FPA is shown. For this setup, an electronically controlled switching architecture was realized to read the 12 pixels. Finally, the steps for aligning the QO setup are presented and an estimate of the accuracy is given for each alignment step.

3.1 QO setup with CMOS Array Architecture Implementation

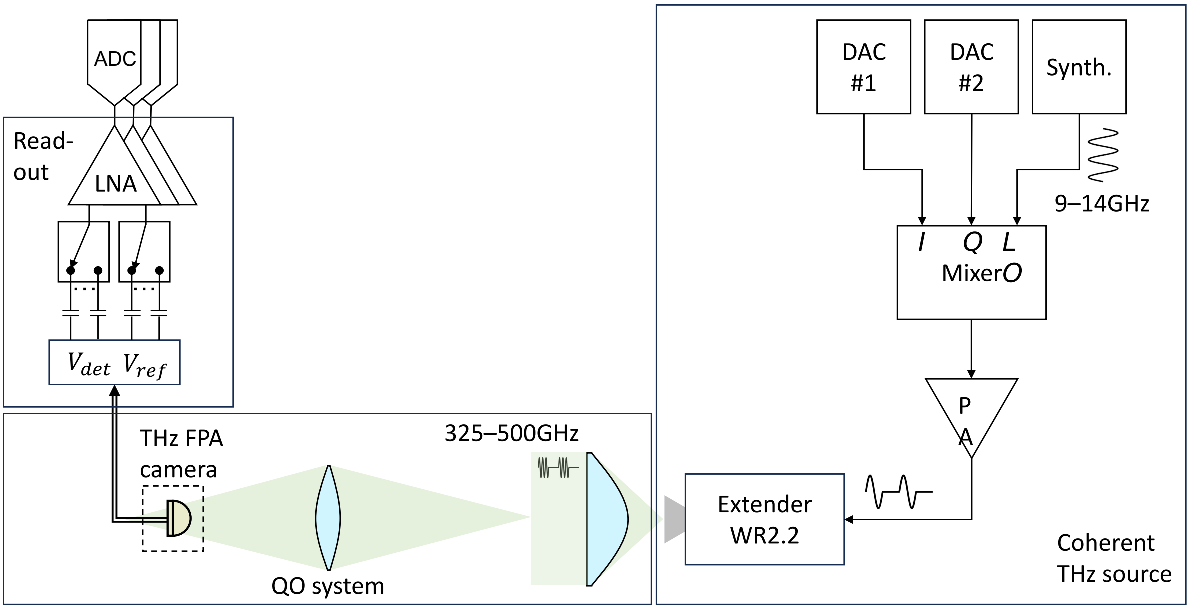

Figure 3.1: A schematic overview of the implementation of the QO Imaging System with the CMOS passive imager array, subdivided into the source module, QO setup module and read-out module.

The implementation of the QO imaging system, including the CMOS-integrated array, is shown in Figure 3.1. It is composed of the QO system which includes the THz FPA camera, the readout for the camera, and the implementation of the coherent THz source. The source is composed of a WR2.2 frequency extender equipped with a 20dB standard gain horn. The multiplication factor of the extender module is 36, and thus the frequency at its input should range between 9 and 14 GHz. This 9-14 GHz CW signal is generated by an Anritsu MG3694A synthesizer and is of-off modulated in order to separate the detected signal from flicker noise and increase the DR [11]. The modulation is implemented with an IQ mixer which is controlled by 2 DACs. To get a high quality off-state, the I and Q values are chosen to produce a minimal power at the output. During the on-state, one DAC maintains a constant value while the other DAC generates a signal that will drive the extender in saturation mode. The procedure for finding the appropriate I and Q voltages was described in [11]. A modulation frequency, f_{MOD}, of 1 MHz was selected since this achieves the highest dynamic range in this particular setup [11].

3.2 THz FPA camera

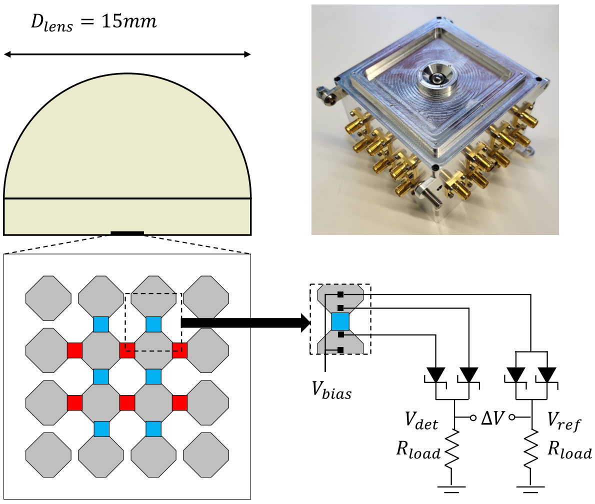

Figure 3.2: Schematics of a detector.

Figure 3.2 shows a schematic overview of the 12 pixel antenna coupled detector array implemented in 22nm silicon-on-insulator (FD-SOI) CMOS technology. It is composed of an array of 45 degree tapered dipole antennas. The dual-polarized array geometry results in a tight sampling of the focal plane, yielding a (near) diffraction-limited angular resolution. Each antenna is connected to a direct-detector. The detector architecture consists of a pseudo differential Schottky barrier diode (SBD) detection circuit [12] as shown in the bottom in Figure 3.2. The pseudo-differential read-out limits common mode noise. The SBDs generate a current response at DC ΔI_{det} when power P_{det} is absorbed by the array element. The load resistor R_{load} is used to convert this current response into a voltage response, ΔV. The voltage over the resistor R_{load} of the detector branch is called V_{det}, it is a summation of the voltage V_0 and ΔV caused by P_{det}.

A reference branch is added, which contains identical and equally biased SBDs and is not connected to the antenna terminals [27]. Since this branch has the same biasing current, and thus an identical voltage drop V_0 over the R_{load} in the reference branch, this allows for a pseudo-differential readout so that ΔV can be found between the reference and detector terminal.

Thus, the voltage response ΔV has a direct relation to P_{det}. This relation is expressed with the responsivity $\Re_{v,det}$ as in:

$$\Re_{v,det} = \frac{\Delta V}{P_{det}} \tag{3.1}$$

$\Re_{v,det}$ has been characterized extensively in [12] and the simulation is shown in Figure 3.3a.

The detector and reference voltage are then pseudo-deferentially amplified using a LNA so that the output of the LNA, $\Delta V'_{out}$, is defined as in Equation 3.2.

$$\Delta V'_{out} = G_{LNA}\Delta V = G_{LNA}\Re_{v,det}P_{det} \tag{3.2}$$

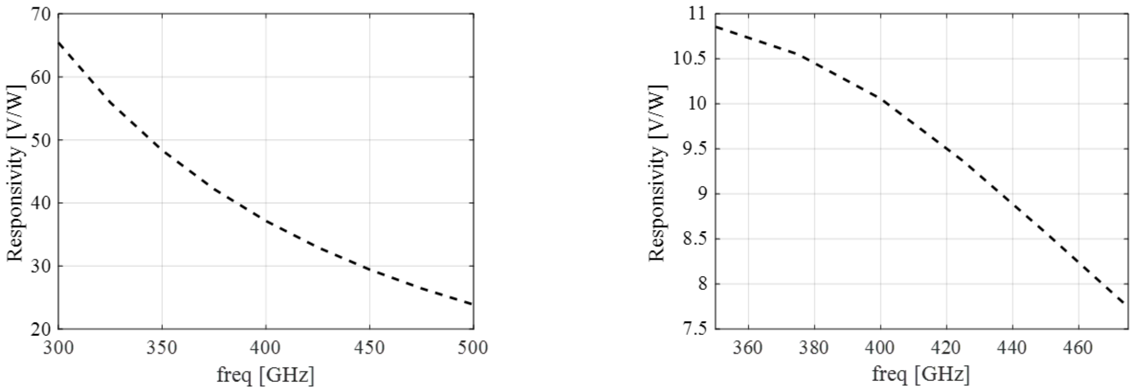

(a) $\Re_{v,det}$ versus frequency.

(b) $\Re_{v,sys}$ versus frequency.

Figure 3.3: Detector and system responsivities.

Where G_{LNA} is the gain of the LNA. The gain of the LNA is set to 40dB, yielding a bandwidth of 8 MHz, which is sufficient to amplify the modulation frequency [28]. The relation between the power coupled by the hemispherical lens, P_{in} (see Figure 3.4), and P_{det} is given by:

$$P_{det} = \eta_{ap}\eta_{\Omega}P_{in} \tag{3.3}$$

Where η_{Ω} is the impedance matching efficiency and η_{ap} is the aperture efficiency of the hyperhemispherical lens as described in Section 2.2. Filling in Equation 3.3 into Equation 3.2 gives:

$$\Delta V'_{out} = G_{LNA}\Delta V = G_{LNA}\Re_{v,det}\eta_{ap}\eta_{\Omega}P_{in} \tag{3.4}$$

The system responsivity is then defined as in Equation 3.5

$$\Re_{v,sys} = \eta_{ap}\eta_{\Omega}\Re_{v,det} = \frac{\Delta V'_{out}}{G_{LNA}P_{in}} \tag{3.5}$$

By multiplying η_{Ω} and η_{ap} from Section 2.2 with $\Re_{v,det}$ from Figure 3.3a, $\Re_{v,sys}$ is obtained and shown in Figure 3.3b. With these steps the relationship between P_{det}, P_{in} and $\Delta V'_{out}$ is defined.

3.3 Read-out architecture

3.3.1 Signal detection

Since the THz source is on-off modulated, $\Delta V'_{out}$ needs to be retrieved from the measured square wave at the ADC. Equation 3.2 and 3.5 only describe the relation between P_{det}, P_{in} and $\Delta V'_{out}$ when the THz source is in on-state. This section will explain how $\Delta V'_{out}$ is extracted from the measured square wave at the ADC.

Figure 3.4 shows how the signal of interest travels from the aperture of the lens to the readout. The on-off modulated signal results in a square wave with amplitude $\Delta V'_{out}$. The ADCs sample the output signal, which fluctuates between $\Delta V'_{out}$ during on-state and the noise floor during off-state. Then the Fourier transform of the signal is taken and evaluated at f_{MOD}. By using the property that the fundamental tone of a square wave is a factor π smaller than the amplitude of the square wave, $\Delta V'_{out}$ is found without suffering from 1/f noise.

With these steps a method is presented for retrieving $\Delta V'_{out}$ from the measurements, and thus P_{det} and P_{in} can also determined through measurements.

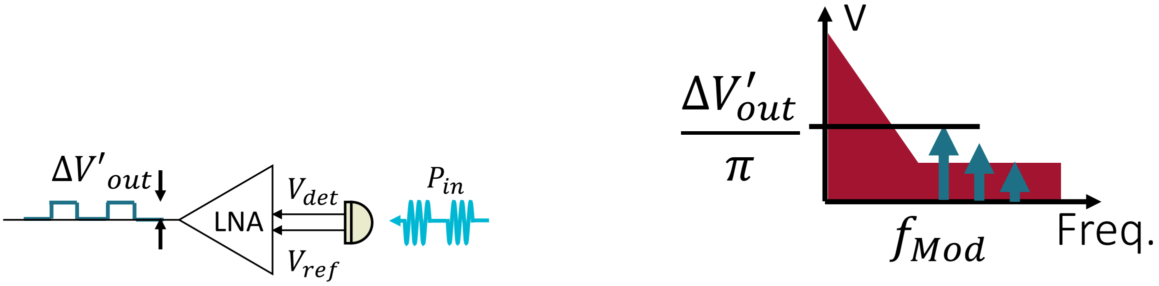

(a) Square wave from the input power.

(b) Spectrum from square wave, including noise.

Figure 3.4: Signal detection from the square wave at the output of the LNA (a) and the corresponding spectrum (b), which shows that the amplitude of the square wave is related to the amplitude of the fundamental tone.

3.3.2 Design of electronic switching system

To generate an image, all twelve pixels should be read out as quickly as possible. Due to practical considerations, only 3 ADCs can be used simultaneously. As a result, an electronic switching system needs to be implemented to allow automated readout. The switching system multiplexes these outputs over three LNAs, of which the outputs can be subsequently digitized by the ADCs.

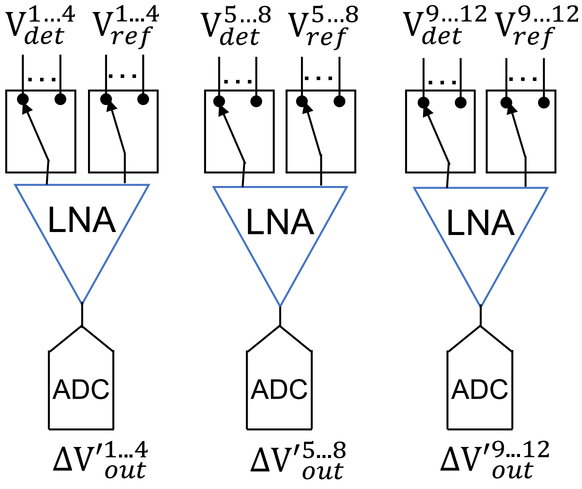

Figure 3.5: Schematics of a switching architecture.

Figure 3.5 shows a schematic overview of the switching system. In total 6 switches were used. Each LNA is driven by a pair of switches, one switch multiplexes the V_{det} ports, while the other switch multiplexes the V_{ref} ports. The switch that was used is the Agilent 87204. This is a mechanical switch, which are designed for minimal signal degradation. The switches were controlled using an Agilent 11713A Attenuator/Switch Driver, remotely controlled via a GPIB interface, allowing for automated readout of all pixels.

3.3.3 DC Blocks

When the switches are in open-path mode, the paths are terminated with $R_{switch} = 50\Omega$, which is illustrated in Figure 3.6. This means that when the pixels are not read out, the $2k\Omega$ load resistance R_{load} is in parallel with the 50Ω switch resistance. This results in high currents flowing through the SBDs for which the system was not designed. To prevent this, a BLK-89-S+ DC block is placed between each output of the pixels and the inputs of the switch. The DC block exists of a capacitor connected to SMA connectors, which creates a high-pass filter with a cut-off frequency of 100kHz, normalized to 50Ω, like R_{switch}. When the detector or reference branch is connected to the LNA, the capacitor is put in series with the LNA input impedance. The LNA input impedance is in the order of $G\Omega$s and thus considerably higher than 50 Ω. This will lower the cutoff frequency significantly. However, this is not an issue since the only task of the DC block is to remove the DC component of the signal.

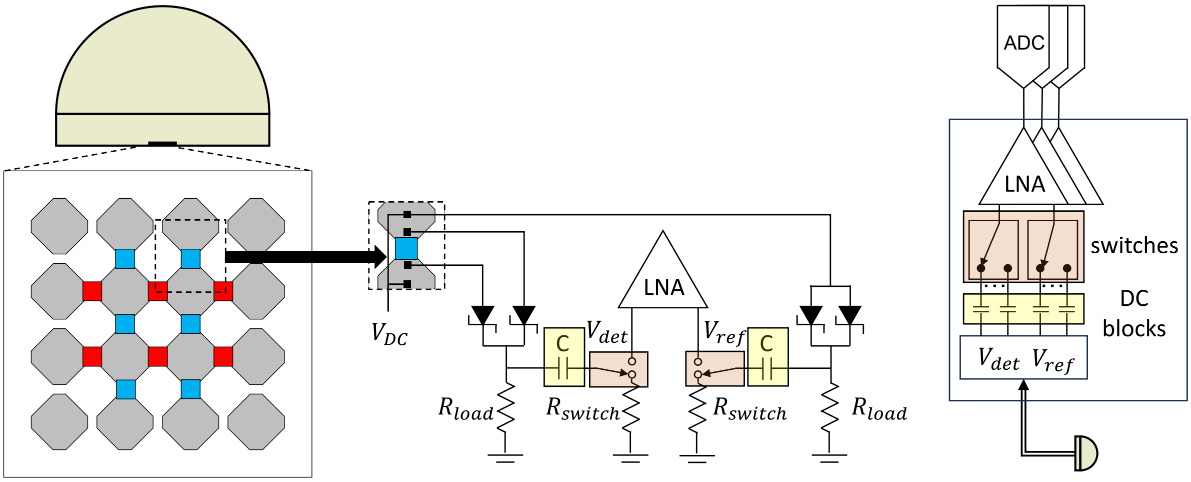

Figure 3.6: Schematics of a switching architecture.

3.4 Fabrication and assembly

This section first introduces the assembled QO imaging setup. Second, the design and motivation of the components of the QO imaging setup are explained. Finally, an overview of the alignment steps is presented, including the accuracies.

Figure 3.7 shows and overview of the QO imaging setup, assembled on an optical table. The holes in the optical table form a reference point so that alignment is easier. The holes also ensure that there are minimal angular errors: the planoconvex lens and biconvex lens can be assumed to be near parallel because they are attached to the same optical table.

The FPA is integrated with the hyperhemispherical lens following identical steps as in [11]. The THz camera is held in place with a 3D-printed stand. The stand is designed so that it can hold the camera at different orientations with regular 45 degree intervals, for testing different polarizations. The orientation that is chosen is such that both polarizations are illuminated equally by the THz source. The switches are organized in a second stand shown in the back of Figure 3.7. All 3D printed parts have a tolerance of less than 0.2 mm. Both hyperbolic lenses were manufactured using a CNC milling process. The used material of the lenses is HDPE. The subject to be imaged is put in an envelope and attached to a CNC machine using an extension arm, which allows it to move the object within the imaging plane.

Since the focus of the biconvex lens should coincide with the focus of the hyperhemispherical lens, the alignment of the biconvex lens was the most critical part. Thus, it was desirable to have freedom

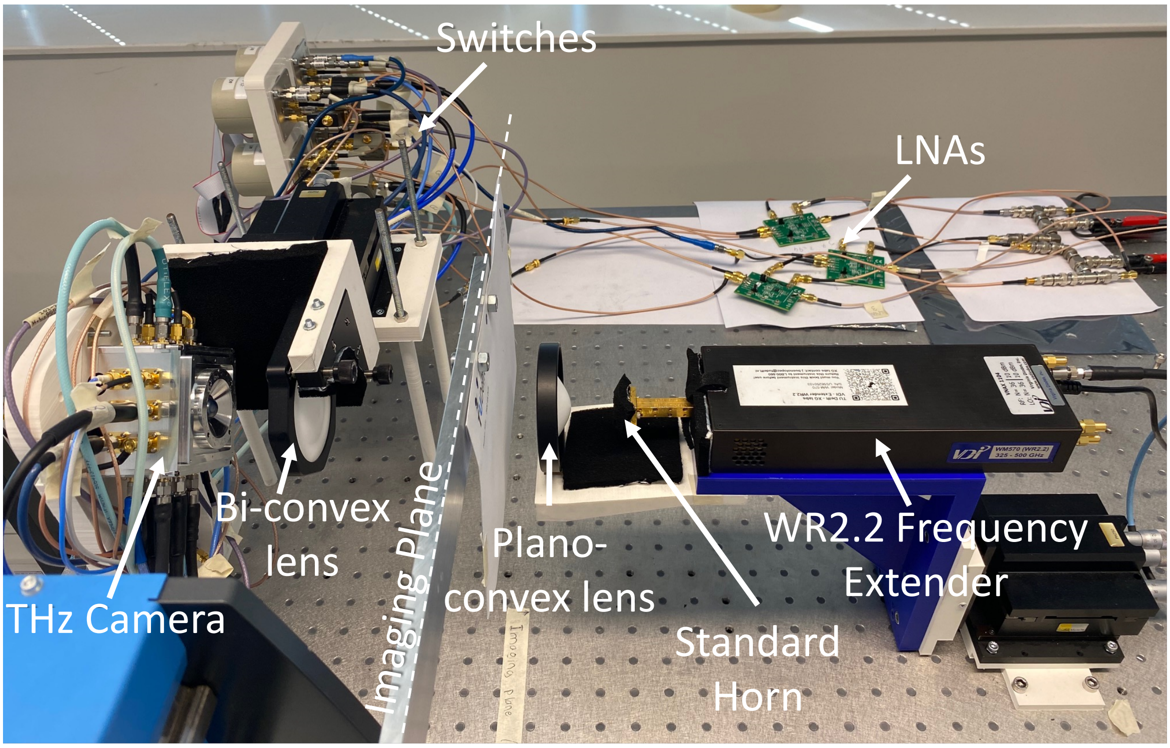

Figure 3.7: Image of the fabricated and assembled quasi-optical setup.

of movement in all axis to overcome any misalignment due to tolerances in any dimensions in the setup. Therefore, the lens was held by a KS3 lens-holder from Thorlabs, which allowed for rotational alignment ((θ,ϕ), see Figure 3.8). The KS3 holder was attached to a 3-axis stage via a 3D-printed part. The 3-axis stage allowed for translational alignment ((x,y,z), see Figure 3.8). The 3-axis stage was put on a 3D-printed table that was attached to the optical table. The biconvex lens could then be aligned in five axes, as shown in Figure 3.8.

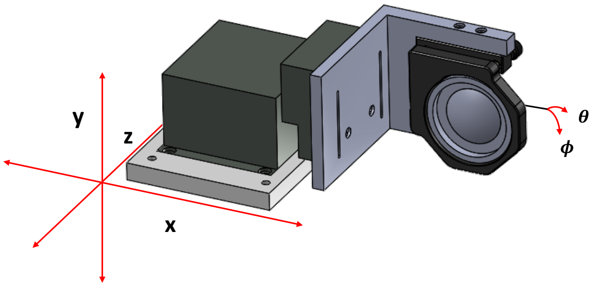

Figure 3.8: Designed component for to allow 5 axis of alignment for biconvex lens.

The planoconvex lens was placed in an LMR3 lens holder from Thorlabs, as shown in Figure 3.9. To ensure proper alignment between the planoconvex lens w.r.t. the horn, a 3D-printed part was designed. The 3D-printed part ensured proper rotational alignment with a cavity with the exact thickness of the LMR3, which prevents rotation in undesired direction. The 3D-printed part ensured proper translational alignment by attaching to the extender and keeping the lens at a fixed location. This ensured translational alignment of the lens w.r.t. the horn with an accuracy of 0.2mm, which is the tolerance of the 3D printer. The extender was mounted to a 3-axis stage via two 3D-printed parts. The 3-axis stage allowed for alignment of the horn and planoconvex lens w.r.t. the imaging plane. This freedom of movement enables moving the collimated beam in the imaging plane to illuminate all pixels in the imaging plane as uniform as possible.

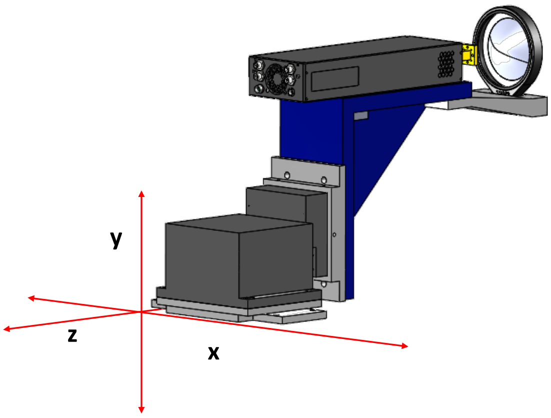

Figure 3.9: Designed component for to allow 3 axis of alignment for horn and PC lens.

3.4.1 Alignment biconvex lens

To realize the alignment and characterize the radiation patterns of the 12 pixel camera in the imaging plane, the setup in Figure 3.10 was built. The biconvex lens and THz camera are still in place, but the planoconvex lens is removed. The horn is attached to a CNC to scan the radiation patterns in the imaging plane.

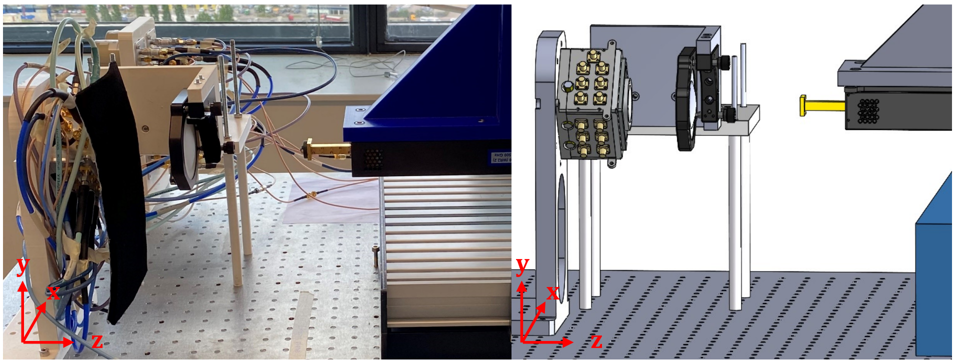

Figure 3.10: Overview of measurement setup for measuring radiation patterns. Using bolts in the optical table, alignment of the CNC is ensured.

For practical considerations, soft alignment points are introduced to perform the alignment. Soft alignment points are used when one of the original distances in the design of the QO system is difficult to measure (e.g. distance between tips of two lenses). The soft alignment points use the distance between two alternative locations in the setup that are easier to measure, yet still ensures the requirement on the original distance is met.

The soft alignment point for the biconvex lens in z-direction (see Figure 3.10) is the distance between the rectangular rim on the THz camera, and the surface of the KS3 as shown in Figure 3.11.

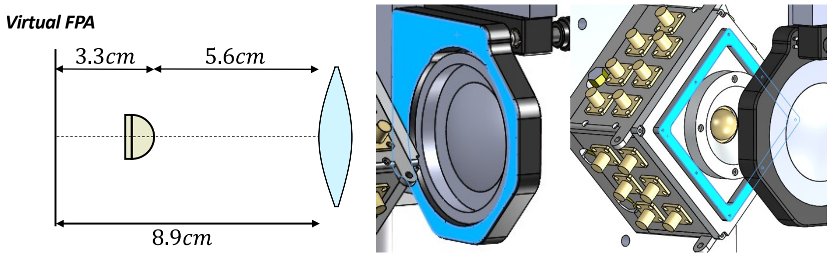

Figure 3.11: Soft alignment point distance hemispherical lens and biconvex lens.

The nominal distance was 53.85mm and the measured distance was 53.7mm. The accuracy of the physical alignment, done using a caliper, is .25mm.

The second soft alignment point for the biconvex lens in y-direction (see Figure 3.10) is the height of the KS3 lens-holder above the optical table, as shown in Figure 3.12a. The nominal distance was 176.89mm and the measured distance was 176.8mm. The accuracy of the physical alignment, done using a ruler, is 0.5mm.

The third and final soft alignment point for the biconvex lens in x-direction (see Figure 3.10) is the distance between the KS3 projected onto the optical table and one of the holes in the optical table, as shown in Figure 3.12b. The nominal distance was 2.3mm and the measured distance was 2.43mm. and has an estimated accuracy of 0.5mm. The accuracy of the physical alignment, done using a caliper, is 0.5mm.

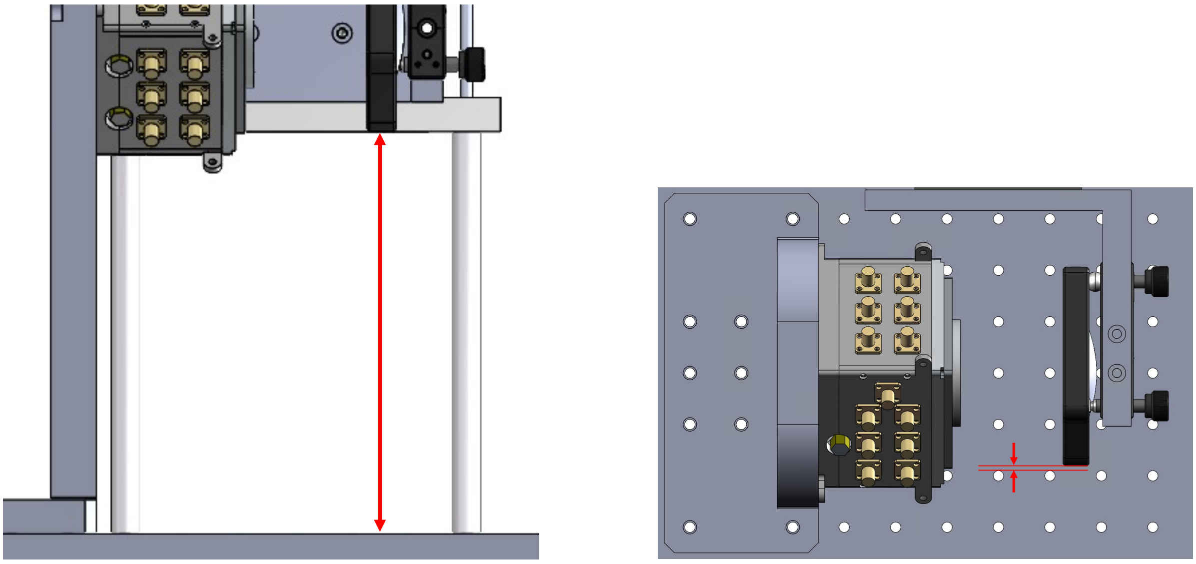

(a) Soft alignment point in y-alignment biconvex lens.

(b) Soft alignment point in x-alignment biconvex lens.

Figure 3.12: Soft alignment points for x- and y- alignment of the biconvex lens.

Another inaccuracy in the x and y alignment of the biconvex lens is caused by the deviation of the radius of the lens w.r.t. the radius of the KS3 lens holder. The biconvex lens has a radius of 23.9mm while the lens holder has a radius of 37.5mm. To minimize the possible error, a flat ring is put around the biconvex lens with a radius of 37.3mm. This means that there is still freedom of movement of ±0.2mm in both x and y direction, as shown in Figure 3.13. Adding this to the accuracy of the alignment in x-direction gives an overall accuracy of 0.7 mm.

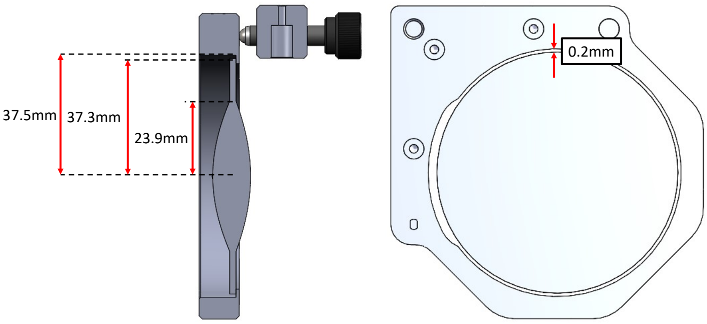

Figure 3.13: Uncertainty due to lens size.

The rotational alignment of the KS3 was set to 0, as the optical table was assumed to ensure good rotational alignment.

Next, the horn will be aligned w.r.t. the biconvex lens in z-direction (see Figure 3.10). The soft alignment point is the distance between the waveguide to which the horn is attached and the surface of the KS3 (see Figure 3.14). The nominal distance was 116.55mm and the measured distance was 116.7mm. The accuracy of the physical alignment, done using a caliper is 0.25mm. Since this setup will be used for 2D scans, no alignment in the x and y plane is necessary.

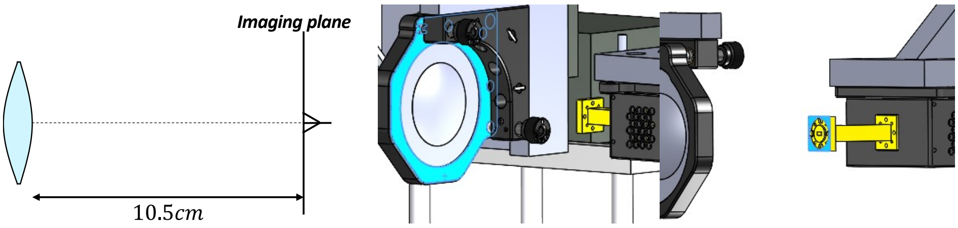

Figure 3.14: Alignment of distance between horn and biconvex lens.

After the measurements of the radiation patterns, the location of the horn in z-direction was projected on the optical table using a ruler and marked with tape on the optical table, as shown in Figure 3.7. This location is defined as the imaging plane.

3.4.2 Alignment planoconvex lens and THz source

For the complete imaging system, the planoconvex lens should be properly aligned to illuminate the imaging plane uniformly. The ideal location for the center of the planoconvex lens is middle of all measured radiation patterns, as this assures the most uniform illumination. The locations of the radiation pattern peaks of the 4 center pixels were used to determine where the center of the planoconvex lens should be placed. To find the location of these peaks w.r.t. reference points in the setup, the horn was put at the location where the peaks were measured. The locations of the peaks in x direction are found by projecting the center of the horn to the optical table and measuring w.r.t. one of the holes, as shown in Figure 3.15. The location of the peaks in y direction are found directly by measuring the distance between the center of the horn and the optical table. The planoconvex lens was then placed at the center of these locations. The alignment in z direction does not need

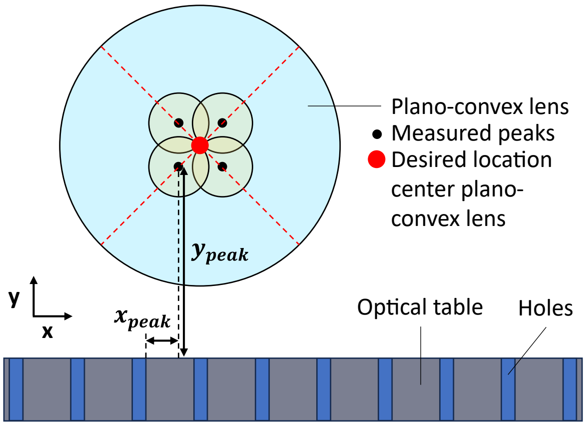

Figure 3.15: Alignment of planoconvex lens.

high precision since the planoconvex lens produces a collimated beam. For practical reasons, the lateral distance of planoconvex lens to the imaging plane was set to be 2 cm.

After performing this alignment, the freedom of movement in translational alignment provided by the structure shown in Figure 3.9 was used to minimize difference in received power between all 12 pixels with no object in the imaging plane.

Overall, the accumulated worst-case deviation is around 0.7 mm, for the biconvex lens alignment in x-direction. After the alignment procedure, the 3-axis stage of the biconvex lens should therefore not be moved more than this 0.7 mm. The alignment of the illumination is less precise and should result in all pixels being illuminated as equal as possible.

Chapter 4

Characterization of the QO imaging system

In order to validate the QO imaging system, the radiation patterns in the imaging plane and the coupling efficiency were measured. To measure the patterns, a planar scan was performed in the imaging plane with the horn antenna as explained in Section 3.4.1 and shown in Figure 4.1. From these patterns, the directivity, $\Delta\rho^{det}_{HPBW}$ and standing wave effects are extracted. Finally, using a noise measurement and the received power, the dynamic range of the setup is estimated.

4.1 Radiation patterns

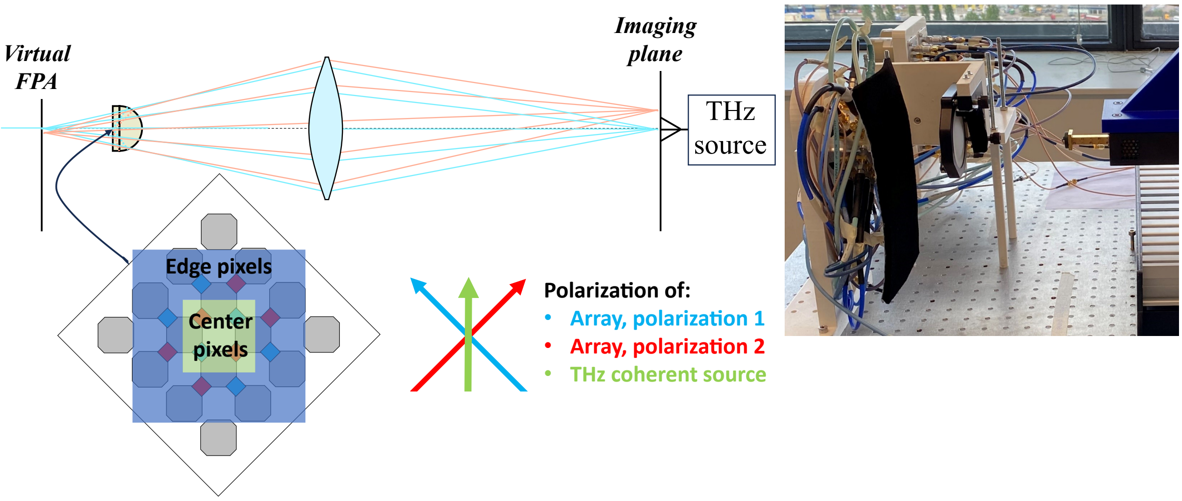

Figure 4.1: schematic overview and photograph of setup used to measure patterns in the imaging plane. The array is oriented to couple both polarizations equally to the coherent THz source.

The detector radiation patterns in the imaging plane, $\vec{E}^{im}_{det}$, have been measured between 350 and 475 GHz, with 25 GHz intervals. Besides these frequencies, the patterns have also been measured at ±1 GHz and ±2 GHz w.r.t. the previously mentioned frequencies to investigate the impact of standing waves. The patterns were measured by doing a planar scan with the horn in the imaging plane using a CNC machine. The CNC was moved in steps of 0.2mm in x and y directions in the imaging plane. For each location (x_i, y_i) value, the output voltage $\Delta V'_{out}(x_i, y_j)$ of each pixel of the array was measured. Using this voltage response, $P_{in}(x_i, y_i)$ was calculated using Equation 3.5.

In Appendix B the influence of the horn is investigated by calculating the coupling between the horn and equivalent aperture of the biconvex lens via a reaction integral and comparing it to $|\vec{E}^{im}_{det}|^2$ in the imaging plane. It is concluded that $|\vec{E}^{im}_{det}|^2$ is a good approximation for $P_{in}(x_i, y_i)$. Since $\Delta V'_{out}(x_i, y_j)$ is linearly related to $P_{in}(x_i, y_i)$, it is also directly proportional to the electric field radiation pattern $|\vec{E}^{im}_{det}|^2$ and therefore $\Delta V'_{out}(x_i, y_j)$ can be used to directly characterize $|\vec{E}^{im}_{det}|^2$.

Figure 4.2 shows the measured and simulated 2D patterns of the detector in the imaging plane, each normalized to the maximum magnitude of its signal strength. The measured patterns show one of the center and edge pixels and one of each polarization, red and blue (see Figure 4.1). The simulation corresponds to the virtual center pixel in the red polarization, $|\vec{E}_{det}^{im}|^2$, via the simulation approach explained in Chapter 2. As shown, the agreement in 2D is good across the band, showing a 90° rotation of the patterns between the red an blue polarization, as expected.

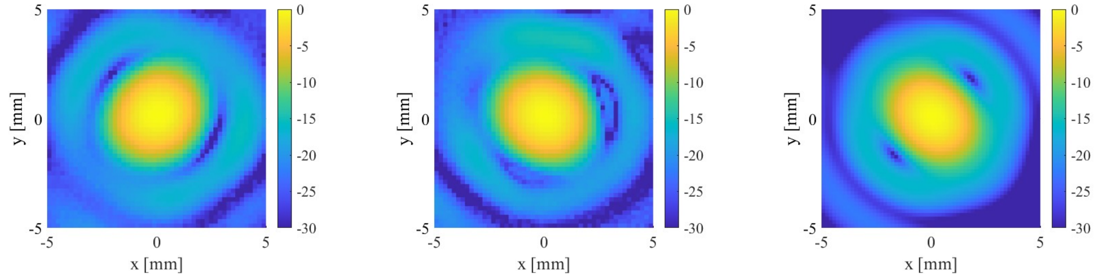

(a) center pixel, 350 GHz, pol. blue. **(b)** edge pixel, 350 GHz, pol. red. **(c)** simulation, 350 GHz, pol. red.

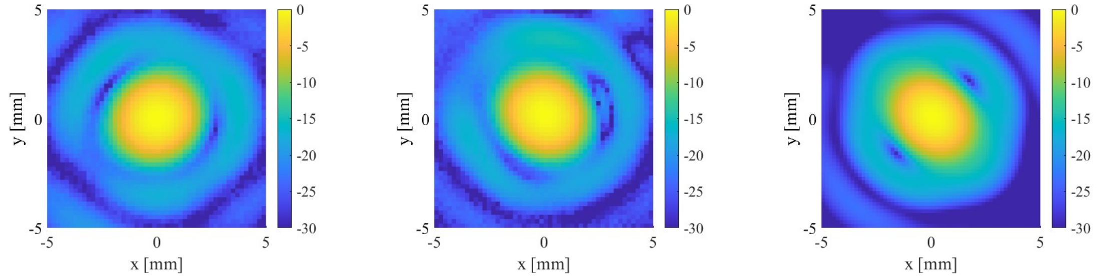

(d) center pixel, 375 GHz, pol. blue. **(e)** edge pixel, 375 GHz, pol. red. **(f)** simulation, 375 GHz, pol. red.

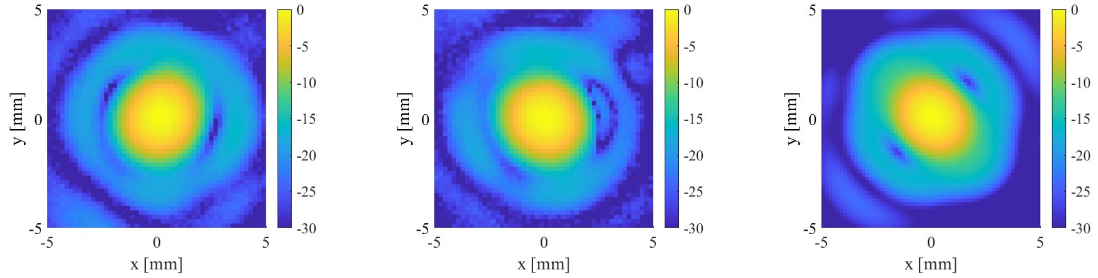

(g) center pixel, 400 GHz, pol. blue. **(h)** edge pixel, 400 GHz, pol. red. **(i)** simulation, 400 GHz, pol. red.

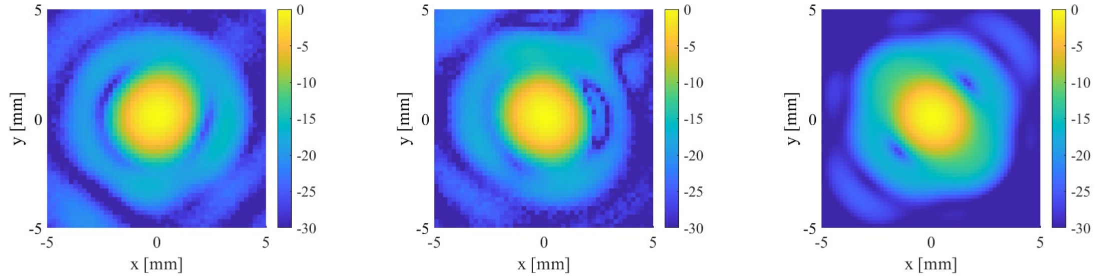

(j) center pixel, 425 GHz, pol. blue. **(k)** edge pixel, 425 GHz, pol. red. **(l)** simulation, 425 GHz, pol. red.

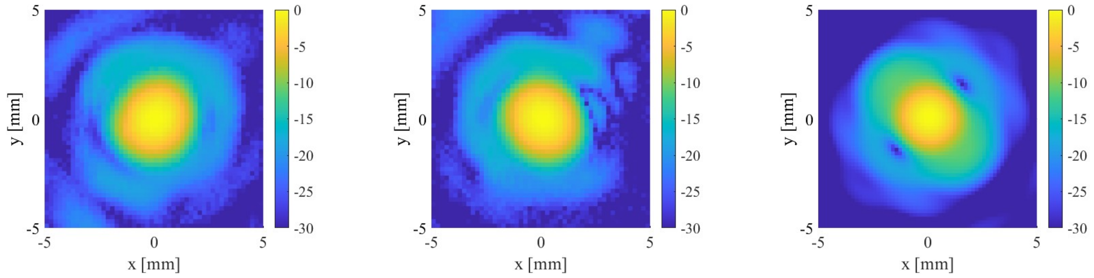

(m) center pixel, 450 GHz, pol. blue. **(n)** edge pixel, 450 GHz, pol. red. **(o)** simulation, 450 GHz, pol. red.

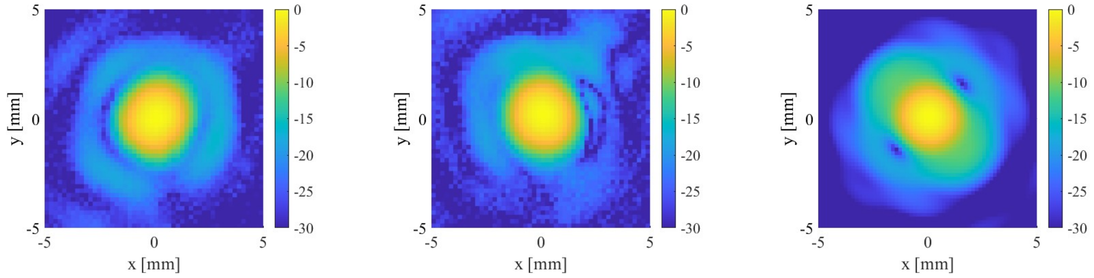

(p) center pixel, 475 GHz, pol. blue. **(q)** edge pixel, 475 GHz, pol. red. **(r)** simulation, 475 GHz, pol. red.

Figure 4.2: measured and simulated 2D patterns in imaging plane for different frequencies.

Figure 4.3 compares the cuts of the measured and simulated patterns in the E-, H- and D-planes of the same pixels as shown in Figure 4.2. The overall agreement between simulation and measurement in the cuts is good considering the fact that the simulations do not take into account the reflections (i.e. standing wave effects), spillover and diffraction of the overall QO setup.

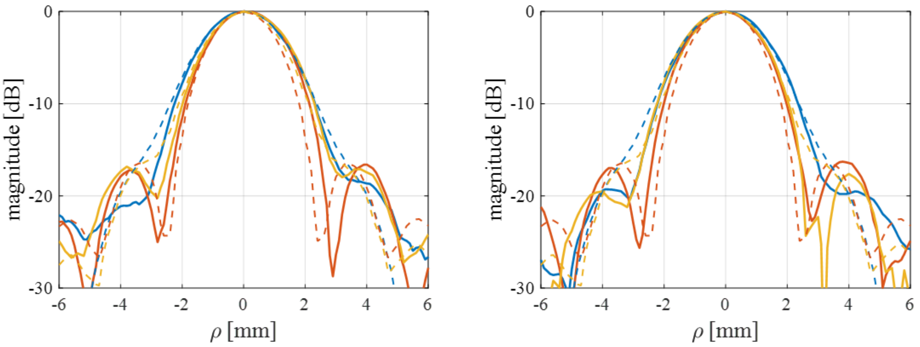

(a) center pixel, 350 GHz. **(b)** edge pixel, 350 GHz.

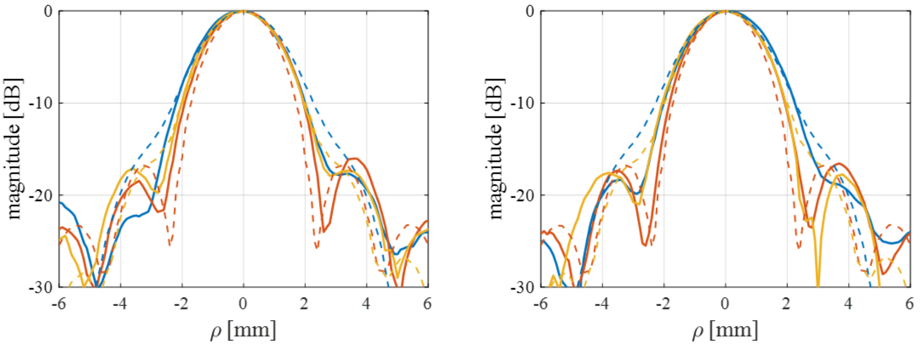

(c) center pixel, 375 GHz. **(d)** edge pixel, 375 GHz.

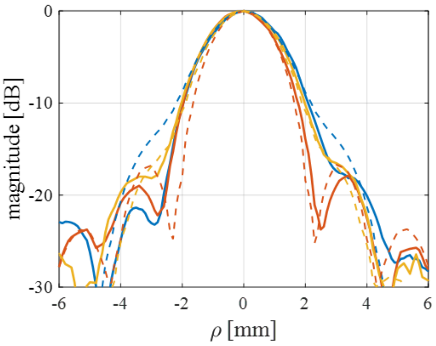

(e) center pixel, 400 GHz. **(f)** edge pixel, 400 GHz.

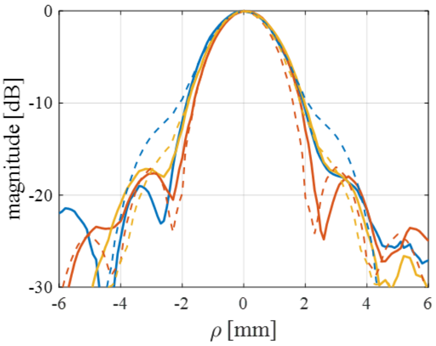

(g) center pixel, 425 GHz. **(h)** edge pixel, 425 GHz.

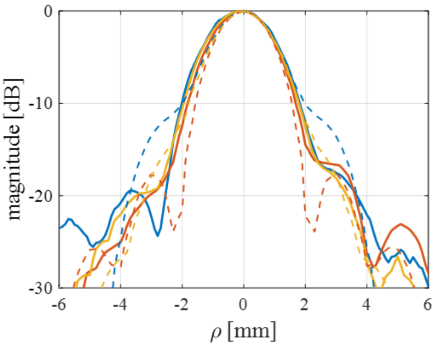

(i) center pixel, 450 GHz. **(j)** edge pixel, 450 GHz.

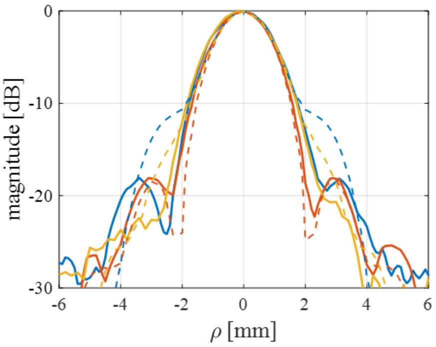

(k) center pixel, 475 GHz. **(l)** edge pixel, 475 GHz.

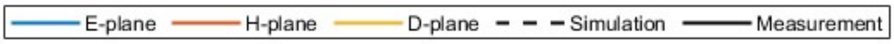

(m) Legend.

Figure 4.3: Measured versus simulated radiation patterns.

Figure 4.4 shows the combined measured detector patterns in the imaging plane for all considered frequencies. The figure also shows cuts of 4 adjacent pixels along the dotted black line for each frequency. The inter-element distance in the imaging plane, d_i can be seen to be around 1.33 mm, which is slightly above the predicted 1.27 mm (see Table 2.1). This can be explained by a deviation in the dielectric constant of the hyperbolic lenses, as explained in Appendix A, which resulted in a larger F_{bc2} and thus a larger inter-element distance in the imaging plane given that $d_i = \frac{F_{bc2}}{F_{bc1}} d_v$.

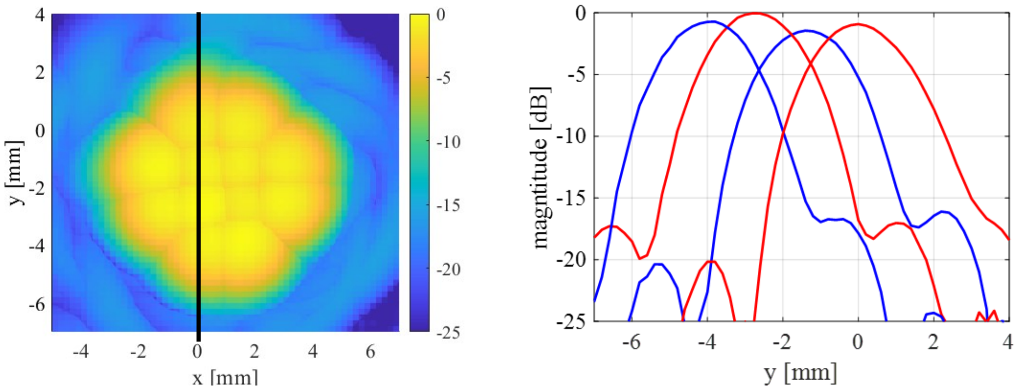

(a) 2D plot of combined patterns at 350 GHz.

(b) Cut of 4 radiation patterns at 350 GHz.

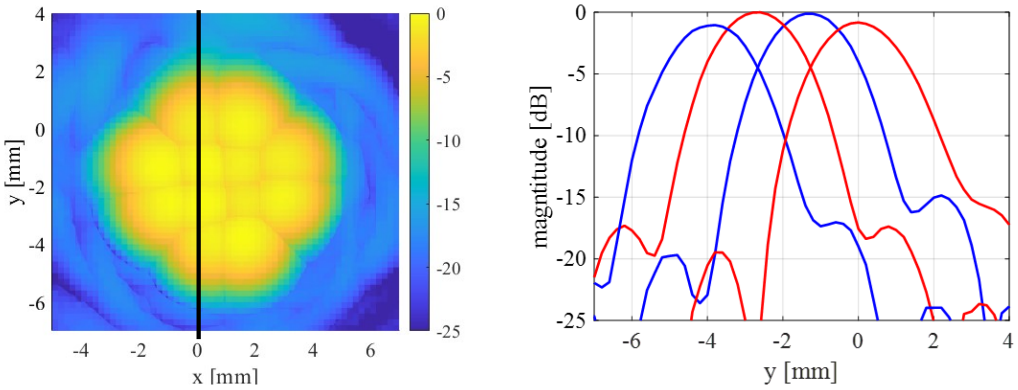

(c) 2D plot of combined patterns at 375 GHz.

(d) Cut of 4 radiation patterns at 375 GHz.

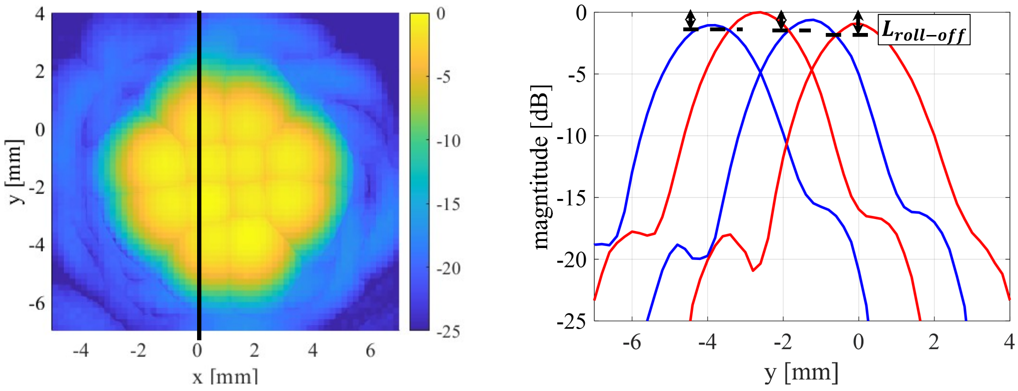

(e) 2D plot of combined patterns at 400 GHz.

(f) Cut of 4 radiation patterns at 400 GHz.

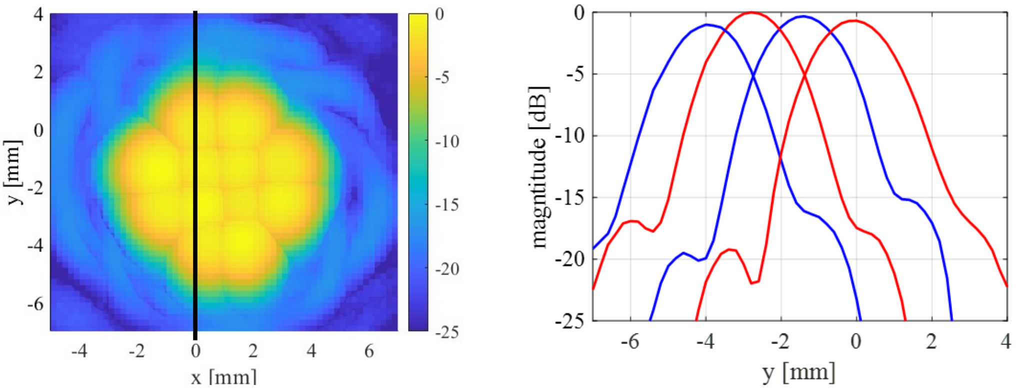

(g) 2D plot of combined patterns at 425 GHz. **(h)** Cut of 4 radiation patterns at 425 GHz.

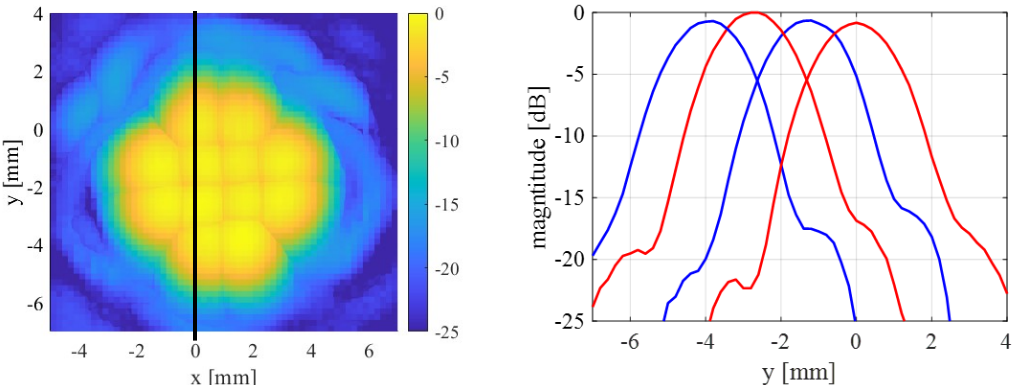

(i) 2D plot of combined patterns at 450 GHz. **(j)** Cut of 4 radiation patterns at 450 GHz.

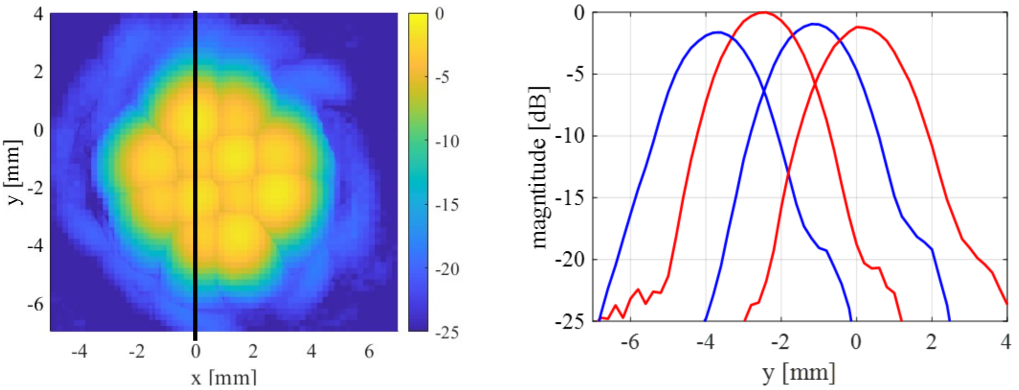

(k) 2D plot of combined patterns at 475 GHz. **(l)** Cut of 4 radiation patterns at 475 GHz.

Figure 4.4: Combined measured detector radiation patterns.

Figure 4.4 shows that the magnitude of the peaks of the detector radiation patterns is different for each detector. This is caused by a combined effect of scan loss, offset in system responsivity of each detector, misalignment of the QO setup and standing waves. This deviation in magnitude of the peaks can be compensated by equalizing the peaks to make more uniform images. For 400 GHz, the roll-off (see Figure 4.4f) was approximately -1.6 dB. This is 0.4 dB lower than the simulated beam overlap in Chapter 2 and can be ascribed to the same combination of effects that result in a deviation in radiation pattern peaks.

4.1.1 Directivity

To quantify the similarity between the measured patterns and simulated patterns, the focused antenna directivity as defined in Equation 2.10 has been calculated for both the measurements and simulations as a function of frequency. To evaluate the measured focused antenna directivity, Equation 2.10 is rewritten as:

$$D_{NF} = \frac{4\pi|\vec{S}(\vec{r}_{max})|r_{max}^2}{P_{rad}} = \frac{4\pi|\vec{E}_{det}^{im}(\vec{r}_{max})|^2 r_{max}^2}{\int\int_{S_{im}}|\vec{E}_{det}^{im}|^2 dS} \tag{4.1}$$

By noting that $\Delta V'_{out}(x_i, y_j) \propto |\vec{E}_{det}^{im}|^2$ and observing that $|\vec{E}_{det}^{im}|^2$ is both in the numerator and denominator, the focused antenna directivity can be calculated from the measurements by substituting $\Delta V'_{out}(x_i, y_j)$ for $|\vec{E}_{det}^{im}|^2$ in Equation 4.1. The simulated directivity is calculated with the simulated $|\vec{E}_{det}^{im}|^2$ obtained from PO methods in GRASP, following similar steps as in Chapter 2.

The dynamic range achieved in the measurement setup, around 25 dB, results in a range validity in the pattern measurement until 4mm, corresponding to the full main beam and first sidelobe. Thus, to give a fair comparison between the measurements and simulations, both are therefore truncated at 4 mm from the peak of the radiation pattern. Figure 4.5 shows a comparison between the measured and simulated directivity.

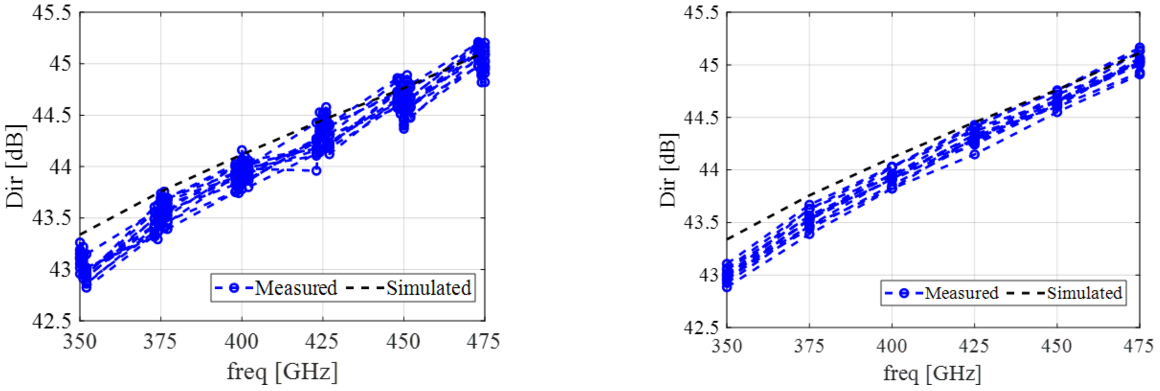

(a) Focused antenna directivity, all freq. **(b)** Focused antenna directivity, freq. averaged.

Figure 4.5: Simulated and measured focused antenna directivity at 25 GHz intervals with ± 1 GHz and ±2 GHz (a) and averaged over each ± 1 GHz and ±2 GHz (b).

The directivities were calculated for 350 GHz to 475 GHz with 25 GHz intervals, and at each interval ± 1 GHz and ±2 GHz (see Figure 4.5a). From these extra measurements the average directivity around each 25GHz interval was taken to reduce the effect of standing waves, resulting in the directivities displayed in Figure 4.5b. For these averaged measured directivities, the deviation w.r.t. the simulated directivities is at most 0.45 dB for all pixels at all frequencies, meaning there is excellent agreement between simulated and measured patterns.

4.1.2 Half-power beamwidth

$\Delta\rho_{HPBW}^{det}$ was calculated for all pixels and compared to the simulated values in Figure 4.6. $\Delta\rho_{HPBW}^{det}$ is calculated as an average over all cuts in the imaging plane. Figure 4.6 shows that $\Delta\rho_{HPBW}^{det}$ for the measured patterns is larger than the simulated virtual center pixel, as is expected since the directivity of the measured patterns was also slightly lower. It can be seen that both center pixels and edge pixels have approximately equal deviation in $\Delta\rho_{HPBW}^{det}$, which suggests the deviation is not due to the pixels being located further off-axis. This deviation is likely caused by the horn, as it is shown in Appendix B that there is a minor influence of the horn when the radiation patterns are measured, making the radiation patterns slightly wider. Figure 4.6 also shows the simulated $\Delta\rho^{det}_{HPBW}$ of the patterns when taking into account this effect of the horn, which is in good agreement with the measured $\Delta\rho^{det}_{HPBW}$.

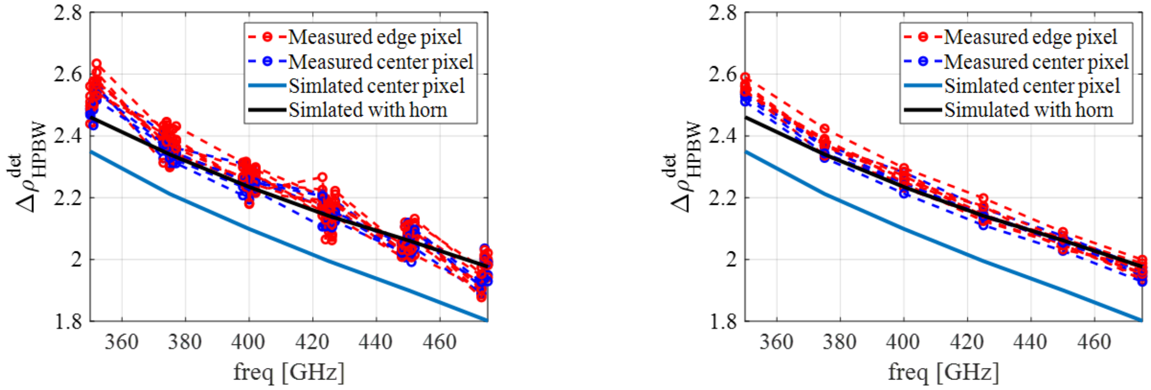

(a) HPBW for all frequencies.

(b) HPBW frequency averaged.

Figure 4.6: Simulated and measured HPBW at 25 GHz intervals with ± 1 GHz and ±2 GHz (a) and averaged over each ± 1 GHz and ±2 GHz (b).

4.2 Coupling

From the measured voltage response $\Delta V'_{out}$, the absolute power absorbed by each detector P_{det} can be calculated using Equation 3.2. From this P_{det} the overall coupling of the full QO setup, η_P^{QO} was extracted as defined in Equation 2.12. The definition of η_P^{QO} is illustrated in Figure 4.7. The measured η_P^{QO} will be compared to the simulated η_P^{QO}, which was calculated in Chapter 2 and shown in Table 2.2.

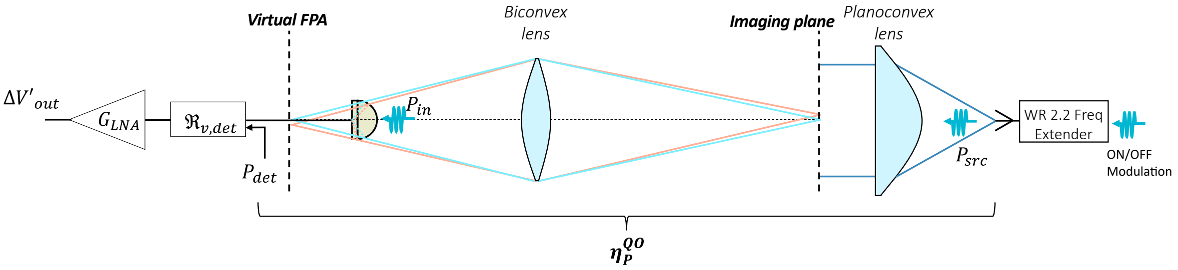

Figure 4.7: Overview of setup.

To determine measured η_P^{QO}, the power radiated by the source, P_{src}, needs to be accurately known. To determine this power, a VDI Erickson PM5 Power Meter was connected to the waveguide of the extender. After compensating for the losses and reflections in the waveguide taper of the PM5, P_{src} is obtained, which is shown in Figure 4.8.

Figure 4.8 shows that the power produced by the extender drops substantially for 325 GHz and 500 GHz. Therefore, the measurements are only performed in the 350GHz to 475GHz band.

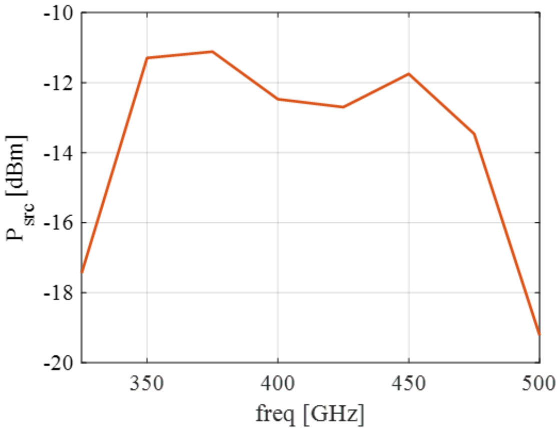

Figure 4.8: Measured power at the output of the extender.

Figure 4.9 shows the comparison between measured coupling and simulated coupling from Table 2.2 for all pixels. The coupling was first extracted for 350 GHz to 475 GHz with 25GHz intervals, and at each interval ±1 GHz and ±2 GHz, as shown in Figure 4.9a. Then the average coupling around each 25GHz interval was taken, resulting in the displayed measured coupling as shown in Figure 4.9b.

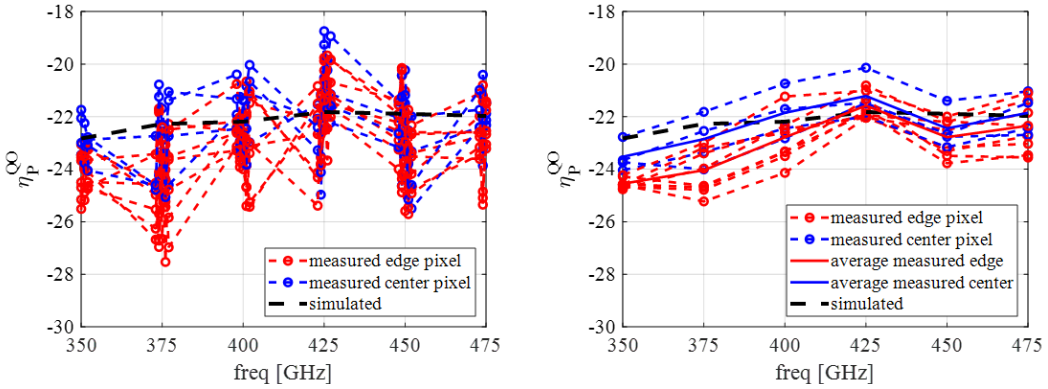

(a) All frequencies. **(b)** Frequencies averaged over ±1 GHz, ±2 GHz.

Figure 4.9: Measured versus simulated coupling.

In Figure 4.9b the average measured coupling of both the center and edge pixels is also shown. These averages reveal the effect of the off-axis position of the detectors on the coupling. It can be noted that the average measured coupling of the center pixels is slightly higher w.r.t. to edge pixels. The deviation between the averages varies between 1dB and 0.4dB. This deviation can be ascribed to the off-axis position which causes higher taper losses and scanning losses.

The simulation is performed with a virtual center pixel, which approximates the measured coupling of the center pixels better than the edge pixels. Thus, assessing how well the measurements match the simulations is performed best by comparing the measured average of the center pixels with the simulation. The measured average coupling of the center pixels varies between -0.7dB to +0.4dB w.r.t. the simulations. This is a very good agreement, and the remaining deviations in coupling can be ascribed to the remaining standing waves and deviations in responsivity of detectors.

4.3 Dynamic range

With the losses in the QO system characterized, the dynamic range remains to be found for all pixels. The dynamic range is important as it dictates the threshold of which signal levels can be displayed in the images before it is corrupted by noise. To find the dynamic range, first the peak value is measured while the source is on-off modulated. Then, the source is turned off and the average noise $\Delta V'_{out}|_{src,off}$ is calculated using 5 sampling points centered around the modulation frequency (see Figure 4.10). The dynamic range is then calculated as in Equation 4.2. Both the noise and $\Delta V'_{out}$ were measured with an integration time of 10 ms, which will also be used in Chapter 5 when images are taken. Following this method, the dynamic range is found for all pixels at all frequencies and shown in Figure 4.11.

$$DR = \frac{\Delta V'_{out}}{\Delta V'_{out}|_{src,off}} \tag{4.2}$$

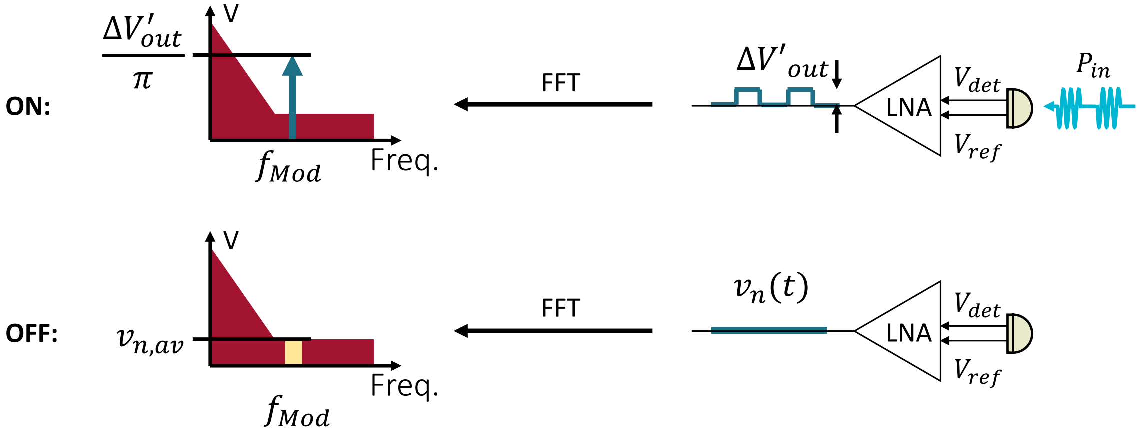

Figure 4.10: Illustration of measurement of the dynamic range.

The frequency averaged DR of each pixel is at least 20dB over the characterized bandwidth. The average DR of the center pixels is higher than the average DR of the edge pixels, which is expected since this difference was also present in the coupling measurements. The deviation in Q_P^{QO} between pixels will cause deviations in images. As will be explained in CH5, this deviation can be compensated for using a simple calibration step.

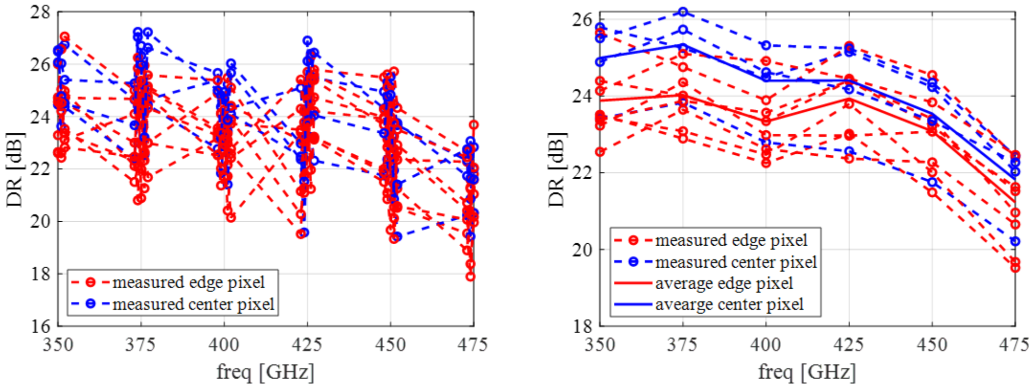

(**a**) Dynamic range for all frequencies.

(**b**) Dynamic range averaged over ±1 GHz, ±2 GHz

Figure 4.11: Dynamic range extracted from measured noise.

4.4 Standing wave effects

As could be seen in the measurements of the directivity, HPBW, coupling and DR, the ±1 GHz and ±2 GHz measurements showed significant fluctuations, indicating effects of standing waves. To explore the effect of these standing waves, the radiation patterns were measured at 398, 399, 400, 401 and 402 GHz. When measurements are performed at such small frequency intervals, the losses in the system should remain approximately constant. Any deviations in the measured radiation patterns can therefore be contributed to standing waves, thus giving a good estimate of how pronounced the standing wave effects are in this setup.

Figure 4.12 shows a cut of patterns of 4 pixels at 5 frequencies separated 1GHz intervals. It can be seen that the standing waves can influence measurements by up to 1.9dB. When measurements are performed at a single frequency, the measured power can thus vary by up to 1.9dB due to standing waves. This shows that averaging any measurements or images over multiple frequency points can greatly improve the quality of these measurements by averaging out these standing waves.

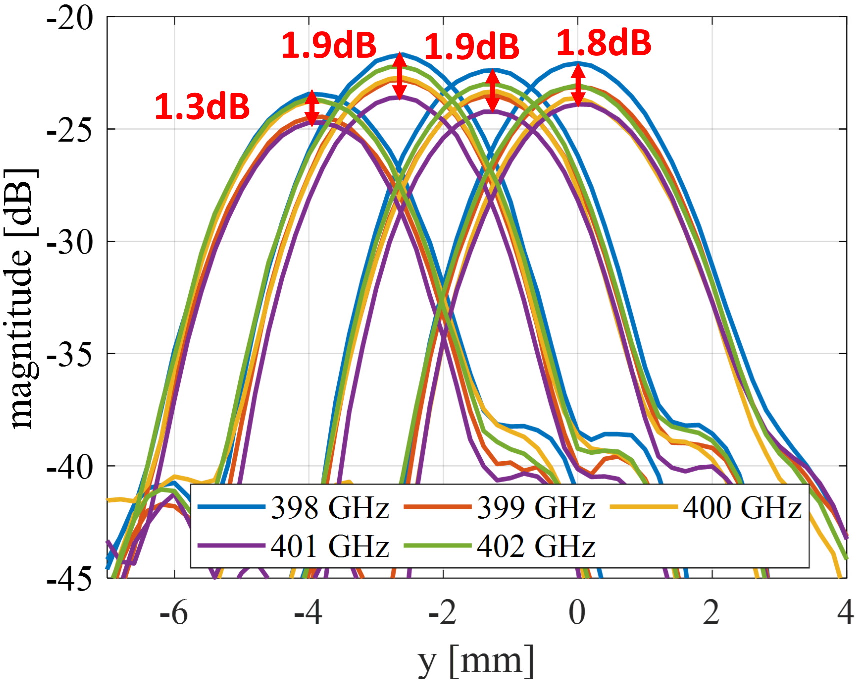

Figure 4.12: Effect of standing waves.

Chapter 5

Sample images using 12 pixel THz camera

With the radiation patterns and overall coupling of the full QO setup validated, images can be taken with the THz FPA camera. In this chapter, an efficient method for obtaining images with more pixels than the number of detector elements in the FPA is presented. After that, the images of two objects are shown and analysed for different frequencies, and the effect of a simple calibration is demonstrated. Finally, the images are compared to other state-of-the-art THz imagers.

5.1 Imaging method

With only 12 pixels available for readout, the array size is not sufficient to perform imaging in a practical scenario. To overcome this issue, the object that was desired to be imaged was moved in the imaging plane using a CNC machine. Consequently, some post-processing steps were required in order to construct a larger image from the individual 12-pixel images. All images were taken with an integration time of 10 ms.

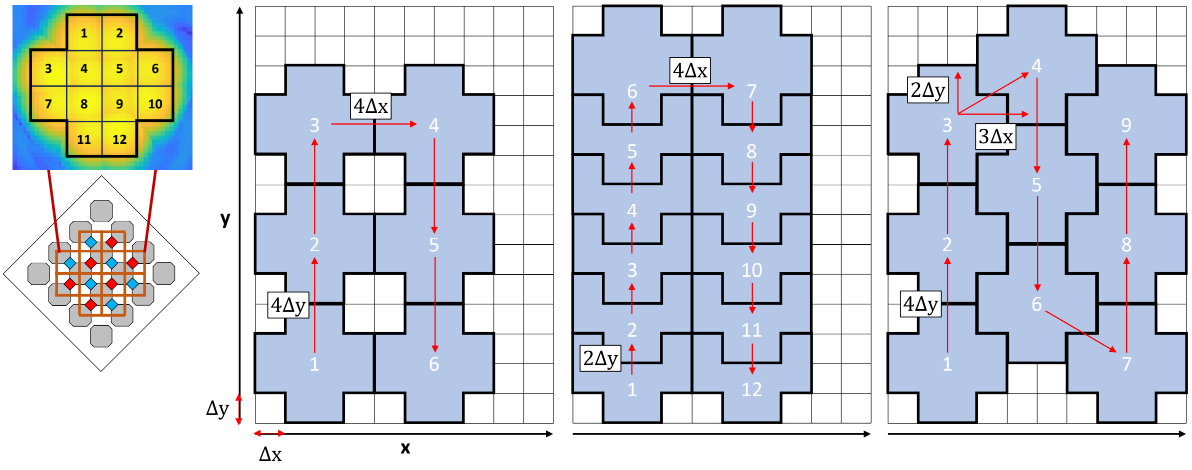

(a) (b) (c) (d)

Figure 5.1: Different methods for scanning the imaging plane, where the FPA imaging plane radiation patterns are resembled by a blue cross with a number in it (a). Scanning patterns in (b) and (c) result in poor performance, while (d), the brick-like pattern, results in optimal performance.

Figures 5.1b, 5.1c and 5.1d illustrate different methods for scanning the imaging plane, where the FPA radiation patterns in the imaging plane are resembled by a blue cross with a number in it, as is visualized in 5.1a. In this illustration, the imaging plane is divided into an array of 14×10 pixels each with a size of $\Delta x \times \Delta y$, where Δx and Δy are the beam separation in the x- and y- dimensions, respectively. One measurement of all 12 pixels will be called a scan. As shown in Figure 5.1b, moving the sample by steps of $4\Delta x$ and $4\Delta y$ before taking the next scan results in gaps in the image. One could resolve this by using a step size of $4\Delta x$ and $2\Delta y$ (see Figure 5.1c) as this leaves no gaps in the image, but the number of pixels that is effectively used this way is reduced to 8, and thus increases imaging time. Instead, a step size of $3\Delta x$ and $2\Delta y$ with an offset of $2\Delta y$ in every other x-columns is used, creating the brick-like pattern (see Figure 5.1d). Using this method, no gaps are present in the image and all pixels are used. A down-side of this method is that there are some gaps around the edges of the resulting image.

To implement the imaging procedure in the most simple manner, a constant separation Δx Δy is assumed between the beams of the pixels. This separation was determined using the multi-beam radiation pattern measurements from Section 4.1.2, as is illustrated in Figure 5.2. By taking the average separation over all multi-beam radiation pattern measurements, it was found that $\Delta y_1 \approx \Delta y_2 \approx \Delta x_1 \approx \Delta x_2 \approx 1.33mm$.

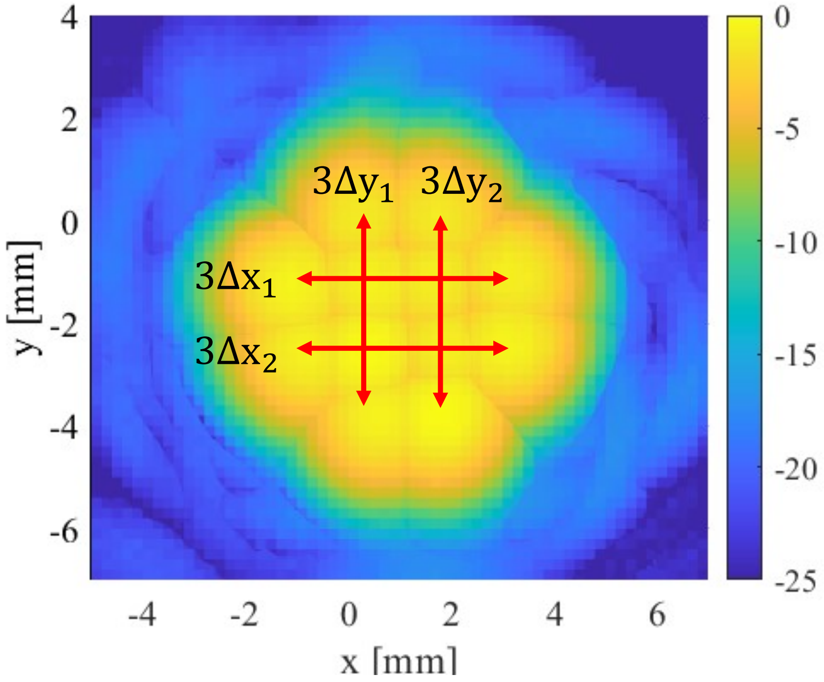

Figure 5.2: dx and dy characterization.

The average time to take one scan (one image of 12 pixels), T_{scan}, is 3.2 seconds for 1 frequency point. The area of one scan, A_{scan}, is approximately $21mm^2$. The time to take an image of an object at one frequency, T_{sample}, is then calculated as:

$$T_{sample} = T_{scan}\frac{A_{sample}}{A_{scan}} \tag{5.1}$$

Where A_{sample} is the area of the object that is being imaged. This large time per scan is mainly attributed to the switches, which have to switch between 4 ports for one scan. Another cause is the time it takes the CNC to move the object in the imaging plane.

5.2 Sample images

Two objects were imaged with the THz camera for all characterized frequencies. The first object was a thin metal sheet with slots. Since the used material is metal, the images become almost binary, as no radiation from the source can be coupled by the detector when the metal is at the location of the respective detector radiation pattern in the imaging plane. The coupling for different circular slots is simulated using the simulated fields of the horn and detector radiation pattern in the imaging plane and compared to the measured coupling for the respective slot. The second object that was imaged, was a green leaf. Within the leaf a part of the radiation was absorbed, which gave information about the structure of the leaf.

5.2.1 Metal sheet with slots

Figure 5.3 shows a picture of a thin sheet of metal that was fabricated to evaluate the imaging capacity of the THz camera. The metal sheet has a thickness of 0.1 mm, well below the wavelength for the center frequency of 400 GHz (e.g. 0.75 mm), reducing the risk of diffraction effects. The diameter of the circles and width of the slits ranges from 0.9 mm to 9 mm, which corresponds to $1.2\lambda_0$ to $12\lambda_0$ or $0.4\Delta\rho_{HPBW}^{det}$ to $4\Delta\rho_{HPBW}^{det}$ for the center frequency of 400 GHz. The metal sheet is put in an envelope for support, but also to demonstrate the ability of radiation at these frequencies to penetrate packaging materials.

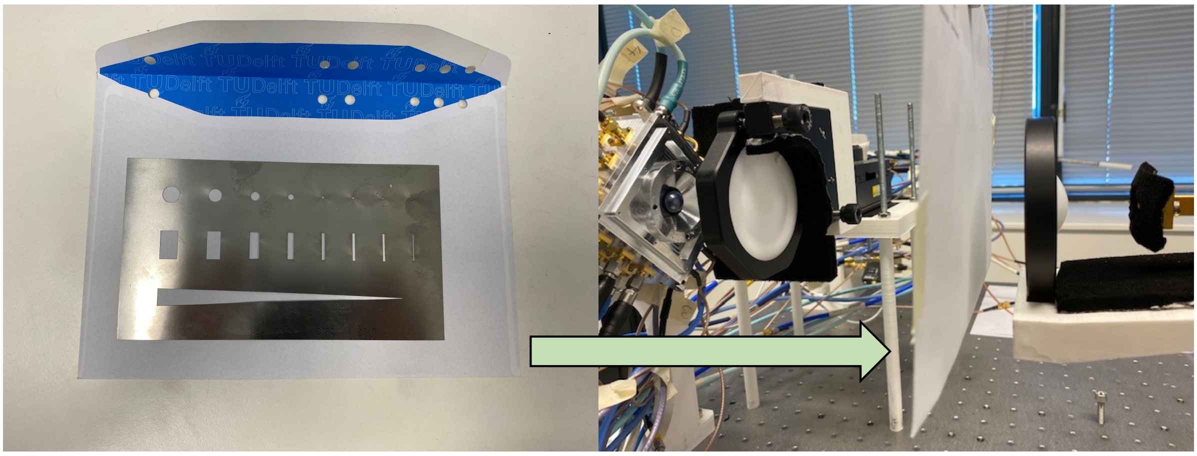

Figure 5.3: Fabricated metal sheet with slots for imaging.

Figure 5.4a shows the raw image of the metal sheet with slots, Figure 5.4b shows the image where the voltage response of the detectors are equalized when no object is in the imaging plane, and Figure 5.4c shows the image in which both the voltage responses are equalized and averaging is performed over a narrow frequency band. Equalizing the voltage responses makes the apertures more uniform, but the increase in image quality is minor. As expected, the frequency averaging increases uniformity among pixels located on a slot, by averaging out of the standing waves. Figure 5.4c also compares the THz camera image to the (designed) physical dimensions of the slots in the metal sheet (shown in red), which shows excellent agreement and therefore confirms a correct image construction.

To quantitatively asses the realized imaging performance, the coupling of the circular slots in Figure 5.4c is compared to simulations. Using Equation 2.9, the coupling between the detector and source can be calculated from the imaging plane fields of the detector and source, which were obtained through a PO method in GRASP. To this end, $\vec{E}_{det}^{im}$ and $\vec{E}_{src}^{im}$ are integrated over the full imaging plane in the denominator of Equation 2.9, identical to Chapter 2. In the numerator, the reaction integral is evaluated until $\rho = \varnothing_0/2$, where $\varnothing_0$ is the diameter of the slot. $\vec{E}_{det}^{im}$ and $\vec{E}_{src}^{im}$ are set to 0 for $\rho > \varnothing_0/2$ to include the effect of the metal sheet, as shown in Figure 5.5. It is important to note that this is a first-order approximation, as diffraction is not taken into account. Especially for the smaller

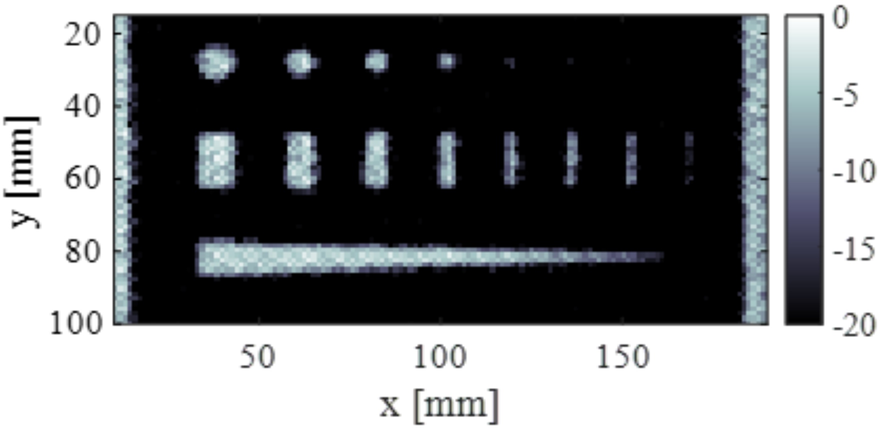

(a) No compensation and no frequency averaging.

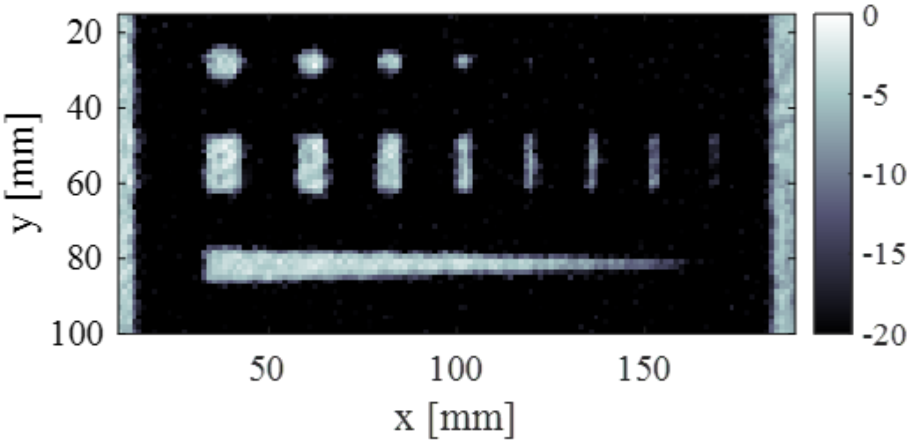

(b) With compensation and no frequency averaging.

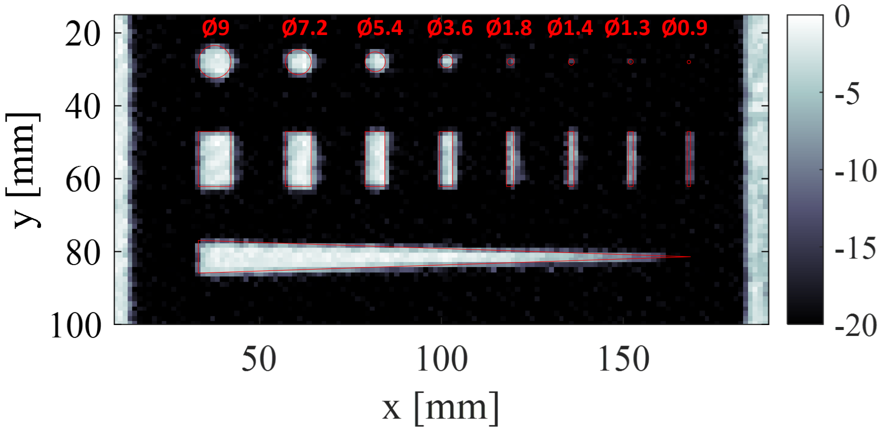

(c) Metal sheet at 400 GHz, with compensation and with frequency averaging, compared to designed slot dimensions.

Figure 5.4: Images of the metal sheet with slots taken with THz camera.

apertures the diffraction might have a more pronounced effect.
Besides the size of the slots, the coupling is also affected by the alignment of a slot to a pixel. This effect is explained schematically in Figure 5.6. In the best case scenario, the pattern of a pixel coin-

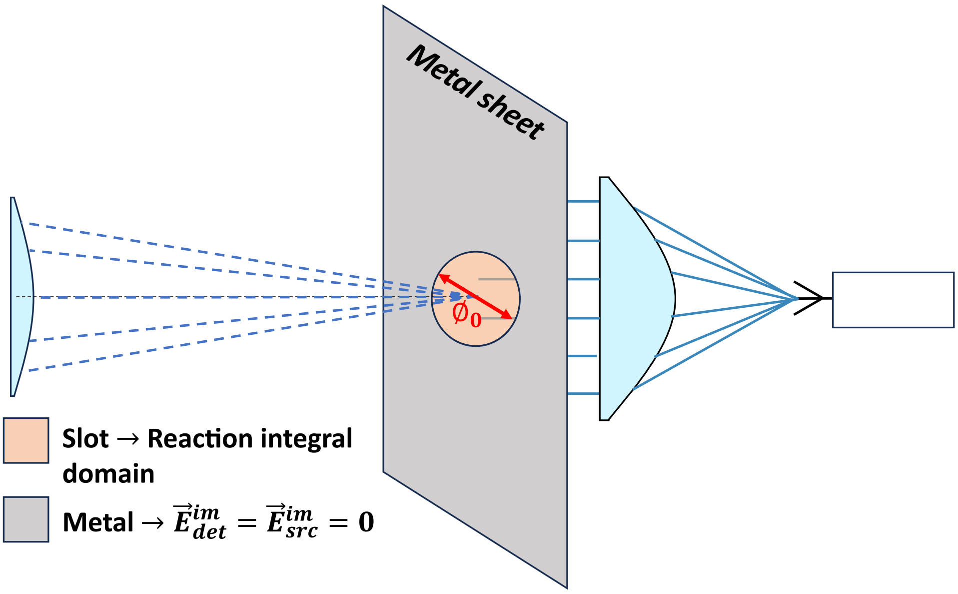

Figure 5.5: Method for calculating the coupling using a reaction integral in the imaging plane.

cides with the center of the circular slot in the metal sheet, which results in maximum coupling. In the worst case scenario, the center of the circular slot is located furthest away from the peak of any pixel pattern, which occurs when the circular slot is at the cross-over of 4 pixels, which is the least covered point in the field-of-view.

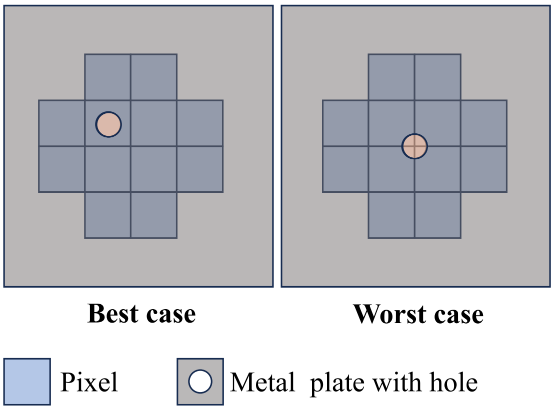

Figure 5.6: Explanation of the two scenarios that give maximum (best case) and minimum (worst case) coupling.

By truncating the fields in the numerator for different $\rho > \varnothing_0/2$, the coupling for is found as a function of the circle diameter, $\varnothing_0$ and shown in Figure 5.7. On the y-axis the coupling is normalized to the coupling for a diameter of $\varnothing_0 = 9mm$, as will also be done when the comparison is made with the measurements.

Figure 5.8 shows a cut of the image shown in Figure 5.4c, taken along the centers of the circular slots, and normalized to the coupling of the 9 mm slot. Note that there is a decreased DR in this image w.r.t (4.11), caused by the losses of an envelope in which the metal sheet was placed, approximately 2 dB. The simulated and measured normalized coupling is compared in Table 5.1 and visually represented in Figure 5.8.

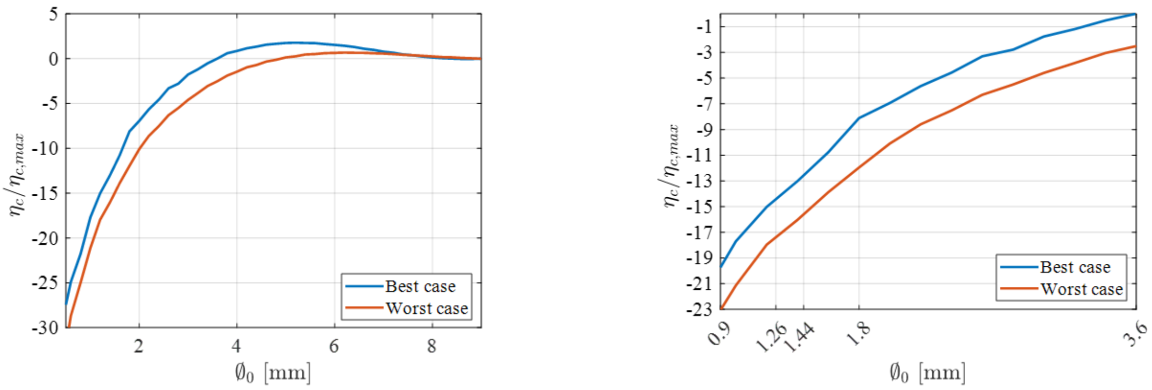

(a) Zoom-out.

(b) Zoom-in.

Figure 5.7: simulated coupling as a function of slot size.

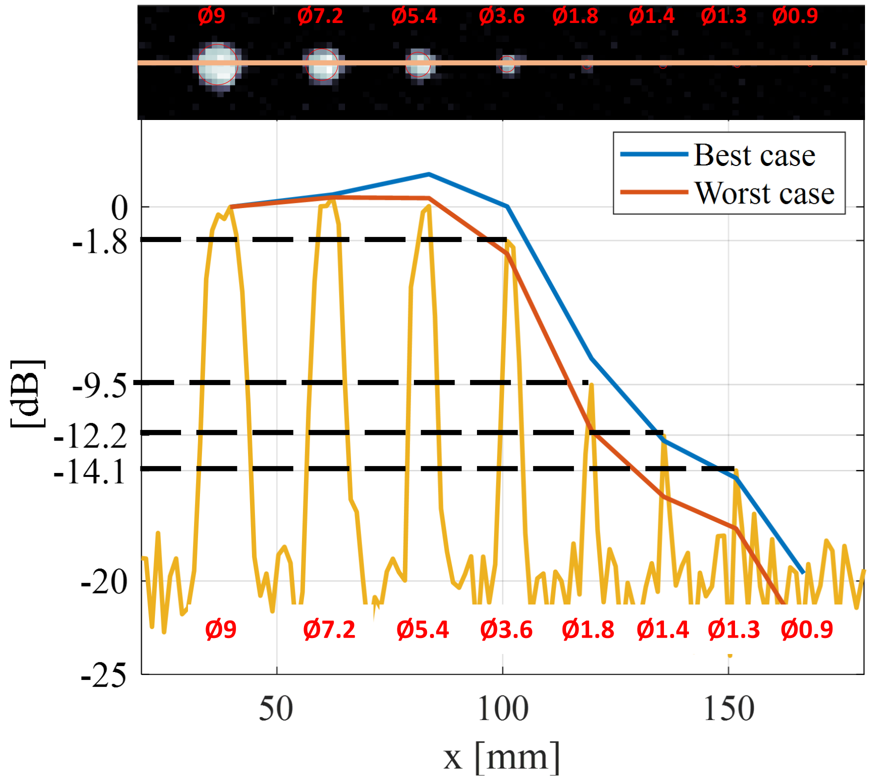

Figure 5.8: Coupling for a cut along the circular slots of the image shown in Figure 5.4c, indicating the peak values for the different apertures.

Table 5.1: Measured versus simulated coupling for circular slots in imaging plane.

$\varnothing_0$	**Simulated worst case**	**Simulated best case**	**Measured**
9 mm	0 dB	0 dB	0 dB
7.2 mm	0.51 dB	0.66 dB	0.53 dB
5.4 mm	0.47 dB	1.75 dB	0.04 dB
3.6 mm	-2.51 dB	0.02 dB	-1.83 dB
1.8 mm	-11.96 dB	-8.11 dB	-9.52 dB
1.44 mm	-15.5 dB	-12.5 dB	-12.23 dB
1.26 mm	-17.2 dB	-14.5 dB	-14.09 dB
0.9 mm	-23 dB	-19.6 dB	/

Table 5.1 shows that in general there is good agreement between the simulation and measurement. The 0.9 mm aperture is not measured as it can not be distinguished from the noise. For $\varnothing_0 = [5.4, 1.44, 1.26]$ there are minor deviations to the maxima and minima of at most 0.4dB, which can be caused by standing waves, diffraction or the normalization or inaccuracies due to the inaccuracies in the simulated first-order approximation.

5.2.2 Leaf

The second imaged object is a green leaf. To support the leaf, it was taped inside an envelope. Figure 5.9 shows images of a leaf using the imaging setup at different frequencies. Each image is compared to an image taken by a regular camera of the same leaf. Each image is normalized to the maximum received level and with a DR of 25 dB.

All middle figures show the raw image as captured by the camera. A noisy, but periodic pattern can be recognized in the middle figures, which arises from the different responsivities of the pixels. Since this error is deterministic of nature, it can be easily compensated for by equalizing the pixel responses. After applying this compensation, the rightmost figures are obtained.

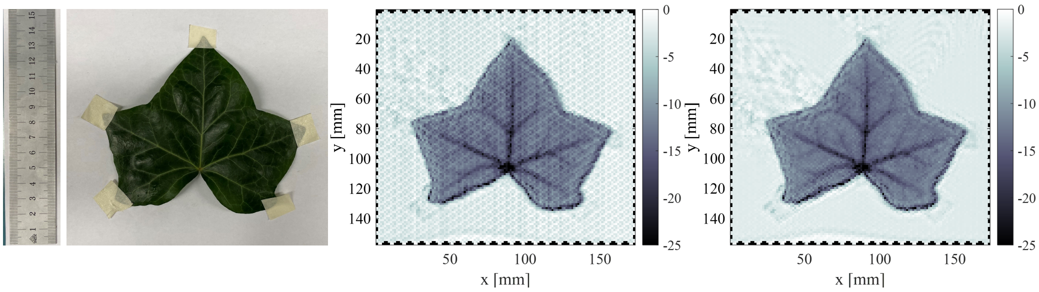

(a) leaf, 350 GHz.

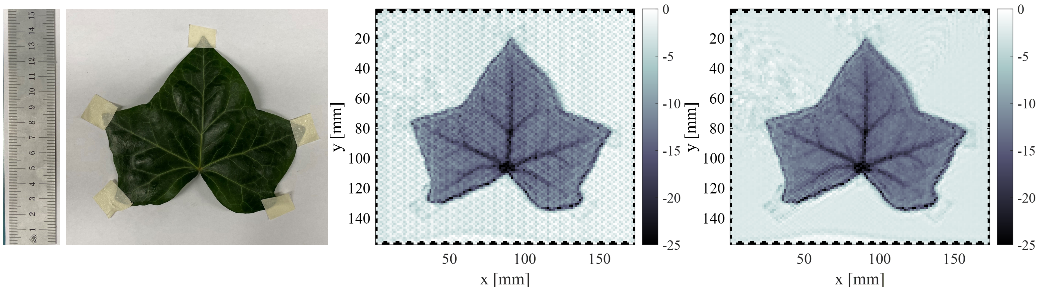

(b) leaf, 375 GHz.

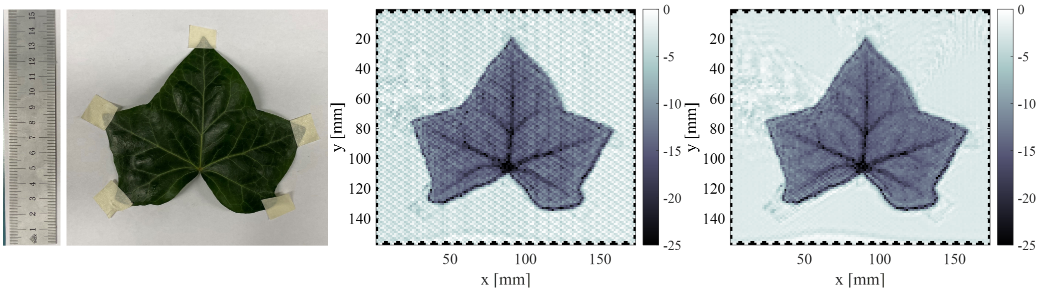

(c) leaf, 400 GHz.

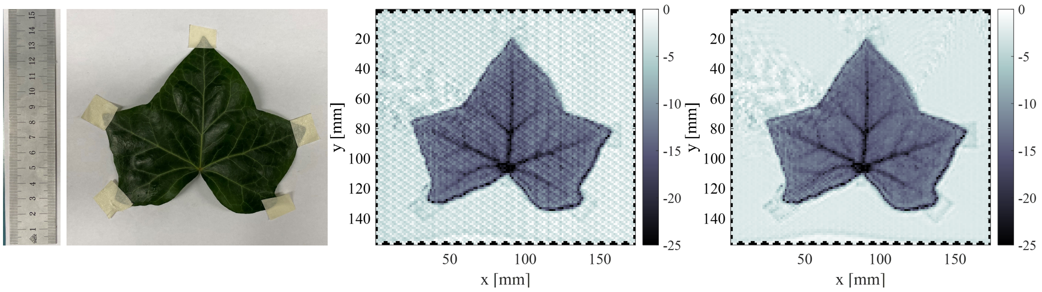

(**d**) leaf, 425 GHz.

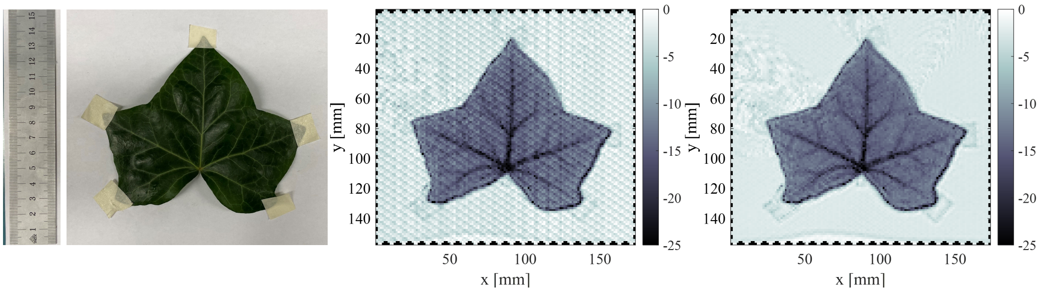

(**e**) leaf, 450 GHz.

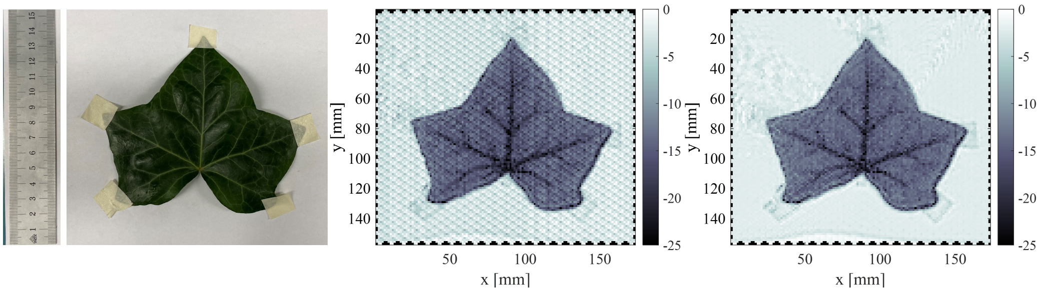

(**f**) leaf, 475 GHz.

Figure 5.9: Images of a leaf taken with a regular camera (left), raw image from THz camera (center), compensated THz camera (right).

The main veins of the leaf appear as very dark on the images, indicating low transmission. The other areas of the leaf present around -10 dB of attenuation. The image implies that the water content in the main veins is higher, which is most likely the result of their thickness. If one looks carefully, the tape used to fix the leaf can also be distinguished in the images.

When comparing images taken at different frequencies, it stands out that the absorption for high frequencies is larger than for small frequencies. This is caused by the water absorption increasing with frequency [29]. For higher frequencies, transitions seem sharper, like the edge of the leave. This is caused by the smaller HPBW of the detector in the imaging plane and thus higher isolation of each pixel.

Figure 5.10 compares the images from Figure 5.9c to an image that has been compensated and averaged over a narrow frequency band. To obtain the averaged image, 5 images were taken around the frequencies of interest with, ±1 GHz. after compensating the entire image using the same method as before, at each location (x_i, y_i) the average over these frequencies was taken. This way, the impact of standing waves is reduced and therefore an image with higher quality is obtained, as can be seen in Figure 5.10c.

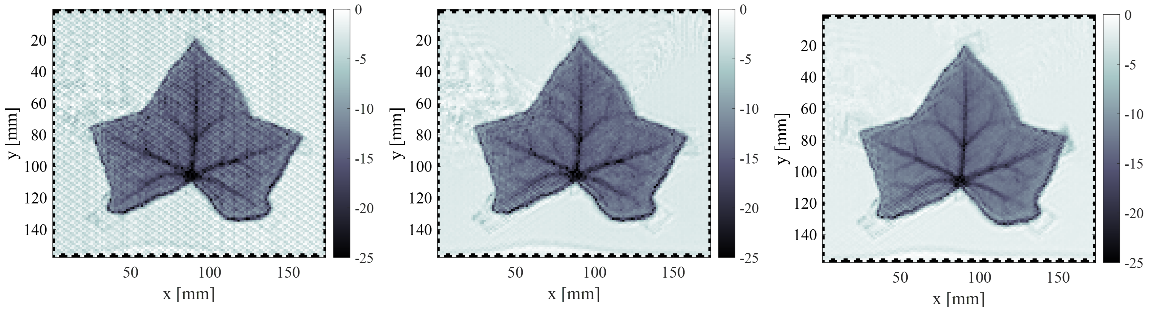

(a) (b) (c)

Figure 5.10: Image of leaf at 400 GHz without compensation (a), with compensation (b) and with compensation and frequency averaging (c).

5.2.3 Image quality comparison with different samplings

To illustrate the effect of the sampling on the quality of the image, the same image has been measured with a 2× higher sampling rate $d_{oversample} = d_f/2$ than the THz camera presented in this work, which gave a virtual periodicity of $d_{oversample} = 0.35F_{\#}\lambda_d$ (see table 1.1). This higher sampling rate was achieved by creating an image with a single pixel and moving the object in the imaging plane with $\Delta x/2$ and $\Delta y/2$. The ratio between the periodicity of a state-of-the-art THz imager, d_{comp}, and the over-sampled image setup is then $N = d_{comp}/d_{oversample}$, rounded to the nearest integer. The virtual image was then obtained by selecting every N^{th} pixel in both x and y and discarding intermediate pixels.

Figure 5.11 shows the comparison between the virtual image with 2 × higher sampling and the image taken with the array. Since the array performs near the diffraction limit, it was expected that the resolution of the image would not increase with a factor 2 when the sampling was 2 × higher. Indeed, the level of details visible in both images is very similar.

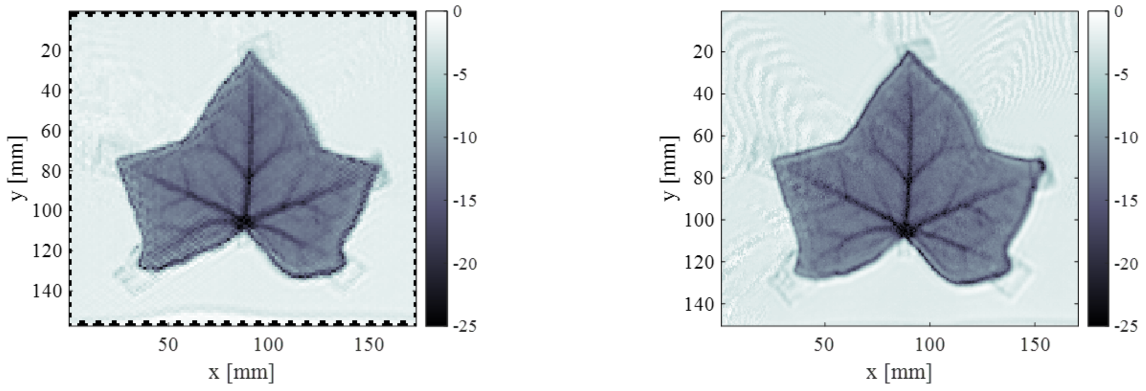

(a) Leaf image from array, $d_f = 0.7F_{\#}\lambda$.

(b) $d_f = 0.35F_{\#}\lambda_d$.

Figure 5.11: Comparison of image obtained with with THz camera and over-sampled virtual image.

To verify that down-sampling the over-sampled figure gave an accurate representation of the image directly obtained with the FPA, Figure 5.12 shows the comparison between the image of the array and the virtual image down-sampled with N = 2. The images are indeed in very good agreement.

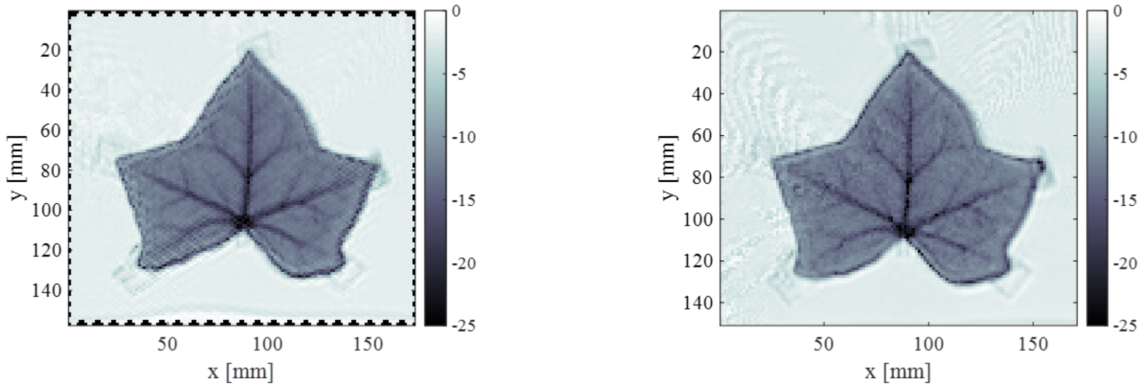

(a) Leaf image from array, $d_f = 0.7F_{\#}\lambda$. **(b)** $d_f = 0.7F_{\#}\lambda_d$.

Figure 5.12: Comparison of image obtained with with THz camera and virtual image with $d_f = 0.7F_{\#}\lambda_d$.

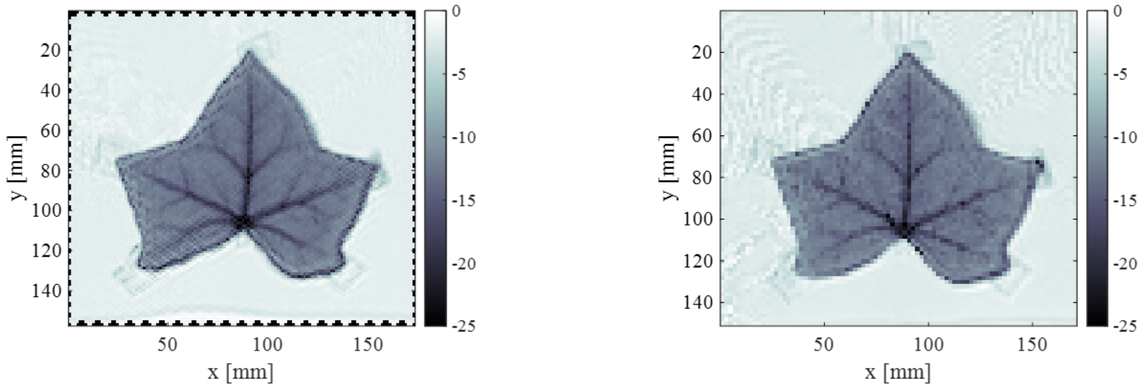

(a) Leaf image from array, $d_f = 0.7F_{\#}\lambda$. **(b)** $d_f = 1.05F_{\#}\lambda_d$.

Figure 5.13: Comparison of image obtained with with THz camera and virtual image with $d_f = 1.05F_{\#}\lambda_d$.

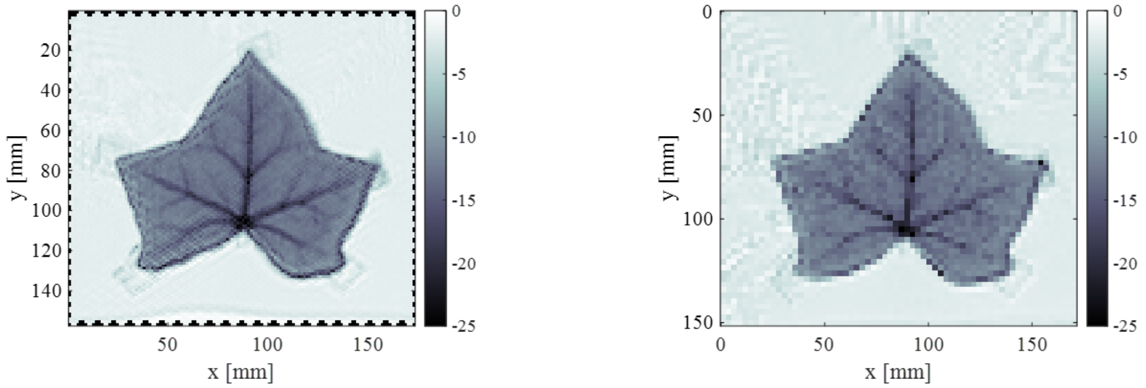

(a) Leaf image from array, $d_f = 0.7F_{\#}\lambda$. **(b)** $d_f = 1.4F_{\#}\lambda_d$.

Figure 5.14: Comparison of image obtained with with THz camera and virtual image with $d_f = 1.4F_{\#}\lambda_d$.

Table 1.1 shows an overview of the current state-of-the-art THz imagers, each with their periodicity. The periodicity of an array composed of wire-ring antennas presented in [13] and [14] resulted in a periodicity of $d_f = 1.2F_{\#}\lambda_d^{(a)}$, which should give an image quality somewhere in between Figure 5.13b and 5.14b. The array presented in [15] would give $d_f = 1.4F_{\#}\lambda_d^{(a)}$ and is therefore resembled

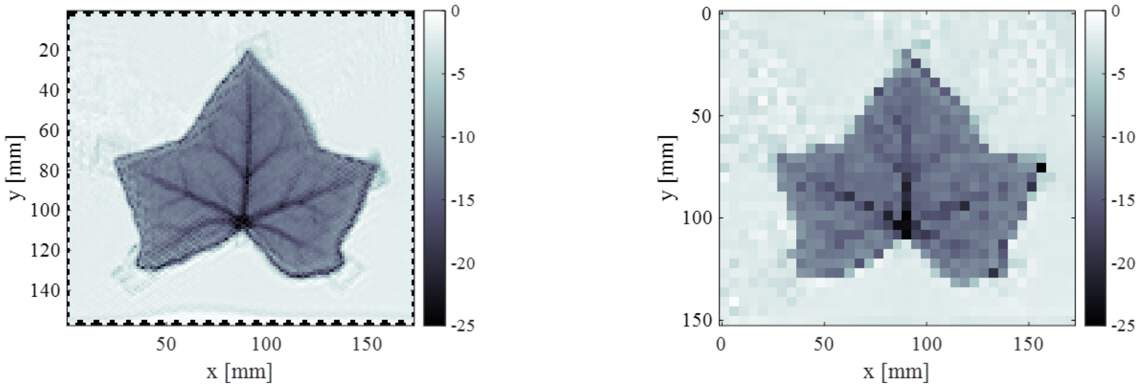

(a) Leaf image from array, $d_f = 0.7F_\#\lambda$.

(b) $d_f = 2.45F_\#\lambda_d$.

Figure 5.15: Comparison of image obtained with with THz camera and virtual image with $d_f = 2.45F_\#\lambda_d$.

by Figure 5.14b. Finally, Figure 5.15 makes a comparison between the image of the array and the image of an array composed of double slot elements presented in [12] with $d_f = 2.5F_\#\lambda_d$.

The presented comparison demonstrates that the images from the THz imager in this work show significantly higher quality than other state-of-the-art THz imagers. Considering that the image captured with a 2× lower periodicity presented in 5.11b did result in substantially higher level of details than the image captured with the FPA shown 5.11a confirms that the obtained images with the FPA are in fact (near) diffraction limited.

Chapter 6

Conclusion and future work

6.1 Summary and conclusions

This work was dedicated to the realization of (near) diffraction-limited images using the silicon-integrated THz camera developed in [11]. The main challenge was to design a QO setup that does not degrade the scanning capabilities of the QO setup and simultaneously maximizes the uniform coupling between the THz source and each of the detectors of the FPA. As a trade-off, a QO setup was designed in which the two-way-beam-pattern of the detector in the imaging plane deviated at most 0.5 dB from the original beam pattern, and a coupling of -15 dB was achieved for the dual-polarized scenario.

After the QO setup was designed, an overview and description of the working principles of the overall imaging implementation was presented, including the coherent source, the detector architecture, the readout and the implementation of the 12 pixel FPA. The hyperbolic lenses were fabricated and a combination of 3D-printed parts were assembled with lens holders and 3-axis stages to allow accurate alignment. The process for aligning the QO setup was thoroughly described with an overall accumulated worst-case accuracy of 0.7 mm.

Following the implementation and alignment of the QO setup, the system was characterized. First, the radiation patterns in the imaging plane were obtained. The similarity between the simulated and measured patterns was expressed via the near field directivity and showed excellent agreement, with a deviation of at most 0.45 dB over the characterized bandwidth. Subsequently, the coupling and dynamic range of all pixels of the full QO setup were measured. The overall coupling of the QO setup was between -25 dB and -20 dB over the characterized bandwidth, with a maximum deviation between measured and simulated coupling of 0.7 dB, which is also a very good result. The dynamic range among the pixels over 350 GHz - 475 GHz was between 20 dB and 26 dB.

Next, an efficient method for sampling the field-of-view with the 12 pixels of the FPA was presented. The images of a slotted metal plate and a leaf were presented. Images for different frequencies were presented and the effect of frequency averaging and compensation for detector responsivity on the image quality was analyzed. The applied compensation resulted in the removal of the noisy, but periodic pattern, and frequency averaging revealed finer details in the picture by removing the standing waves. Consequently, a comparison of the imaging quality was performed with images taken using the sampling periodicity of other state-of-the-art images. It was concluded that a substantial improvement of image quality could be seen with respect to the other state-of-the-art imagers. Finally, it was noted that oversampling the array with a 2x lower periodicity did not result in images with a substantially higher level of details, confirming that the obtained resolution is indeed (near) diffraction-limited.

6.2 Future work

This work demonstrated that the imaging system is capable of creating high resolution images. In order to make the imaging setup more appealing for commercial use, several suggestions for improvement are presented here.

For the imaging system to be compelling in commercial fields, the imaging time should be decreased. In the current design, a single 12 pixel image took 3.2s to complete. As explained in Chapter 3, this was largely caused by the switching mechanism. A study could be performed towards an integrated switching solution. Another cause for the large image time was the movement of the CNC. This can be solved by scaling the FPA, increasing the field-of-view so that the object in the imaging plane can be moved in larger steps or would not need to be moved within the imaging plane at all. A new QO setup would need to be designed in that scenario, as more pixels would need to be illuminated. Achieving uniform illumination could prove challenging in this situation, as a larger area in the imaging plane needs to be illuminated, therefore also decreasing the coupling between the source and each individual detector.

The used THz camera was designed as a broadband solution, but in this work only single frequency measurements were performed. A study towards imaging with a broadband source could show how the detector would perform when imaging a black body, as black bodies also radiate broadband signals.

The imaging setup has shown that it is possible to image through packaging material, in this case an envelope. A case study towards more user cases could be performed, like scanning mail for prohibited items.

Finally, an interesting case study would be to place the source at the location of the detector, allowing for stand-off detection. Instead of illuminating an object, reflections from the measured object would be measured.

Bibliography

[1] P. Siegel, “Terahertz technology,” *IEEE Transactions on Microwave Theory and Techniques*, vol. 50, no. 3, pp. 910–928, 2002.

[2] D. Jasteh, E. G. Hoare, M. Cherniakov, and M. Gashinova, “Experimental low-terahertz radar image analysis for automotive terrain sensing,” *IEEE Geoscience and Remote Sensing Letters*, vol. 13, no. 4, pp. 490–494, 2016.

[3] T. S. Rappaport, Y. Xing, O. Kanhere, S. Ju, A. Madanayake, S. Mandal, A. Alkhateeb, and G. C. Trichopoulos, “Wireless communications and applications above 100 ghz: Opportunities and challenges for 6g and beyond,” *IEEE Access*, vol. 7, pp. 78729–78757, 2019.

[4] D. Woolard, R. Brown, M. Pepper, and M. Kemp, “Terahertz frequency sensing and imaging: A time of reckoning future applications?,” *Proceedings of the IEEE*, vol. 93, no. 10, pp. 1722–1743, 2005.

[5] P. Hillger, J. Grzyb, R. Jain, and U. R. Pfeiffer, “Terahertz imaging and sensing applications with silicon-based technologies,” *IEEE Transactions on Terahertz Science and Technology*, vol. 9, no. 1, pp. 1–19, 2019.

[6] P. Richards, “Bolometers for infrared and millimeter waves,” *Journal of Applied Physics 76*, vol. 1, 1994.

[7] S. van Berkel, O. Yurduseven, A. Freni, A. Neto, and N. Llombart, “Thz imaging using uncooled wideband direct detection focal plane arrays,” *IEEE Transactions on Terahertz Science and Technology*, vol. 7, no. 5, pp. 481–492, 2017.

[8] J. F. Johansson, *Millimeter-wave imaging theory and experiments.* 1986.

[9] A. Timofeev, J. Luomahaara, L. Grönberg, A. Mäyrä, H. Sipola, M. Aikio, M. Metso, V. Vesterinen, K. Tappura, J. Ala-Laurinaho, A. Luukanen, and J. Hassel, “Optical and electrical characterization of a large kinetic inductance bolometer focal plane array,” *IEEE Transactions on Terahertz Science and Technology*, vol. 7, no. 2, pp. 218–224, 2017.

[10] R. Zatta, R. Jain, J. Grzyb, and U. R. Pfeiffer, “Resolution limits of hyper-hemispherical silicon lens-integrated thz cameras employing geometrical multiframe super-resolution imaging,” *IEEE Transactions on Terahertz Science and Technology*, vol. 11, no. 3, pp. 277–286, 2021.

[11] M. Hoogelander, S. v. Berkel, S. Malotaux, M. Alonso-delPino, D. Cavallo, M. Spirito, and N. Llombart, “Chessboard focal plane array for a cmos-integrated terahertz camera,” *IEEE Transactions on Terahertz Science and Technology*, pp. 1–13, 2023.

[12] S. v. Berkel, E. S. Malotaux, C. d. Martino, M. Spirito, D. Cavallo, A. Neto, and N. Llombart, “Wideband modeling of cmos schottky barrier diode detectors for thz radiometry,” *IEEE Transactions on Terahertz Science and Technology*, vol. 11, no. 5, pp. 495–507, 2021.

[13] M. Andree, J. Grzyb, R. Jain, B. Heinemann, and U. R. Pfeiffer, “A broadband dual-polarized terahertz direct detector in a 0.13-μm sige hbt technology,” in *2019 IEEE MTT-S International Microwave Symposium (IMS)*, pp. 500–503, 2019.

[14] J. Grzyb, M. Andree, R. Jain, B. Heinemann, and U. R. Pfeiffer, "A lens-coupled on-chip antenna for dual-polarization sige hbt thz direct detector," *IEEE Antennas and Wireless Propagation Letters*, vol. 18, no. 11, pp. 2404–2408, 2019.

[15] R. Al Hadi, H. Sherry, J. Grzyb, Y. Zhao, W. Forster, H. M. Keller, A. Cathelin, A. Kaiser, and U. R. Pfeiffer, "A 1 k-pixel video camera for 0.7–1.1 terahertz imaging applications in 65-nm cmos," *IEEE Journal of Solid-State Circuits*, vol. 47, no. 12, pp. 2999–3012, 2012.

[16] R. Han, Y. Zhang, Y. Kim, D. Y. Kim, H. Shichijo, E. Afshari, and K. K. O, "Active terahertz imaging using schottky diodes in cmos: Array and 860-ghz pixel," *IEEE Journal of Solid-State Circuits*, vol. 48, no. 10, pp. 2296–2308, 2013.

[17] K. Sengupta, D. Seo, L. Yang, and A. Hajimiri, "Silicon integrated 280 ghz imaging chipset with 4× 4 sige receiver array and cmos source," *IEEE Transactions on Terahertz Science and Technology*, vol. 5, no. 3, pp. 427–437, 2015.

[18] A. Lisauskas, W. Spiegel, S. Boubanga-Tombet, A. EL Fatimy, D. Coquillat, F. Teppe, N. Dyakonova, W. Knap, and H. Roskos, "Terahertz imaging with gaas field-effect transistors," *Electronics Letters*, vol. 44, pp. 408 – 409, 02 2008.

[19] M. Hoogelander, S. Van Berkel, S. Malotaux, M. Alonso-delPino, M. Spirito, A. Neto, D. Cavallo, and N. Llombart, "Diffraction-limited imaging demonstration using a silicon integrated array at terahertz frequencies," in *2022 47th International Conference on Infrared, Millimeter and Terahertz Waves (IRMMW-THz)*, pp. 1–2, 2022.

[20] G. Rebeiz, "Millimeter-wave and terahertz integrated circuit antennas," *Proceedings of the IEEE*, vol. 80, no. 11, pp. 1748–1770, 1992.

[21] A. N. E. Gandini, N. Llombart, "Focal plane array size reduction for terahertz transceivers in integrated technology," in *European conference on Antennas and Propagation (EuCAP)*, (Lisbon, Portugal), 2015.

[22] H. Zhang, S. O. Dabironezare, G. Carluccio, A. Neto, and N. Llombart, "A fourier optics tool to derive the plane wave spectrum of quasi-optical systems [em programmer's notebook]," *IEEE Antennas and Propagation Magazine*, vol. 63, no. 1, pp. 103–116, 2021.

[23] M. Hoogelander, S. van Berkel, S. Malotaux, M. Alonso, M. Spirito, A. Neto, D. Cavallo, and N. Llombart, "Diffraction-limited imaging using a silicon integrated array at submillimeter wavelengths," in *European conference on Antennas and Propagation (EuCAP)*, 2021.

[24] K. B. Cooper, R. J. Dengler, N. Llombart, T. Bryllert, G. Chattopadhyay, E. Schlecht, J. Gill, C. Lee, A. Skalare, I. Mehdi, and P. H. Siegel, "Penetrating 3-d imaging at 4- and 25-m range using a submillimeter-wave radar," *IEEE Transactions on Microwave Theory and Techniques*, vol. 56, no. 12, pp. 2771–2778, 2008.

[25] E. Gandini, A. Tamminen, A. Luukanen, and N. Llombart, "Wide field of view inversely magnified dual-lens for near-field submillimeter wavelength imagers," *IEEE Transactions on Antennas and Propagation*, vol. 66, no. 2, pp. 541–549, 2018.

[26] J. Bueno, S. Bosma, T. Bußkamp-Alda, M. Alonso-delPino, and N. Llombart, "Lossless matching layer for silicon lens arrays at 500 ghz using laser ablated structures," *IEEE Transactions on Terahertz Science and Technology*, vol. 12, no. 6, pp. 667–672, 2022.

[27] S. van Berkel, E. Malotaux, C. de Martino, M. Spirito, D. Cavallo, A. Neto, and N. Llombart, "System nep verification of a wideband thz direct detector in cmos," in *2020 45th International Conference on Infrared, Millimeter, and Terahertz Waves (IRMMW-THz)*, pp. 1–1, 2020.

[28] M. Hoogelander, M. Alonso-delPino, N. Llombart, and M. Spirito, "Over-the-air characterization techniques for antenna-coupled direct-detectors at terahertz frequencies," in *2023 IEEE/MTT-S International Microwave Symposium - IMS 2023*, pp. 919–922, 2023.

[29] Y. Yang, A. Shutler, and D. Grischkowsky, "Measurement of the transmission of the atmosphere from 0.2 to 2 thz," *Optics express*, vol. 19, pp. 8830–8, 04 2011.

A

Deviation in dielectric constant of hyperbolic lenses

After aligning as described in Chapter 3, the radiation patterns were measured. The comparison of the measured patterns and simulated patterns can be found in Figure A.1. The simulated patterns here, are the ones obtained from the reaction integral as in Appendix B.

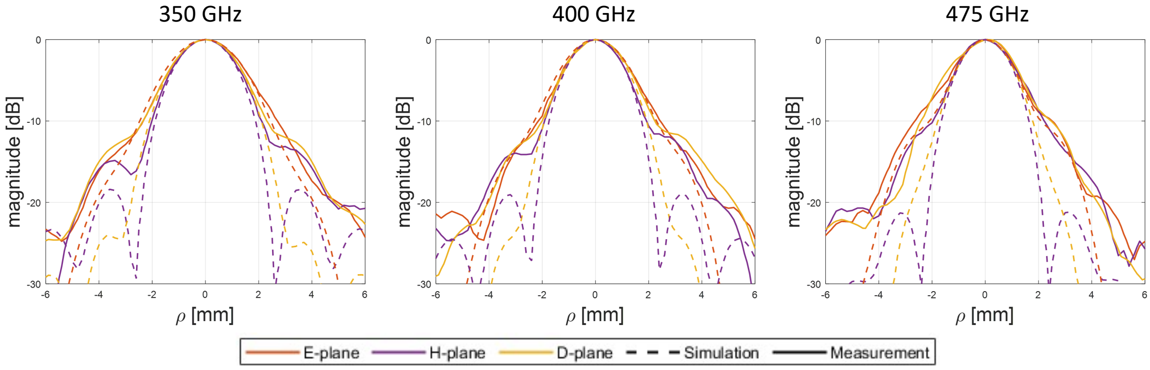

Figure A.1: Patterns measured with $F_{bc2} = 10.5cm$

From the figure it can be seen that the simulated patterns have a narrower pattern than the measured patterns. Re-alignment of the source and/or biconvex lens within the estimated accumulated worst-case deviation, which was shown to be 0.7mm in Chapter 3, did not improve the performance. Characterization of the HDPE material that was used for the biconvex lens and planoconvex lens turned out that dielectric constant that was used for the design, $\epsilon_r = 2.4$ did not match with the dielectric constant of the used HDPE $2.3 < \epsilon_r < 2.4$.

Figure A.2 shows the ray tracing in GRASP for two lenses with the same dimensions but different ϵ_r. The figure shows that the imaging plane is moved further away from the biconvex lens.

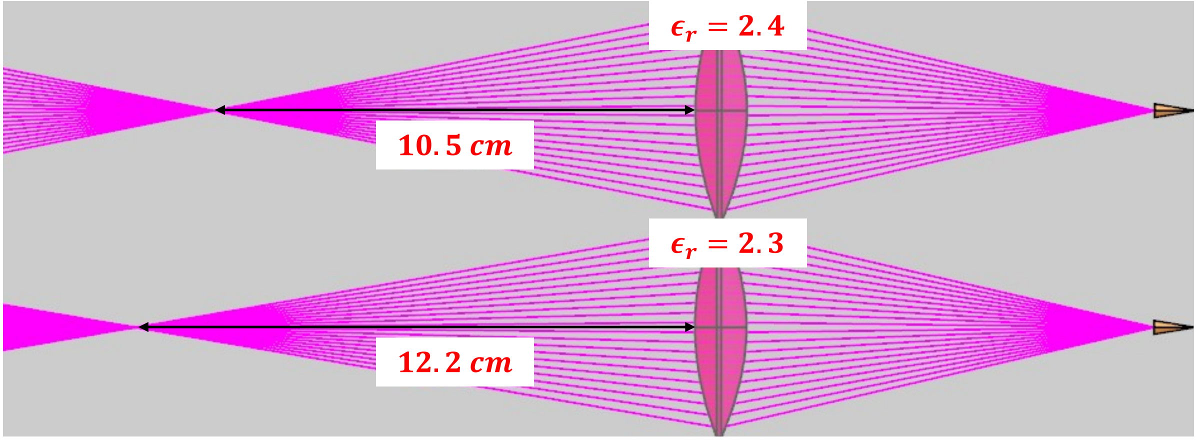

Figure A.2: Effect of deviation in dielectric constant ϵ_r on the focus

Since there was uncertainty about the exact value of ϵ_r, the exact location of the imaging plane was also not known. To this end, the radiation patterns were measured at different distances of F_{bc2} for the frequency where the deviation of the radiation pattern is the strongest, which is at 475 GHz (see Figure A.1). Figure A.3 shows the radiation patterns for 475 GHz for different locations of the imaging plane.

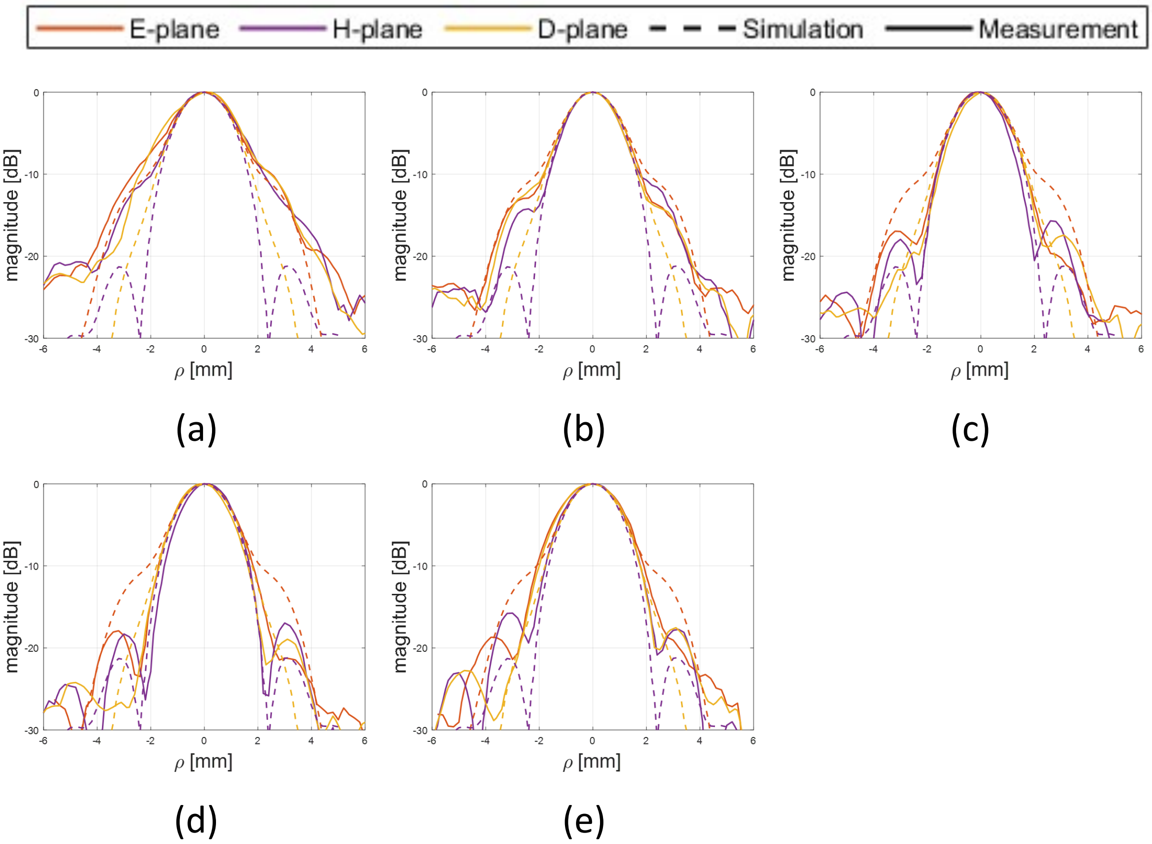

(a) (b) (c) (d) (e)

Figure A.3: Patterns measured for F_{bc2} = (a) 10.5cm (b) 10.9cm (c) 11.4cm (d) 11.9cm (e) 12.4cm

Figure A.3 shows that the pattern for $F_{bc2} = 11.9cm$ has the best overall agreement with the simulation. The similarity between measured and simulated patterns was further explored after all frequencies were measured by comparing the directivity of the measured patterns with the directivity of the simulated patterns, which is shown in Chapter 4. When the directivities were shown to be in good agreement, it was concluded that location of the imaging plane was at F_{bc2} = 11.9 cm instead of 10.5 cm.

B

Impact of the polarized THz source on the measured radiation patterns

To find the influence of the horn on the measured patterns, the simulated electric field of the detector in the imaging plane has been compared to a pattern that is obtained using a reaction integral involving the simulated fields of the horn, which are displaced as the horn moves across the imaging plane. In thi simulation, the horn and detector have identical polarization. To generalise the scenario, the biconvex lens and horn are represented with their equivalent apertures, as shown in Figure B.1.

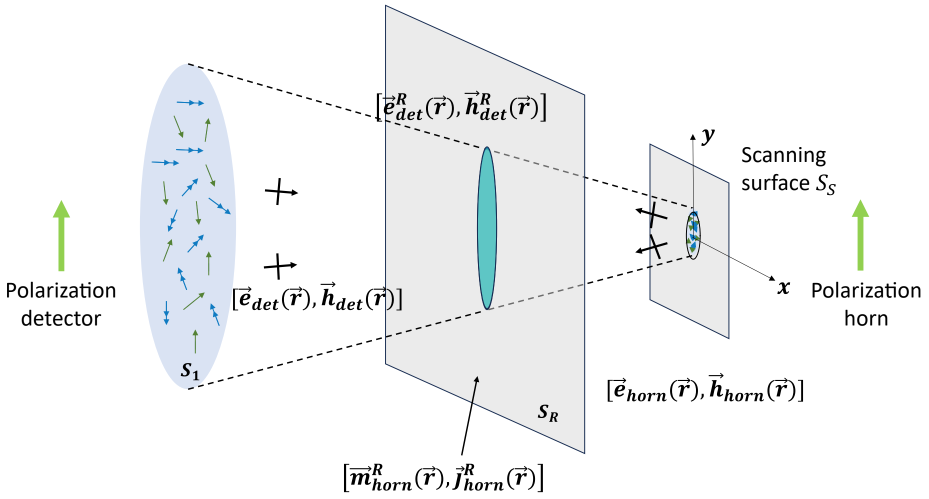

(a) Horn located at the center.

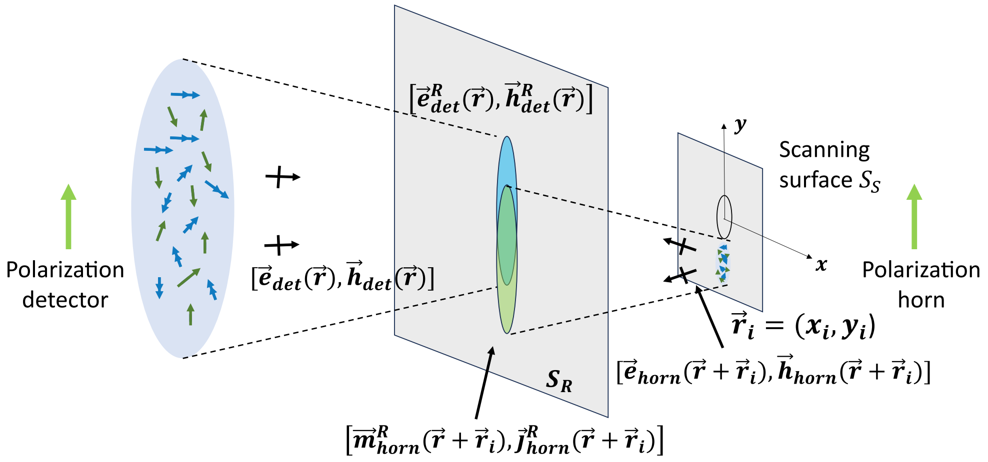

(b) Horn displaced (x_i, y_i) from center.

Figure B.1: Representation of the biconvex lens and horn with their equivalent aperture to evaluate the coupling. Note that when the horn is displaced with $\vec{r}_i = (x_i, y_i)$ in scanning surface S_S, equivalent currents $[\vec{m}_{horn}(\vec{r}+\vec{r}_i), \vec{j}_{horn}(\vec{r}+\vec{r}_i)]$ are also displaced $\vec{r}_i$ on the reaction integral surface S_R.

The equivalent aperture of the biconvex lens supports the electric and magnetic fields $[\vec{e}_{det}(\vec{r}), \vec{h}_{det}(\vec{r})]$, which are being focused toward the equivalent aperture of the horn in Figure B.1a. The equivalent aperture of the horn supports the electric and magnetic fields $[\vec{e}_{horn}(\vec{r}), \vec{h}_{horn}(\vec{r})]$.

For each scanning position $\vec{r}_i$ of the horn in scanning surface S_S, the coupling efficiency, $\eta_R(\vec{r}_i)$, where $\vec{r}_i = \sqrt{x_i^2 + y_i^2}$ represents the scanning of the horn in scanning surface S_S, is calculated as:

$$\eta_R(\vec{r}_i) = \frac{|V_{oc}(\vec{r}_i)|^2}{16 P_{rad} P_{horn}} \tag{B.1}$$

Where P_{rad} is the total power radiated by the equivalent aperture of the biconvex lens, P_{horn} is the total power radiated by the by the equivalent aperture of the horn and $V_{oc}(\vec{r}_i)$ is the open circuit voltage of the Thevenin equivalent circuit for location $\vec{r}_i$ of the horn. P_{rad} is calculated as:

$$P_{rad} = \frac{1}{2\zeta_0} \int\int_{S_1} |\vec{e}_{det}(\vec{r})|^2 dS \tag{B.2}$$

Where S_1 is the area of the equivalent aperture of the biconvex lens, which is illustrated in Figure B.1a. P_{horn} is evaluated in a similar manner. $V_{oc}(\vec{r}_i)$ is calculated as:

$$V_{oc}(\vec{r}_i) = \int\int_{S_R} \vec{h}^R_{det}(\vec{r}) \cdot \vec{m}^R_{horn}(\vec{r} + \vec{r}_i) - \vec{e}^R_{det}(\vec{r}) \cdot \vec{j}^R_{horn}(\vec{r} + \vec{r}_i) dS \tag{B.3}$$

Where S_R is a surface between the equivalent apertures indicated in Figure B.1 with the grey area and $\vec{m}^R_{horn}$ and $\vec{j}^R_{horn}$ are the equivalent currents induced by the horn, defined as in:

$$\vec{j}^R_{horn}(\vec{r} + \vec{r}_i) = \hat{n} \times \vec{h}_{horn}(\vec{r} + \vec{r}_i) \tag{B.4}$$

$$\vec{m}^R_{horn}(\vec{r} + \vec{r}_i) = -\hat{n} \times \vec{e}_{horn}(\vec{r} + \vec{r}_i) \tag{B.5}$$

Where $\hat{n}$ is the unit normal vector on surface S_R pointing inward the volume containing the detector. If the horn is displaced by $\vec{r}_i$, $\vec{j}_{horn}(\vec{r} + \vec{r}_i)$ and $\vec{m}_{horn}(\vec{r} + \vec{r}_i)$ move by the same $\vec{r}_i$ in the grey plane (see Figure B.1b). Since $\vec{e}_{det}(\vec{r})$ and $\vec{h}_{det}(\vec{r})$ do not change if the horn is moved, $\eta_R(\vec{r}_i)$ can be calculated by linearly shifting the equivalent currents, making it an efficient computation. $\eta_R(\vec{r}_i)$ is calculated for $(x_i, y_i) \in [-5, 5]$.

As the power received by the detector is proportional to $\eta_R(\vec{r}_i)$, a comparison between $\eta_R(\vec{r}_i)$ and $|\vec{e}_{det}(\vec{r}_i)|^2$ gives insight to how well the measurements with the horn represent $|\vec{e}_{det}|^2$. Figure B.2 shows the comparison between the normalised patterns of $\eta_R(\vec{r}_i)$ and $|\vec{e}_{det}(\vec{r}_i)|^2$.

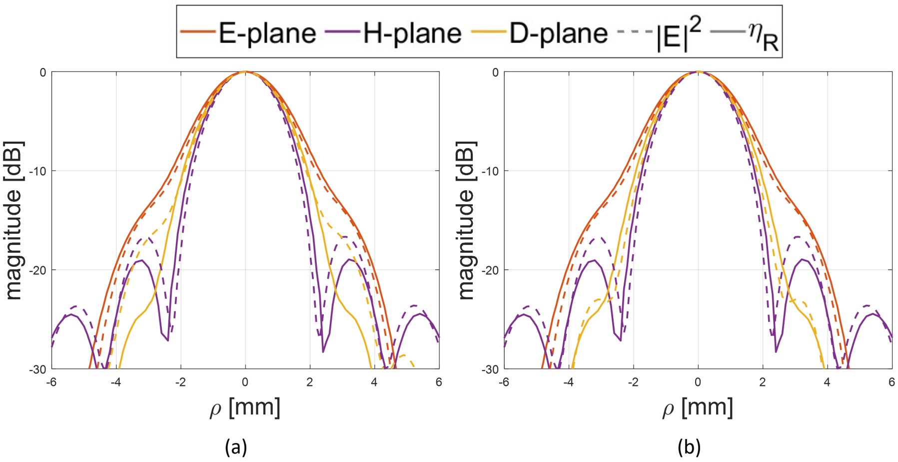

Figure B.2: Comparison at 400GHz between (a) $\eta_R(\vec{r}_i)$ and $|\vec{e}_{det}(\vec{r}_i)|^2$ (b) $\eta_R(\vec{r}_i)$ and $|e^{co}_{det}(\vec{r}_i)|^2$

The agreement between $\eta_R(\vec{r}_i)$, $|\vec{e}_{det}(\vec{r}_i)|^2$ and $|e^{co}_{det}(\vec{r}_i)|^2$ is very good up to -15 dB, and therefore in this work the measured patterns with the horn will be compared to $|\vec{e}_{det}(\vec{r}_i)|^2$.